UNIVERSITÀ
DEGLI STUDI
DI PADOVA

University of Padova

Department of Physics and Astronomy "Galileo Galilei"

Ph.D. course in Physics - XXXV cycle

BEAMLINE DESIGN AND CALORIMETER PROTOTYPES FOR THE ENUBET MONITORED NEUTRINO BEAM FACILITY

SUPERVISOR
Prof. Andrea Longhin

PHD STUDENT
Claudia Caterina Delogu

Academic Year 2021-2022

Contents

Outline

The Standard Model of particle physics combines the description of the electrodynamics, the weak interactions and the strong interactions with the classification of all the known elementary particles. Neutrinos are the least known fermions of the Standard Model. Like any other lepton they do not experience strong interactions, but since they have no electric charge these particles only interact through the weak force. Thus, experimental neutrino physics is quite challenging. Neutrinos are key ingredients for Beyond Standard Model searches and still a source of unexpected results.

Typical measurements of neutrinos characteristics, such as oscillations, are based on the number of specific flavours of neutrinos that appear or disappear after a given length from their production point, compared to the number of produced neutrinos. In such context, there is the need to carefully have an accurate estimation of the original flux of neutrinos. So far most beam-based neutrino experiments estimate the original flux of neutrinos by means of models and data on hadron production, which however carry with them an intrinsic systematic uncertainty of about 10%. In order to reduce this uncertainty, a new generation of neutrino beams has been proposed: the results presented in this thesis have been achieved in the framework of the ENUBET ERC project. The goal of ENUBET (Enhanced NeUtrino BEams from Kaon Tagging) is to develop the first "monitored neutrino beam", where the neutrino flux can be measured with a 1% precision. The idea is to fully instrument the secondary particle decay tunnel with a longitudinally segmented calorimeter, which will tag the large angle leptons produced together with the neutrinos. A typical example is measuring the electron neutrinos from kaon decays by means of measuring the positrons in the K_{e3} decay. ENUBET consists of a conventional narrow-band beam with a short transfer line ($\sim$20 m) followed by a 40 m long instrumented decay tunnel. The most significant studies of the project consist of the primary protons extraction scheme, the design of the secondary beamline, the reconstruction algorithms for the lepton tagger, the prototype activities for detectors, and studies to evaluate the reduction of the systematics.

The work presented in this thesis focuses on two aspects of ENUBET: the design of the hadronic beamline and the tagger detector development. In Chapter 1 the fundamental physics notions are given along with a general description of the ENUBET project. From the interaction of protons on the target, particles must be focused and momentum selected and transported at the entrance of the decay pipe, ensuring that the rate of events on the tunnel walls is tolerated by the instrumentation. The transfer line implementation must result in a beam of electron and muon neutrinos originating from the decays of kaons. The studies on the design and simulation of the optimized kaon-enriched beamline are presented in Chapter 2. The tunnel technology must

ensure good energy resolution and radiation tolerance and must be inexpensive in order to be scaled up to tens of meters. The R&D campaign converged to the final prototype of the modular calorimeter that will be used to discriminate signal events (positrons or muons from kaons) from the background. Chapter 3 focuses on the construction, test and data analysis of the most recent calorimeter prototypes.

Chapter 1

Neutrino beams and the ENUBET project

Over the last few decades, the importance and relevance of neutrino physics as a probe for the Standard Model, and the physics beyond it, has progressively increased. A thorough investigation of the nature of neutrinos could provide answers to cosmological problems, such as the asymmetry between matter and antimatter in our Universe. To comprehend this, it is necessary to investigate how neutrinos interact with the other Standard Model particles, i.e., to have a deep understanding of the cross sections at various energy ranges.

By performing a direct measurement of the neutrino flux inside an instrumented decay tunnel, the ENUBET Collaboration aims to show that an absolute cross section precision of the order of $\mathcal{O}(1\%)$ can be achieved. This Chapter will give a quick overview of neutrino physics, as well as the ENUBET project's physics case.

1.1 Oscillations and cross-section measurements

Neutrinos have a sub-eV rest mass, although not zero (in fact, in the original formulation of the Standard Model neutrinos are massless fermions). Observation of neutrino oscillations provides such evidence. The so-called solar electron neutrino (ν_e) is created by nuclear events in the Sun's core. The rate of solar neutrinos detected (Davis, 1968 [1]) was much lower than Bachall's Standard Solar Model expected [2,3]. Following Davis experiment, others, such as the Super–Kamiokande detector, provided similar results from atmospheric neutrinos [4]. In 2001, the SNO experiment demonstrated that a fraction of the solar ν_e converts into muon neutrino (ν_μ) or τ neutrino (ν_τ) [5]. The SNO experiment's answer to the Solar Standard Model issue resulted in conclusive proof of the neutrino oscillation phenomenon.

1.1.1 Oscillation phenomenon

Pontecorvo, Maki, Nakagawa, and Sakata explained this mechanism as follows: neutrino flavours can combine, resulting in one type of neutrino oscillating into the other. This effect is only possible if neutrinos are massive particles. In weak decays, neutrinos are produced in a well-defined

lepton flavour eigenstate, which is a mixing of their mass eigenstates [6]. The mixing matrix

$$|\nu_l\rangle = \sum_{i=1}^{n=3} U_{li}^{*} |\nu_i\rangle \tag{1.1}$$

relates weak eigenstates ν_{l} to mass eigenstates ν_{i}. U represents the PMNS matrix (Pontecorvo-Maki-Nakagawa-Sakata matrix), the lepton analogue of the CKM matrix for quarks. For three flavours, we have:

$$\begin{aligned} U &= \begin{pmatrix} 1 & 0 & 0 \\ 0 & c_{23} & s_{23} \\ 0 & -s_{23} & c_{23} \end{pmatrix} \begin{pmatrix} c_{13} & 0 & s_{13}e^{-i\delta} \\ 0 & 1 & 0 \\ -s_{13}e^{-i\delta} & 0 & c_{13} \end{pmatrix} \begin{pmatrix} c_{12} & s_{12} & 0 \\ -s_{12} & c_{12} & 0 \\ 0 & 0 & 1 \end{pmatrix} \cdot \\ &\cdot \begin{pmatrix} 1 & 0 & 0 \\ 0 & e^{i\alpha_1/2} & 0 \\ 0 & 0 & e^{i\alpha_2/2} \end{pmatrix} = \\ &= \begin{pmatrix} c_{12}c_{13} & s_{12}c_{13} & s_{13}e^{-i\delta} \\ -s_{12}c_{23} - c_{12}s_{23}s_{13}e^{i\delta} & c_{12}c_{23} - s_{12}s_{23}s_{13}e^{i\delta} & s_{23}c_{13} \\ s_{12}s_{23} - c_{12}c_{23}s_{13}e^{i\delta} & -c_{12}s_{23} - s_{12}c_{23}s_{13}e^{i\delta} & c_{23}c_{13} \end{pmatrix} \cdot \\ &\cdot \begin{pmatrix} 1 & 0 & 0 \\ 0 & e^{i\alpha_1/2} & 0 \\ 0 & 0 & e^{i\alpha_2/2} \end{pmatrix} \end{aligned} \tag{1.2}$$

$c_{ij} = \cos\theta_{ij}$, $s_{ij} = \sin\theta_{ij}$ and δ, α_i are real phases.
Using the latter results, the evolution of a flavour eigenstate is given by:

$$|\nu_i(t)\rangle = \sum_{j=e,\mu,\tau} \left(\sum_k U_{ik}^{*} e^{-iE_k t} U_{jk} \right) |\nu_j\rangle \tag{1.3}$$

where both i and j are flavour indexes. This implies that if the matrix U is non-diagonal, as in the case of the PMNS mixing matrix, flavour states evolve into a superposition of different flavour states, leading to the phenomenon of neutrino oscillations. The transition probability for a neutrino i at time $t = 0$ detected as j at a later time t is

$$P_{\nu_i \to \nu_j}(t) = |\langle \nu_i | \nu_j(t) \rangle|^2 \tag{1.4}$$

If we define $\Delta m_{ij}^2 = m_i^2 - m_j^2$, the oscillation probability in vacuum expressed in terms of the distance L travelled by neutrinos and their energy E is:

$$P_{\nu_\alpha \to \nu_\beta}(L, E) = \sum_{k,j} U_{\alpha k}^{*} U_{\beta k} U_{\alpha j} U_{\beta j}^{*} \exp\left(-i \frac{\Delta m_{jk}^2 L}{4E} \right) \tag{1.5}$$

that can be rewritten as:

$$P_{\nu_\alpha \to \nu_\beta} = \delta_{\alpha\beta} - 4\sum_{i>j} \mathrm{Re}(U^*_{\alpha i}U_{\beta i}U_{\alpha j}U^*_{\beta j}) \sin^2\left(\frac{1.27\Delta m^2_{ij}(\mathrm{eV}^2)L(\mathrm{km})}{E(\mathrm{GeV})}\right) \pm 2\sum_{i>j} \mathrm{Im}(U^*_{\alpha i}U_{\beta i}U_{\alpha j}U^*_{\beta j}) \sin\left(\frac{2.54\Delta m^2_{ij}(\mathrm{eV}^2)L(\mathrm{km})}{E(\mathrm{GeV})}\right) \quad (1.6)$$

where the sign before the second sum is positive for neutrinos and negative for antineutrinos. $L_{\mathrm{osc}} = 4E/\Delta m^2_{ij}$ is called the "oscillation length". If $\alpha \neq \beta$ the formula provides the probability of a change of flavour and it is called the "appearance probability"; while, if $\alpha = \beta$, $1 - P_{\nu_\alpha \to \nu_\alpha}$ is called the "disappearance probability".
From Eq. 1.2 and 1.6 one can prove that:

- if neutrinos are Majorana particles, the phase factors α_1 and α_2 may be different from zero. However, because the oscillation probabilities remain unchanged, the neutrino oscillation process cannot be used to determine whether neutrinos are Majorana particles or not;
- if neutrino oscillation violates CP symmetry, the phase factor δ must be non-zero. Only the imaginary term in 1.6 can contain the CP-violating phase, this means that only experiments in "appearance" mode ($\alpha \neq \beta$) are sensitive to CP violation, while experiments in "disappearance" mode ($\alpha = \beta$) are not;
- oscillations experiments only measure squared mass differences and mixing parameters, not the absolute neutrino mass. For this reason, neutrino oscillation data are compatible with two types of mass spectra and the mass hierarchy (i.e. the ordering) is unknown.

1.1.2 Current measured oscillation parameters

The purpose of a neutrino oscillation experiment is to measure the oscillation probabilities. An experiment has to be set up with $E/L \simeq \Delta m^2_{ij}$ (where L is the source-detector distance), in order to maximize the sensitivity to a given value of Δm^2_{ij} (see Eq. 1.6).
If $L \ll L_{\mathrm{osc}}$ the oscillation does not have time to produce an appreciable effect, because $\sin^2(L/L_{osc}) \ll 1$. For $L \gg L_{\mathrm{osc}}$, the phase is averaged to $\langle \sin^2(L/L_{osc})\rangle = 1/2$ and the oscillation pattern vanishes.

Because $\Delta m^2_{21} \ll \Delta m^2_{31}$ and $\Delta m^2_{31} \approx \Delta m^2_{32}$, for sufficiently small L/E, the Δm^2_{21} term in 1.6 can be ignored. In this case ν_e and ν_μ oscillations are the dominant ones and the probabilities become:

$$P(\nu_e \to \nu_\mu) \cong 1 - \sin^2 2\theta_{13} \sin^2\left(\frac{\Delta m^2_{31}L}{4E}\right)$$

$$P(\nu_\mu \to \nu_\mu) \cong 1 - 4\cos^2\theta_{13}\sin^2\theta_{23}(1 - \cos^2\theta_{13}\sin^2\theta_{23}) \sin^2\left(\frac{\Delta m^2_{31}L}{4E}\right)$$

$$P(\nu_\mu \to \nu_e) \cong \sin^2 2\theta_{13}\sin^2\theta_{23}\sin^2\left(\frac{\Delta m^2_{31}L}{4E}\right)$$

Source	ν **type**	**E (MeV)**	**L (m)**	$\mathbf{\Delta m^2\ (eV^2)}$
Solar	ν_e	1	10^{10}	10^{-10}
Atmospheric	$\nu_{\mu,e}, \bar{\nu}_{\mu,e}$	$10^2 - 10^5$	10^4 - 10^7	$10^{-1} - 10^{-4}$
Reactor	$\bar{\nu_e}$	1	10 - 10^{-3}	$1 - 10^{-3}$
			$10^4 - 10^{-5}$	$10^{-4} - 10^{-5}$
Accelerator	$\nu_\mu, \bar{\nu}_\mu$	$10^3 - 10^4$	10^2	> 0.1
			$10^5 - 10^6$	$10^{-2} - 10^{-3}$

Table 1.1: Characteristic values of L and E for oscillation experiments and corresponding ranges of $|\Delta m^2|$, categorized based on the neutrino source used. Adapted from [7].

Oscillation parameter	**Central value** $\pm$ **1**σ	3σ range
Normal hierarchy (best fit)		
$\sin^2\theta_{12}$	$0.304^{+0.012}_{-0.012}$	$0.269 - 0.343$
θ_{12} (°)	$33.45^{+0.77}_{-0.74}$	$31.27 - 35.87$
$\sin^2\theta_{23}$	$0.450^{+0.019}_{-0.016}$	$0.408 - 0.603$
θ_{23} (°)	$42.1^{+1.1}_{-0.9}$	$39.7 - 50.9$
$\sin^2\theta_{13}$	$0.02246^{+0.00062}_{-0.00062}$	$0.02060 - 0.02435$
θ_{13} (°)	$8.62^{+0.12}_{-0.12}$	$8.25 - 8.98$
δ_{CP} (°)	230^{+36}_{-25}	$144 - 350$
$\Delta m^2_{21}/10^{-5}\text{eV}^2$	$7.42^{+0.21}_{-0.20}$	$6.82 - 8.04$
$\Delta m^2_{31}/10^{-3}\text{eV}^2$	$+2.510^{+0.027}_{-0.027}$	$2.430 - 2.593$
Inverted hierarchy ($\Delta\chi^2 = 7.0$)		
$\sin^2\theta_{12}$	$0.304^{+0.013}_{-0.012}$	$0.269 - 0.343$
θ_{12} (°)	$33.45^{+0.78}_{-0.75}$	$31.27 - 35.87$
$\sin^2\theta_{23}$	$0.570^{+0.016}_{-0.022}$	$0.410 - 0.613$
θ_{23} (°)	$49.0^{+0.9}_{-1.3}$	$39.8 - 51.6$
$\sin^2\theta_{13}$	$0.022461^{+0.00074}_{-0.00062}$	$0.02055 - 0.02457$
θ_{13} (°)	$8.61^{+0.14}_{-0.12}$	$8.24 - 9.02$
δ_{CP} (°)	278^{+22}_{-30}	$194 - 345$
$\Delta m^2_{21}/10^{-5}\text{eV}^2$	$7.42^{+0.21}_{-0.20}$	$6.82 - 8.04$
$\Delta m^2_{31}/10^{-3}\text{eV}^2$	$-2.490^{+0.026}_{-0.028}$	$-2.574 - 2.410$

Table 1.2: Neutrino oscillation parameters for normal and inverted hierarchy. From [8, 9].

Table 1.1 shows the typical L/E values for several types of neutrino experiments, as well as the Δm^2 ranges to which they are most sensitive.

The following are the most important open topics in neutrino physics that oscillation experiments can address:

- determining the neutrino mass hierarchy: "normal" ($m_1 < m_2 \ll m_3$) or "inverted" ($m_3 \ll m_1 < m_2$);
- a high precision measurement of θ_{23}, so to determine its octant;
- observing the CP violating phase δ, since $P_{\nu_\alpha \to \nu_\beta} - P_{\bar{\nu}_\alpha \to \bar{\nu}_\beta} \propto \mathrm{Im}(U^*_{\alpha i} U_{\beta i} U_{\alpha j} U^*_{\beta j}) \propto \sin\delta$;
- test of sterile neutrinos.

The results of a large number of studies over several decades were combined to identify Δm^2_{12} and $\sin^2 2\theta_{12}$, while the unknown sign of Δm^2_{31} (which is currently indistinguishable from Δm^2_{32}) affects all the remaining parameters.
Table 1.2 contains the most recent three-flavour oscillation parameters from a fit to global data.

1.1.3 Neutrino cross-sections

Since the disappearance and appearance probabilities are calculated from the rate of neutrinos interacting in the detector at a distance L from the source, accurate predictions of neutrino oscillation parameters need a precise understanding of neutrino interactions with matter (cross-section). Oscillation probabilities are a function of E_ν^{-1}, current accelerator-based studies focus on neutrino energies ranging from a few hundred MeV to the GeV scale. Cross-sections are easily described by the Standard Model [10] since neutrino masses are very small. The absolute values of the neutrino masses are yet unknown and constrained to very small values (< eV) by cosmological constraints (Planck [11], WMAP [12]) and direct measurements (KATRIN [13], ECHo [14], HOLMES [15], NUMECS [16]). They cannot be derived from neutrino oscillation experiments, since they are sensitive only to the squared mass differences.

Neutrinos can be detected by interactions on electrons or nucleons through weak charged currents (mediated by the $W^\pm$ bosons) or neutral currents (Z^0 boson). Charged Current (CC) interactions are easier to detect since they involve a lepton in the final state and allow for the determination of the neutrino leptonic flavour. Neutral Current (NC) interactions can only be detected if the final state contains an excited nucleus.

The total cross-section is $\sigma \sim |M|^2/s$, where M is the scattering amplitude and s the center-of-mass energy. The cross-sections are proportional to the Fermi constant G_F^2. The neutrino-electron cross-section is smaller than neutrino-nucleon cross-section, as can be seen from Tab. 1.3, taking into account that $m_e \ll m_{nucleon}$.

Scattering on electrons In the Elastic Scattering:

$$\nu_l + e^- \to \nu_l + e^-$$

	Neutrino-electron scattering	Neutrino-nucleon scattering
Amplitude	$M \sim G_F E_\nu m_e$	$M \sim G_F E_\nu m_{nucl}$
Total cross-section	$\sigma \sim G_F^2 E_\nu^2, E_\nu \ll m_e$	$\sigma \sim G_F^2 E_\nu^2, E_\nu \ll m_{nucl}$
	$\sigma \sim G_F^2 m_e E_\nu, E_\nu \gg m_e$	$\sigma \sim G_F^2 m_p E_\nu, E_\nu \gg m_{nucl}$

Table 1.3: Neutrino-electron and neutrino-nucleon cross-sections.

the final state is the same as the initial state, thus this process does not have a threshold. The effect is a redistribution of the total energy and momentum between the two particles. In the case of the ν_e scattering, we have at tree level CC and NC processes, while for ν_μ and ν_τ we only have NC contribution. Measurements of the total cross-section for the elastic process, for $\sqrt{s} \gg m_e$ are listed in Table 1.4. From this we see that $\sigma_{\nu_e} : \sigma_{\overline{\nu}_e} : \sigma_{\overline{\nu}_{\mu,\tau}} : \sigma_{\nu_{\mu,\tau}} = 1 : 0.42 : 0.16 : 0.14$,

Process	Total cross-section ($10^{-46} cm^2$)
$\nu_e + e^- \to \nu_e + e^-$	$\sigma \simeq 93\ s/\mathrm{MeV}^2$
$\overline{\nu}_e + e^- \to \overline{\nu}_e + e^-$	$\sigma \simeq 39\ s/\mathrm{MeV}^2$
$\nu_{\mu,\tau} + e^- \to \nu_{\mu,\tau} + e^-$	$\sigma \simeq 15\ s/\mathrm{MeV}^2$
$\overline{\nu}_{\mu,\tau} + e^- \to \overline{\nu}_{\mu,\tau} + e^-$	$\sigma \simeq 13\ s/\mathrm{MeV}^2$

Table 1.4: Total neutrino–electron elastic scattering cross-sections for $\sqrt{s} \gg m_e$ [6]

which means that the $\nu_e - e^-$ cross-section is about 2.4 times larger than the $\overline{\nu}_e - e^-$ cross-section, 6.2 times larger than the $\nu_{\mu,\tau} - e^-$ cross-section, 7.1 times larger than the $\overline{\nu}_{\mu,\tau} - e^-$ cross-section. The future and current experiments will face a big challenge in measuring, for instance, CP violation through the oscillation mechanisms: it is a measure conducted in appearance mode, which has a smaller probability than the disappearance mode. Moreover, it is necessary to measure the rate of neutrinos at the detector, since the anti-neutrino process has to be subtracted from the neutrino process.

Last, ν_μ with energy above the μ production threshold can interact with electrons through the Quasi Elastic (QE) CC process:

$$\nu_\mu + e^- \to \nu_e + \mu^-$$

Scattering on nucleons The Quasi Elastic scattering is the main mechanism at low energies ($E_\nu \ll$ GeV):

$$\begin{array}{lll} \text{CC:} & \nu_l + n \to l^- + p & \overline{\nu}_l + p \to l^+ + n \\ \text{NC:} & \nu_l + n/p \to \nu_l + n/p & \overline{\nu}_l + n/p \to \overline{\nu}_l + n/p \end{array}$$

The neutrino scatters elastically off the nucleon ejecting a nucleon from the target. The threshold for CC interactions is given by energy conservation. Cowan and Reines employed the QE process $\overline{\nu}_e + p \to e^+ + n$, known as inverse beta decay, when neutrinos were discovered for the first time. Detectors of electron antineutrinos generated in reactors now employ this method.

The weak mixing angle, which relates the values of the nucleon weak and electromagnetic form factors that occur in cross-section expressions, was measured using the elastic scattering (NC process) of ν_l, $\overline{\nu}_l$ on protons. For $\mathrm{E}_\nu \sim \mathrm{GeV}$, in the region between elastic and inelastic scattering, the production of pions is possible through the excitation of baryonic resonances. It is referred to as resonant scattering:

$$\begin{aligned} &\text{CC:} \quad \nu_l + N \to l^- + N' + \pi \\ &\text{NC:} \quad \nu_l + n/p \to \nu_l + n/p + \pi \end{aligned}$$

When $\mathrm{E}_\nu \gg \mathrm{GeV}$ neutrinos have enough energy to break the nucleons and the resulting Deep Inelastic Scattering (DIS) consists of a lepton and a hadronic shower:

$$\begin{aligned} &\text{CC:} \quad \nu_l + n/p \to l^- + X \quad \overline{\nu}_l + n/p \to l^+ + X \\ &\text{NC:} \quad \nu_l + n/p \to \nu_l + X \quad \overline{\nu}_l + n/p \to \overline{\nu}_l + X \end{aligned}$$

Scattering on nuclei The scattering is reduced to a sum of neutrino-nucleon scatterings when E_ν is greater than the nuclear binding energy. Low-energy neutrino interactions excite distinct energy levels with certain spin, isospin, and parity values; the energy thresholds may be calculated using kinematical considerations from the masses of the nuclei involved. A neutrino reacts with a nucleus (A,Z) in the following ways:

$$\begin{gathered} \overline{\nu}_e(\mathrm{A},\mathrm{Z}) \to e^+(\mathrm{A},\mathrm{Z}-1) \\ \nu_e(\mathrm{A},\mathrm{Z}) \to e^-(\mathrm{A},\mathrm{Z}+1) \\ \nu_l(\mathrm{A},\mathrm{Z}) \to \nu_l(\mathrm{A},\mathrm{Z}) \end{gathered}$$

1.2 Neutrino beams

Among the different types of experiments probing the neutrino oscillation phenomenon, accelerator neutrino beams cover an essential role, as they are able to produce directional neutrino fluxes with well definable energy and distance from the detector. Many important results have been achieved by these types of experiments over the years [17–19] as well as important future goals of solving the remaining open problems are based on them [20–22].

Accelerator neutrino experiments start from the extraction of protons from an accelerator. Protons are then directed toward a light target, such as Be, graphite or Al. This results in a secondary particle beam, which is charge- and momentum-selected and focused by a system of magnets. Secondary particles, which are mostly pions and kaons, are then free to decay in what is called a decay tunnel, producing neutrinos. As there is no way of directly focusing and selecting neutrinos, both the proton energy and intensity of the accelerator and the secondary focusing systems are crucial to produce a neutrino flux with the desired characteristics. A hadron dump at the end of the decay region prevents hadrons and charged leptons from propagating further, allowing only neutrinos to escape, resulting in a neutrino beam. Neutrino detectors are installed downstream of the beamline, along the neutrino trajectory. Fig. 1.1 depicts a generic layout of a neutrino beam facility.

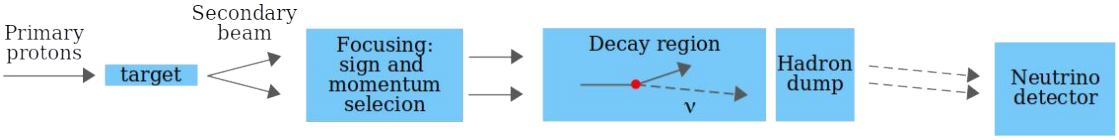

Figure 1.1: Typical layout of an accelerator neutrino beam.

The main products of the interactions of protons on target are π and K, which can decay in several ways, as shown in Tab. 1.5.

Data on hadron production are used to extrapolate models of secondary production, however, one of the main sources of uncertainty is the estimate of the neutrino flux starting with the generation of secondaries. For the normalisation of the number of hadrons and, consequently, neutrinos, it is essential to take into account the cross-sections and yields, usually measured using replica targets.

Most of the secondary particles created by the protons' interactions with the nuclear target are pions: typically, neutrino beams are composed of muon neutrinos, with small pollution of electron neutrinos. Due to this factor, muon neutrino oscillations are the ones mostly used by

Decay	Branching Ratio (%)
$\pi^+ \rightarrow \mu^+ \nu_\mu$	$\sim$100
$K^+ \rightarrow \mu^+ \nu_\mu$	63.6
$K^+ \rightarrow e^+ \pi^0 \nu_e$	5.1
$K^+ \rightarrow \mu^+ \pi^0 \nu_\mu$	3.4

Table 1.5: π, K decays and Branching Ratios (BR).

accelerator neutrino experiments, with typical neutrino energy ranging from 1 to 20 GeV and source-detector distances of several hundred kilometres.

Electron neutrinos are mainly produced by kaon and subsequent muon decays: $K^+ \rightarrow e^+ \pi^0 \nu_e$ and $\mu^+ \rightarrow e^+ \nu_e$ (with BR$\sim$100%). It is essential to optimize the length of the decay region and use shielding to prevent the muons from decaying. With increasing meson momentum, the required length of the decay region must increase: the probability of decay is $P = 1 - e^{-L_{tunnel}/L_0}$, where

$$L_0 = \beta c \gamma \tau_M = \frac{p_M}{m_M} c\tau_M = \begin{cases} 55.9 \text{ m} \dfrac{p_\pi}{\text{GeV}} \\ 7.51 \text{ m} \dfrac{p_K}{\text{GeV}} \end{cases} \tag{1.7}$$

As a result, only a portion of the produced mesons decays in an L-length tunnel.

The kinematics of the two-body decay of the mesons $M^+ \rightarrow \mu^+ \nu_\mu$ can be used to derive the neutrino spectrum. The energy of the neutrino E_ν emitted at an angle θ_0 with respect to the direction of the parent meson is:

$$E_\nu(\theta_\nu) = \frac{(1 - (m_\mu/m_M)^2) E_M}{1 + (E_M/m_M)^2 \theta_\nu^2} \tag{1.8}$$

from which it can be shown that for a non-zero neutrino emission angle θ_ν the neutrino energy loses the strong linear correlation with the secondary particle energy present at the on-axis emission. Equation 1.2 is graphed for the pion decay case in Figure 1.2, for some choices of decay angle between the neutrino and pion direction.

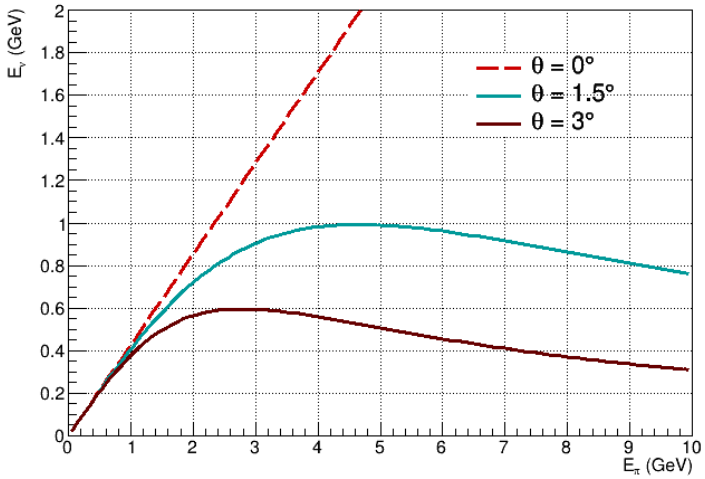

Figure 1.2: Neutrino energy from pion decay for different choices of decay angle.

Some of the past and current neutrino beamlines used for neutrino oscillation experiments are listed below.

- The K2K (KEK to Kamioka) experiment [17] was the first long-baseline experiment, with the goal of the confirmation of atmospheric ν_μ disappearance at the Super Kamiokande (SK) detector. It consisted of a ν_μ beam with an average energy of 1.3 GeV, directed toward the far (250 km) detector SK. A near detector system (300 m downstream of the target) was used to measure the beam profile. Data collection for the K2K experiment began in 1999 and ended in 2004. It observed an anomaly in the observed events, that pointed to the muon neutrino disappearance [23]. K2K also looked at the potential $\nu_\mu \rightarrow \nu_e$ oscillation, without reporting any event above the expected background [24].

- The Fermilab NuMI (Neutrinos at the Main Injector) facility produced a neutrino beam for the MINOS experiment (Main Injector Neutrino Oscillations) [18] with protons accelerated at 120 GeV resulting in an average neutrino energy of 3 GeV. The far detector, at 735 km from the source and placed underground, was an iron-scintillator tracking calorimeter with a total mass of 5.4 kton. Additionally, there was a smaller near detector built with the same technology. MINOS began data taking in 2005 until 2012 looking for the disappearance of ν_μ and appearance of ν_e, combining the atmospheric data and measuring the oscillation parameters [25].

  NOvA (NuMI Off-Axis ν_e Appearance) [20] started taking data in 2013 with a beam produced by NuMI with an average neutrino energy of 2 GeV. Its primary physics goals

are precise measurements of oscillation parameters, including the CP phase δ, and putting constraints on the neutrino mass hierarchy [26, 27].

- T2K (Tokai to Kamioka) [19] employs a narrow-band beam centred resulting from a primary proton beam accelerated to 30 GeV by J-PARC's Main Ring. The neutrino beam has an energy of 1.5 GeV, however, the concept of an off-axis neutrino beam was first implemented in the T2K experiment: at 2.51°, the neutrino energy is 600 MeV. The experiment utilizes a near detector complex at 280 m from the target to characterize the initial flux of neutrinos, and 295 km after the data are collected by SK. The data taking started in 2010 and since then the major results include the appearance of electron neutrinos in an accelerator muon neutrino beam [28, 29], the measurement of oscillation parameter $\sin^2\theta_{23}$ [30], and the hint of CP violation in the leptonic sector [31].

  Hyper Kamiokande (HK) [21], the improvement to the SK water Cerenkov detector, is expected to start operating in 2026. It will be characterized by higher-performance photodetectors and a greater fiducial mass. In addition to serving as the T2K far detector and enabling the observation of the CP violating phase δ, HK will also conduct highly sensitive investigations into a wide variety of phenomena, including atmospheric neutrino oscillation studies, proton decay searches, and neutrino astrophysics.

- DUNE [22] will use Liquid Argon time projection chambers placed 1300 km from the source, performing a calorimetric measurement of the particles produced by the interactions, together with a near detector at 600 meters from the production point. The wide band muon neutrino beam will be produced at Fermilab in the energy range 0.5-5 GeV. The experiment will start taking data in the early 2030s, collecting neutrino and antineutrino data to measure ν_μ disappearance and ν_e appearance probabilities in both ν_μ and $\bar{\nu}_\mu$ beams, allowing a good measurement of mass ordering and of the CP violating phase δ, the determination of the mass hierarchy and precision tests of the three-flavour neutrino oscillation paradigm.

Most of the oscillation experiments rely on the appearance of ν_e at the far detector, whereas pion-based sources mostly produce ν_μ. For example, accurate estimates of the expected neutrino fluxes at both near and far detectors are necessary for the T2K experiment. Hadro-production dominates flux uncertainties: a deep knowledge of the chains of hadronic interactions in targets is necessary for accurate neutrino flux modelling. The NA61/SHINE hadron production experiment is the source of the hadron production constraint for T2K: they employed a replica of the T2K target to measure the hadron production. This allowed to reduce the T2K neutrino flux uncertainty to $\sim$5% [32]. Fig. 1.3 shows the uncertainty on the ν_μ flux together with the improvement obtained by including the NA61/SHINE data.

1.2.1 Secondary beamlines

The specific implementation of the secondary beamline defines the type of neutrino beam that can be produced: the focusing system affects the neutrino beam intensity and the energy distribution [34]. The two types of beams that can be produced are called Wide Band and Narrow Band Beams (WBB and NBB, respectively).

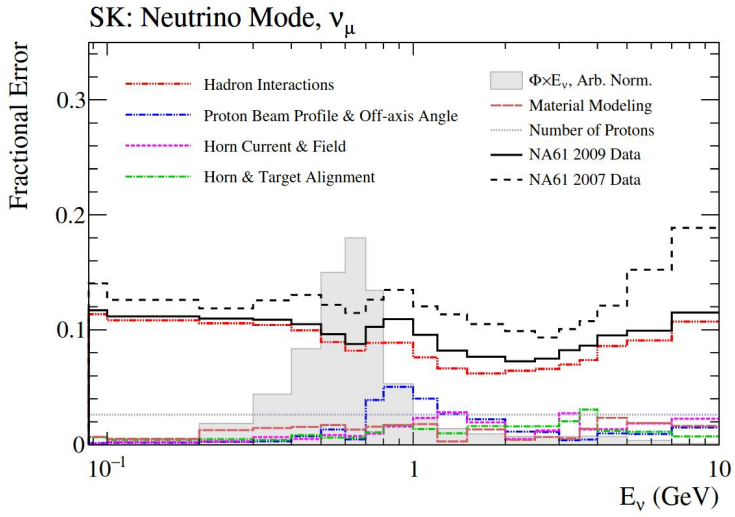

Figure 1.3: Fractional uncertainty on ν_μ flux [33].

- Wide Band Beams are obtained by focusing mesons only with magnetic horns, leading to a focusing section collinear with the decay tunnel. The resulting beam has a wide momentum range and a high intensity;

- Narrow Band Beams are based on accurate focusing and charge selection of the secondary particles, to transport only a narrow momentum range of the secondaries down to the decay tunnel, producing neutrinos in a small energy range. Thus the beam is less intense with respect to WBB, but with a specific momentum selection. When dipoles are also used, the loss of collinearity between the decay tunnel and the rest of the beamline significantly reduces the background level too.

1.3 Neutrino detectors

Neutrino detectors are located after the beam dump at a distance that ranges from tens of meters ("short baseline experiments") to hundreds of km ("long baseline experiments").

Various detection techniques are available to measure neutrino energy, direction and flavour [35].

- Water Cherenkov: they measure the Cherenkov light, allowing the reconstruction of the energy and the direction of charged particles scattered by neutrinos. They consist of pure water surrounded by photomultipliers. Large detectors can be built, but constraints on the target mass come from the necessity of background suppression, which requires the deployment of the detector deep underground. E_ν <GeV neutrinos can only produce e and μ in the final state. These detectors can distinguish the final state leptons because electrons rings are less sharp than the muon rings, but cannot distinguish particles from anti-particles. At larger energies, the reconstruction of the neutrino energy cannot be performed from kinematical constraints only since DIS also produces non-detectable neutral

particles. Water Cherenkov detectors allowed the detection of solar neutrinos down to 5 MeV [35]. A heavy-water based Cherenkov detector allowed SNO [36] to observe NC events together with ν_e CC events.

- Liquid scintillators: charged particles propagating in the scintillator release light that is typically collected by photomultipliers. They have limited particle identification capabilities, but they measure well the energy, especially at low energies (E_ν ∼1-10 MeV). At MeV energies, they are employed for detection of reactor neutrinos (KAMLAND [37], CHOOZ [38]) and low energy solar neutrinos (BOREXINO [39]). At energies around 10 MeV, they are used in the search of neutrinos from supernovae and for the study of pion decays (KARMEN [40], LSND [41], MINIBOONE [42]).

- Calorimeters: they measure the total energy of particles produced by scatterings. By alternating layers of calorimeters to, e.g., scintillators one gains information on the tracks of the charged particles, allowing discrimination between CC events due to ν_μ and ν_e (muons' tracks are longer than electrons') or the hadrons produced in CC or NC interactions. By magnetizing the calorimeter one can also discriminate charged particles from antiparticles. NUTEV [43] and MINOS [44] detectors use this technology. Also, precise measurements of neutrino cross sections and weak parameters have been performed with calorimeters at the West Area Neutrino Facility at CERN (using both narrow band and wide band beamlines), by the CDHS [45] and CHARM [46] experiments

- Radiochemical: a sufficiently large mass of a target nucleus is put underground, in order to reduce cosmogenic backgrounds. The target nucleus is chosen such that the cross-section is well known and such that the produced nuclei can be counted. This is the first technique used in solar neutrino experiments (measuring neutrino rates with ∼5% accuracy) and allows to reach the lowest neutrino energies so far [35].

- Liquid Argon Time Projection Chambers (LAr TPCs): Liquid Argon has various advantages. When an energetic charged particle passes through, Argon scintillates. Since it is a noble element, ionising radiation-produced electrons will not be absorbed as they go toward the detector readout. The density of liquid argon is another main reason for adopting it as a sensitive medium: there is a higher probability that a particle interacts with the detector. The small neutrino-nucleon interaction cross-sections make advantage of this property. Moreover, since Liquid Argon is also moderately priced, large-scale applications are possible. Lar TPCs were first proposed in [47] and have been chosen as the DUNE far detector technology [48].

1.4 ENUBET and future long-baseline oscillation experiments

In the next future, two facilities will be dominating the area of accelerator neutrino physics: DUNE (LBNF, Fermilab) and Hyper-Kamiokande (J-PARC, Japan). These two experiments will address a variety of topics: measure the CP violation phase, perform accurate measurements of oscillation parameters, and determine the mass hierarchy. The near-far detector cancellation

is typically used in this type of experiment to reduce the impact of systematic errors. The rate of ν_e and ν_μ at the source is measured by the near detectors, and the rate at the far detector is compared to it. Given that the corresponding cross-sections are correctly known, a near detector that is close to the source and identical to the far detector offers a normalisation for the ν_e and ν_μ rates. The current long-baseline experiments' systematic budget on the neutrino flux is at the 5% level for ν_μ and 10% level for ν_e events.

In this context, ENUBET is proposing to make accurate measurements of neutrino cross sections at the GeV scale (especially for ν_e) to overcome the need to completely rely on the near-far ratio technique that suffers from several limitations (different fluxes, acceptances, impact of the unknown contribution of different neutrino interaction modes, potential differences between the interactions of ν_e and ν_μ). This is achieved using a neutrino flux with much better precision with respect to the beams of long baseline experiments with a dedicated detector at close distance. The refined information on cross-section could be then fully exploited by long baseline experiments which, in the long run, will otherwise be heavily limited by the knowledge of cross-sections.

The ENUBET facility (see Sec. 1.5) will address this problem with the implementation of a monitored neutrino beam. The ENUBET technology has been proven to be feasible: the project, as will be discussed later, has been validated both by simulations and experimental proofs. The Collaboration has begun addressing the actual implementation at CERN and plans to submit a proposal in 2024/25, in order to start data collection in 2029, during LHC Run IV and in parallel to the DUNE/Hyper-Kamiokande data taking.

1.5 The ENUBET project

The current and future neutrino oscillation experiments are motivated by the measurement of δ_{CP} and the neutrino mass ordering, in addition to a better determination of the oscillation parameters. With respect to the results achieved in the last decades, this requires a considerable increase in precision: as a result, accelerator-based neutrino experiments require systematic errors to be reduced to a few percent. These experiments calculate the neutrino interaction event rate, which is the product of three variables: neutrino flux, interaction cross-section, and detector efficiency. Depending on the energy range of neutrinos, each one of these three quantities can become a dominant systematic uncertainty in the measurements. For example, in the hundreds-MeV to few-GeV energy range, neutrino-nucleus cross sections are one of the most important sources of systematic errors [35], thus becoming important in the interaction cross-section and in the detector efficiency. The ν_e and ν_μ fluxes are typically estimated from a full simulation of meson production and transport from the target to the beam dump and validated by external data: the uncertainties on such values depend on the production of mesons and their transport, that have non-negligible systematics. For this reason, neutrino fluxes are subject to considerable uncertainties, on the order of 5-10 percent [19, 20]. A greater understanding of the produced neutrino fluxes allows for a tighter limit on the neutrino appearance and disappearance probability, which is crucial for oscillation analysis.

With the development of a monitored neutrino beam, the ENUBET (Enhanced NeUtrino BEams from kaon Tagging) project aims at producing a pure, intense and well-controlled source

of electron neutrinos, in order to achieve a $\mathcal{O}(1\%)$ precision on the neutrino flux determination [49–54].

1.5.1 Beamline and instrumented decay tunnel

In the ENUBET project, the pions and kaons produced by the primary protons hitting the fixed target are then focused and transferred through a 40-meter-long instrumented decay tunnel. As a result, K_{e3} decays ($K^+ \rightarrow e^+ \nu_e \pi^0$) becomes the principal source of ν_e, accounting for 97 percent of the entire ν_e flux. The primary goal of ENUBET is to measure the large-angle leptons produced with the neutrinos in kaon decays using calorimeters placed inside the decay pipe. Extending its original physics reach, ENUBET can also detect large-angle muons from $K_{\mu 2}$ ($K^+ \rightarrow \mu^+ \nu_\mu$) and $K_{\mu 3}$ ($K^+ \rightarrow \mu^+ \pi^0 \nu_\mu$) decays, as well as monitor muons from pion decays ($\pi^+ \rightarrow \mu^+ \nu_\mu$) employing muon monitor stations after the hadron dump. The layout of the ENUBET facility is described in Fig. 1.4.

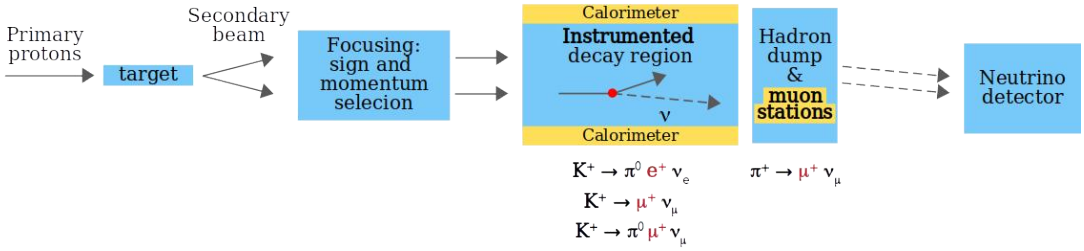

Figure 1.4: Layout of the ENUBET neutrino beam.

ENUBET will be built as a Narrow Band Beam (Sec. 1.2.1) so to have a small energy range and low background at the neutrino detector for a high precision cross-section measurement. In an NBB, the small momentum width of the beam allows for accurate measurement of the neutrino energy on an event-by-event basis. Thanks to the two-body decay kinematics of pions and kaons, the ν_μ energy is correlated to the position of the interaction vertex. Thus, the measurement of neutrinos at a certain distance from the beam axis provides a precise indirect measurement of the neutrino energy. This is what is called the "Narrow band off-axis technique" (NBOA), and can reduce the systematic budget due to the bias in the energy reconstruction at the detector

This would allow to determine the ν_μ energy at source. This study has been conducted using a full particle tracking and interaction simulation of the ENUBET facility. Assuming a 500 ton liquid Argon detector placed at 50 m from the hadron dump and with a transverse area of 6×6 m^2, and assuming 4.5×10^{19} POT (protons on target), the expected number of ν_μ^{CC} interactions observed at the detector have been estimated to be 4×10^5. Their distribution is shown in Fig. 1.5, black line. The selection of neutrino interactions at different distances from the beam axis (coloured lines in Figure) allows the ν_μ energy reconstruction. The pion (low energy peak) and kaon (higher energy peak) components of the spectra are well separated, and the peaks provide an estimation of the incoming neutrino energy.

Moreover, considering the pion decays, Fig. 1.6 shows the precision of the determination of

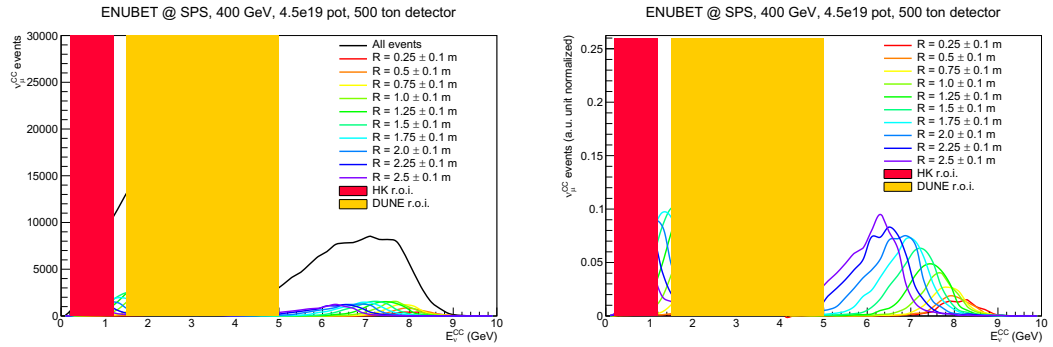

Figure 1.5: ν_μ^{CC} interactions, total (black line) and for interactions at different radial distances R (left); normalized spectra also shown (right). The detailed detector response is not included.

the neutrino energy from the width of the peaks. It ranges from 8% to 25% in the DUNE energy range, for which the ENUBET beam is optimized. It amounts instead to 30% in the Hyper-K region. Ongoing studies on a beamline that can enrich the low-energy part of the spectrum will bring possible performance improvements.

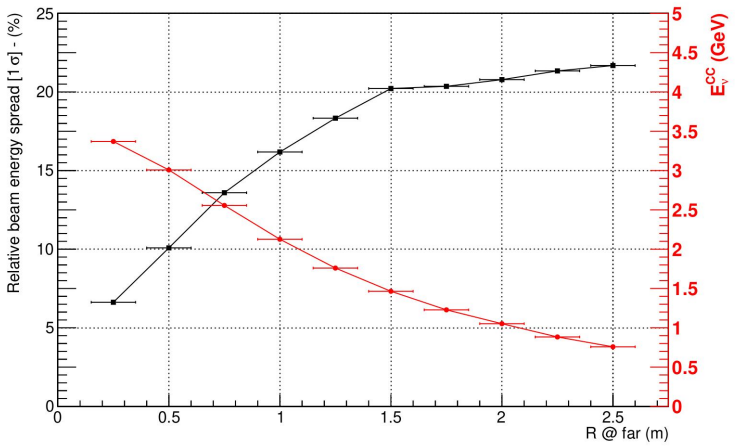

Figure 1.6: Depending on how far the interaction vertex at the detector is from the beam axis (R), the beam energy spread (black) and peak energy (red) are shown [51].

The ENUBET beamline simulations deal with the optimization of the beam parameters. Protons from 400 GeV (CERN-SPS), 120 GeV (Fermilab Main Ring), and 30 GeV (JPARC) accelerator complexes have all been simulated to estimate the secondary yield with various targets. The target design aims to maximize the number of produced kaons per proton on target (POT). The momentum of secondary particles has been adjusted to 8.5 GeV, with a 5-10% momentum bite, in order to fulfil the requirements of the neutrino beam and the reconstruction capabilities of tagger instrumentation.

Over the years, an extended test beam campaign lead the collaboration to the final design of the instrumentation for the decay tunnel, which consists of a modular calorimeter with an integrated photon veto, read out by Silicon Photo-Multipliers (SiPMs). Chapter 2 describes in detail the implementation of the ENUBET secondary beamline, while in Chapter 3 the instrumentation of the decay pipe is discussed, and the different technologies that were tested are summarized.

1.5.2 Background at the decay tunnel level

The ENUBET project plans to exploit the large angle decays of mesons in order to monitor the production of the associated neutrinos (as an example, Fig. 1.7 shows that the mean emission angle of positrons from the K_{e3} decays in the ENUBET beamline is 88 mrad). However, the tunnel walls will be hit also by the products of other kaon decays and other background particles transported by the transfer line to the tagger.

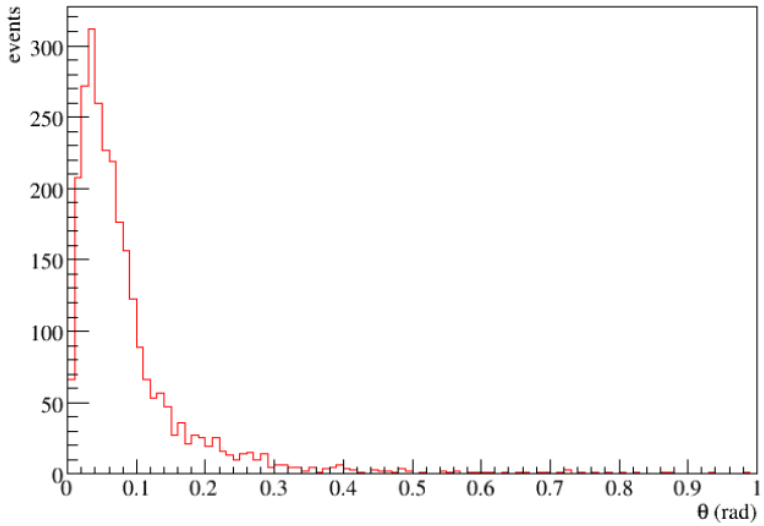

Figure 1.7: Angle distribution of the positrons from K_{e3} decays, for 10^5 K^+ with average momentum of 8.5 GeV at the entrance of the decay tunnel [49].

Tab. 1.6 summarizes all the background sources. Positron, pion and muon separation is possible thanks to the instrumentation of the decay tunnel: they are identified using calorimetric techniques. The detector designs have been extensively validated by dedicated GEANT4 simulations and experimental measurements. The energy resolution request on the calorimeter for positron tagging and e^+/π^+ separation in the range of interest of 1-3 GeV is $\frac{\sigma_E}{E} \leq \frac{25\%}{\sqrt{E}}$ [55]

Positrons coming from muon decays in flight represent another source of background. Given that kaons have a shorter lifespan than pions and muons, this contamination can be minimized with a short beamline and high secondary momentum. A beamline with a focusing section of a few tens of metres and a decay tunnel of 40 m would stop at the hadron dump a significant amount of undecayed pions and muons while enabling the decay of enough kaons.

Decay	BR (%)	Identification
$\pi^+ \rightarrow \mu^+ \nu_\mu$	∼100	muon stations (hadron dump)
$K^+ \rightarrow \mu^+ \nu_\mu$	63.55	tagged in the tunnel
$K^+ \rightarrow \pi^+ \pi^0$	20.66	background
$K^+ \rightarrow \pi^+ \pi^+ \pi^-$	5.59	background
$K^+ \rightarrow e^+ \pi^0 \nu_e$	5.07	tagged in the tunnel
$K^+ \rightarrow \mu^+ \pi^0 \nu_\mu$	3.35	tagged in the tunnel
$K^+ \rightarrow \pi^+ \pi^0 \pi^0$	1.76	background
$\mu^+ \rightarrow e^+ \bar{\nu_\mu} \nu_\mu$	∼100	background

Table 1.6: Signals and backgrounds in the ENUBET decay tunnel.

1.5.3 Detector simulation

The ENUBET collaboration [56] developed a full GEANT4 simulation of the instrumented tagger, with a detailed implementation of the calorimeter modules and the photon veto layer. The simulation takes into account particle propagation and decay inside the tunnel and up to the hadron dump. A separate simulation of the transfer line provides the initial particle distributions at the tunnel entrance. The scintillation process and light propagation are not taken into account while simulating the hit level response of the tunnel detectors. To give more accurate hit digitization, a waveform simulation based on the hits on the tagger and the SiPM response has been developed [57]. The tagger response at the single channel level is simulated to evaluate the impacts of pile-up on the overall detector performance. A conversion factor (15 photo-electrons/MeV) derived from earlier test beam data on tagger prototypes is applied to each visible energy deposit coming from the simulation before it is translated into photons that strike the SiPM. The SiPM response is then simulated, and the waveforms produced are analysed by a pulse detection algorithm, which provides the time and the amplitude (converted back to MeV) of the processed peaks. The waveform analysis provides a realistic estimate of the effects of the pile-up on the overall detector performance. The information from the simulation of the detectors is used for event reconstruction, to monitor lepton production at the single-particle level. Overall, the rate at the decay tunnel should not surpass O(1) MHz/cm^2.

1.5.4 Particle identification

The event reconstruction process [55] is carried out by a neural network (NN) developed using the TMVA toolkit [58]. The assessment of the overall performance of ENUBET is carried out separately for positrons and muons. The variables employed by the NN are constructed from the energy deposit in each module of the calorimeter simulation described in 1.5.3. The ENUBET Event Builder (EB) then defines an event, starting from a "seed" calorimeter module and then clustering neighbouring ones, taking into account their position and timing. In the positron case, the seed is the module with the largest energy deposit and of energy greater than 28 MeV. The NN relies on the pattern of energy deposition in the calorimeter through a set of 19 variables (energy pattern deposition in the calorimeter, event topology) to separate positrons from pions

and muons. The photon discrimination is possible thanks to the photon veto energy deposition as an additional variable. For muons, the seed is identified with a dedicated EB as the inner layer module with energy between 5 and 15 MeV. The background separation is performed by exploiting 13 variables (energy deposition, track isolation and topology). The NN allows monitoring positrons (Fig. 1.8a) with an efficiency of $\sim$22% and signal-to-noise of $\sim$2, while large-angle muon monitoring (Fig. 1.8b) is reached with an efficiency of $\sim$34% and signal-to-noise of $\sim$6.

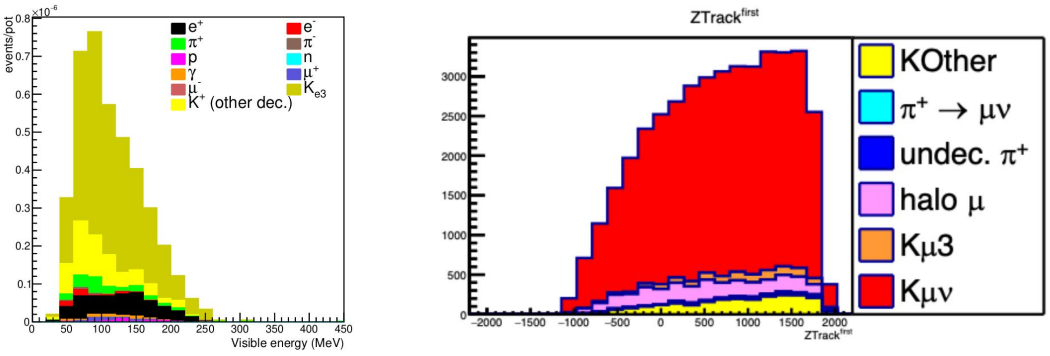

(a) Positron energy

(b) Muon impact position

Figure 1.8: Example of signal identification after the NN discrimination. Left: energy of positrons from K_{e3}, gold. Right: impact point on tagger of muons from $K_{\mu 2}$, red.

1.5.5 Reduction of the systematic uncertainty on the flux

As previously stated, one of the major systematic uncertainties in neutrino physics appearance/disappearance experiments is the normalization of the original flux of neutrinos. By means of monitoring the leptons from meson decays it is possible to constrain the nuisance corresponding to the neutrino flux. In the procedure described in [59], the uncertainties on the hadron flux, such as the different population of charged kaons, charged pions, protons, etc, are propagated to the uncertainty on the neutrino flux. The measurement of kinematic distributions of charge leptons in ENUBET allows the discrimination between the different parent particles, and such constraining the original flux of hadrons. In order to achieve this goal, the lepton tagging is used, not only to identify the lepton flavours but also to measure their energy and directions. Toy MC experiments are simulated for different charged hadrons populations and they are fitted thanks to the measured observables in ENUBET. The uncertainty on the propagation of charged mesons to the ENUBET detector is also taken into account in the expected improvement in the knowledge on the neutrino flux, it is then very important to properly simulate the evolution of particles inside the beamline.

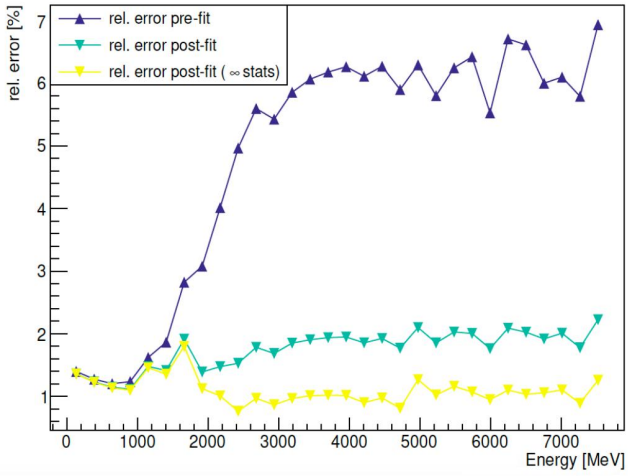

Figure 1.9: Hadro-production systematic uncertainty reduction on the electron neutrino flux. Before constraint: the systematics amount to $\sim$6% (blue), which get reduced to $\sim$1% thanks to the ENUBET tagger constraints (yellow, in the limit of infinite statistics). The green line corresponds to the available simulated data of 600 MPOT.

Chapter 2

Development and optimization of the ENUBET beamline

This Chapter describes the development of a GEANT4 simulation of the ENUBET beamline. The starting point of this thesis work is an existing simulation implemented by the Collaboration in G4beamline. I have implemented an independent GEANT4 simulation that is currently the backbone for the physics simulation of the project. The GEANT4 software is object-oriented, has open-source code, and is built on the C++ programming language. The advantage of GEANT4 over other simulation tools is that it allows for extensive code customization, providing the user with full control over every aspect of the simulations. My PhD research involved the implementation of various beamline configurations and the study of different choices of materials and collimators, which are covered in Section 2.2. The current code implements the possibility of following the history of tracks, thus enabling the full characterization of systematics on the neutrino flux. Moreover, one of the improvements in the simulation is in the description of the magnetic fields. The work done in this area is detailed in Section 2.3. Section 2.4 covers the optimization campaign I carried on in order to finalise the beamline that will be used for the future implementation of ENUBET. Section 2.5 presents the results obtained thanks to my studies.

2.1 Motivation and design

The ENUBET beamline is conceived as a narrow band secondary beamline, relying as primary choice on normal conducting magnets. Protons as primary particles hit a target and produce secondaries, that are sign-selected down to the instrumented decay tunnel. The beamline is designed to enhance the ν_e components from the K_{e3} decay and suppress the contamination of ν_e from muon decays and of ν_μ from pion decays. Additionally, it allows the neutrino energy spectrum to fall within the desired region for future long-baseline experiments. As shown in [49], the ratio between ν_e and ν_μ coming from K and π decays is given by

$$R_{\nu_e/\nu_\mu} = R_{K/\pi} \cdot BR(K_{e3}) \cdot \frac{[1 - e^{L/\gamma_K c\tau_K}]}{[1 - e^{L/\gamma_\pi c\tau_\pi}]} \tag{2.1}$$

- $R_{K/\pi}$ is the ratio between K^+ and π^+ produced at the target;
- $BR(K_{e3})$ is the K_{e3} branching ratio ($5.07 \pm 0.04\%$ [7]);
- L is the length of the decay tunnel;
- $\tau_{K,\pi}$ and $\gamma_{K,\pi}$ are the lifetimes and the Lorentz factors of kaons and pions.

Assuming a K/π ratio of $R_{K/\pi} \sim 10\%$, Fig. 2.1 shows the scaling of ν_e/ν_μ of Eq. 2.1. It is possible to improve the ratio between the ν_e from K_{e3} decays and the ν_μ from pion decays by increasing the energy of the secondaries and shortening the length of the decay tunnel (Fig. 2.1, black lines). Moreover, the ν_e beam contamination from muon decays in flight is also reduced (Fig. 2.1, red lines).

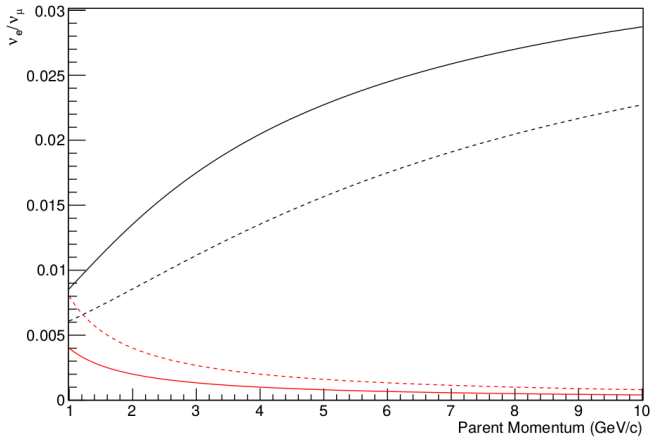

Figure 2.1: Ratios of ν_e and ν_μ fluxes as a function of secondary beam momentum (black) and from muon decay in flight (red). Continuous/dashed lines correspond to a decay tunnel length of 50/100 m. Figure from [49].

The ENUBET beamline is developed taking into account a variety of criteria, including:

- increase the amount of K^+ in the desired momentum range at the tunnel entrance;
- create a small enough beam size so that non-decaying particles can leave the decay pipe without hitting the tagger's inner surface;
- reduce the total length of the transfer line to around 20 m to mitigate kaon decay losses before the entrance of the decay tunnel (kaons' decay length is $\beta\gamma c\tau \simeq 63$ m at 8.5 GeV/c);
- maintain under control the amount of background delivered to the tunnel, which influences the signal-to-noise ratio of the positron selection;
- prioritize the use of standard magnets (normal-conducting devices with apertures below 15 cm).

The optics of the ENUBET reference beamline is currently optimized for a hadron beam with a momentum of 8.5 GeV/c and a momentum bite (half of the total momentum range) of 5-10%. This choice was influenced by the requirements of ν_e contamination, the total number of secondary kaons (see Fig. 2.2) and, as mentioned in Ch. 1, of e^+/π^+ separation at tagger level. It leads to a ν_e beam peaked at an energy of 4 GeV, which covers the energy range of interest for DUNE. Other designs, with secondary energies centred on the Hyper-Kamiokande range, are also under consideration [60].

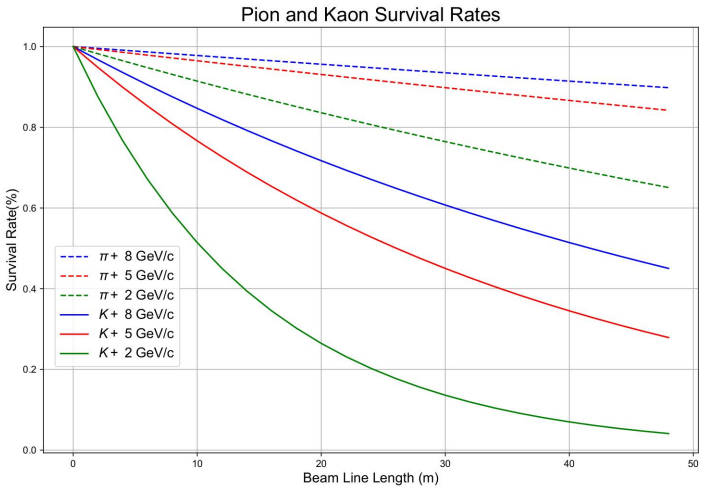

Figure 2.2: Survival probability of pions and kaons produced in neutrino beams below 10 GeV/c as a function of the beamline's length [61].

2.1.1 Slow extraction

Fast extraction of protons, which is the extraction method most commonly used in neutrino beam experiments, is incompatible with ENUBET because of the monitoring of the kaon decay products at single particle level in the decay tunnel. In order to avoid detector saturation due to pile-up at the instrumented decay tunnel, the maximum hit rate must be within $\mathcal{O}(1\ \text{MHz/cm}^2)$. The fast-extraction method is employed to extract the full circulating intensity from a synchrotron, generally in a time of tens of microseconds. While studies on waveform processing and signal reconstruction are now being conducted to further understand the performance restrictions caused by pile-up, ENUBET can not sustain by far the particle rate resulting from a fast proton extraction. This leaves the slow extraction of the primary protons as the ideal extraction method for ENUBET. In a slow extraction scheme, the full intensity of a synchrotron is continuously extracted over times up to a few seconds.

Among the high-energy synchrotons that are and can be used for neutrino beamlines, the CERN-SPS has been selected as an ideal proton driver for ENUBET because of its proton momentum of 400 GeV and maximum slow-extracted intensity of $4.5 \cdot 10^{13}$ protons. Assuming these numbers, a good choice for ENUBET would be an extraction length of 2 s, which would lead to an average of one decay observed every 4 ps at the tagger. This solution would require

implementing a beamline composed of normal conducting magnets. Conversely, the use of a strong focusing device as a magnetic horn would require the same intensity to be extracted in ms-long pulses, so as not to overheat the horn. An example of the two possible proton extraction schemes proposed by ENUBET is shown in Fig. 2.3. In the standard continuous slow extraction

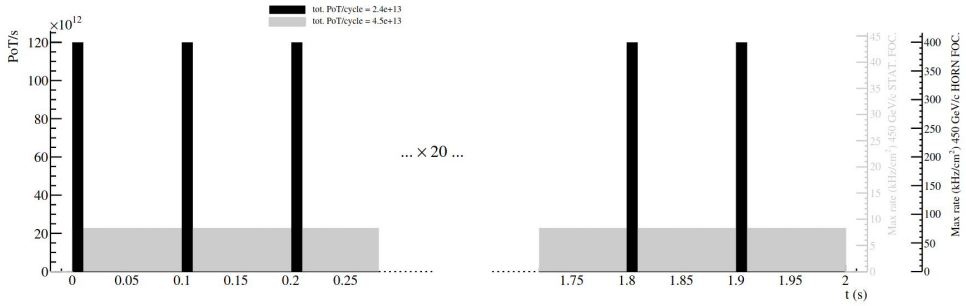

Figure 2.3: Proton extraction schemes for the ENUBET project, standard continuous slow extraction (grey) and slow resonant extraction (black). From [50].

(in grey in figure) the same proton intensity is constantly extracted over a period of 2 seconds. With this option, a transfer line made of dipoles for momentum selection and quadrupoles for focusing carries the secondary beam to the entrance of the decay tunnel. This kind of transfer line is referred to as a "static". The ENUBET collaboration proposed also a resonant extraction technique in order to include the possibility of using a horn. A magnetic horn is a pulsed focusing device that would need to be pulsed with large currents for 2-10 ms at a repetition rate of 10 Hz during the accelerator flat-top. This "burst slow extraction" (black lines in Fig. 2.3) is compatible with the maximum rate sustainable by the calorimeter.

A fully static beamline employing standard normal-conducting magnets is the ENUBET baseline option, with the important advantages of cost-effectiveness, straightforward implementation, stable operation, and a low particle rate. However, this implies increasing the detector exposure (in ton×years) to make up for the reduction in yield with respect to a horn-based beamline. In order not to discard the option of using a magnetic horn that could increase the statistics, a pulsed slow-extraction method at CERN-SPS has been successfully developed [62] and a dedicated horn-based version of the beamline is currently being investigated [63].

2.1.2 Beamline optics

The K/π secondary beam is designed to have an average momentum of 8.5 GeV, with a momentum bite of 10 percent. The design of the optics is performed with TRANSPORT [64], which is a matrix-based tool for beam optics calculations that can be used for designing static beamlines. A beamline is defined as a sequence of magnetic elements placed along a certain reference trajectory. One can also specify the drift spaces between them, as well as parameters for the input beam or specific magnet configurations. The reference trajectory is used to represent the path travelled by a charged particle with the design momentum of the beamline and no transversal motion as it travels through idealised magnets. The coordinate longitudinal to

the initial reference trajectory is typically named z, while the transverse coordinates are x and y, with bending magnets that bend in the horizontal plane. TRANSPORT calculates the beam's attributes element by element as it proceeds through the beamline, showing the beam envelope and giving the length and field of quadrupoles and dipoles. The beam optics is designed by trying to keep the total transfer line length as short as possible, use realistic magnets (in terms of length, aperture and field), and keep the $8.5 \pm 10\%$ GeV beam within the magnet apertures and decay tunnel walls. The resulting magnetic lattice is then implemented in G4beamline [65] in order to insert collimators that match the beam envelope and proper absorbers and shielding and to quantitatively estimate and optimize the background level at the decay tunnel walls. Fig. 2.4 shows an example of the TRANSPORT implementation of the ENUBET beamline.

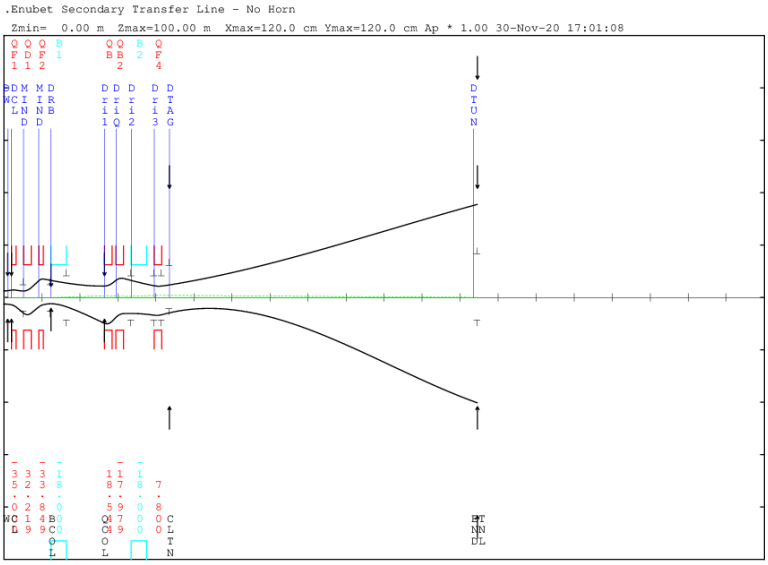

Figure 2.4: TRANSPORT beam envelope for the ENUBET beamline. Magnetic elements, i.e. quadrupoles (red) and dipoles (light blue) are shown.

2.2 GEANT4 description of the beamline

GEANT4 [66–68] is one of the several multipurpose Monte Carlo codes available for the simulation of the passage of particles through matter. The GEANT4 toolkit adopts an object-oriented technology based entirely on the C++ language and its source code is open. Many experiments employ it in a wide range of areas, including high energy physics, astrophysics, medical physics and radiation protection. It is particularly well suited to high-energy physics, where there is a great need for complex geometries, physical models, and highly customizable codes. The GEANT4 code is quite complex since it can represent a broad variety of processes, while also being quite flexible: this is a direct consequence of the user directly accessing and using the code as any other C++ framework or library, without having to interact with it through an additional layer of abstraction, as a custom high-level set of instructions that then speaks to the source code

(this is rather common in these type of software, see for instance G4beamline and FLUKA, and GEANT4 stands out because of this). Commonly used software codes for beamline description are FLUKA [69,70], G4beamline [65], and MARS [71]. FLUKA is another particle tracking and interaction code that is extensively used for facility design for energy deposition, radiation damage and shielding activation studies. G4beamline is optimized for beamline design. It is based on the GEANT4 toolkit, wrapping up the low-level C++ part into a custom high-level interface: this makes the simulation description proportional to the simulation's complexity (i.e. typically simpler), as opposed to a substantially more sophisticated customized C++ program. However, the strength of GEANT4 is that it gives the user the ability to fully customize the code, giving complete control over any part of the simulations. For instance, not only it is possible to control all the geometrical parameters, as well as the eventual electromagnetic field description, but also to directly access and modify the inner structure and workings of the particle tracking process and particle information. Moreover, also the structure of the output file is completely customizable and can be adapted to the user's needs. This made ENUBET choose GEANT4 as one of the codes used for the simulations and validations of its whole beamline and detectors, which will be extensively described in the present work.

In order to better understand the more technical results that will follow, it is important to spend some words on the architecture and inner workings of GEANT4. There are three mandatory classes that the user must define in a GEANT4 application. First, the "Physics List", where all particles and physics processes that will be used in the simulation are specified. There are some reference Physics Lists available, the current ENUBET default is FTFP_BERT. FTFP_BERT is recommended for simulations in which hadron production and interaction play an important role, as it is the case for a secondary beamline. It is based on the Bertini Cascade model [72], that handles the interactions of hadrons up to a few GeV, and the Fritiof [73] model, that handles the same particles at higher energies. FTFP_BERT is based on well consolidated models that have been extensively tested [74,75] and this Physics List is now one of the most commonly used in high energy physics. The "Detector Construction" class is used to describe the detector geometry and materials. The largest volume is called "World" and it must contain all the other volumes. Each volume is created by describing its shape using "solids" (as `G4Box` for boxes or `G4Tubs` for cylinders) and its physical characteristics, such as material or magnetic fields associated with it, using a logical volume. The material definition can go from scratch, specifying atomic and mass numbers, density, and state information, or through the fractional composition of constituent elements, or using a rich database of existing materials. The object is then placed inside a containing volume (either a "mother" volume or the World). The third mandatory class is the "Primary Generator Action". It is called before the start of the event processing and contains information on primary particles' momentum and position. It is possible to generate such particles using GEANT4 or an input file containing the necessary information. Customizable classes are:

- "Run Action": represents a `Run`, which is the largest unit of simulation and contains many `Events`. All the geometry, fields and physics are fixed within a single `Run`. Histograms, variables of interest and other means for calculations are created at this level and then are written to the output;

- "Event Action": an `Events` processes primary particles. The Event Action loops on `Track` (particles) and stores the desired information on the output histograms or trees;
- "Tracking Action": when a `Track` (a new particle) is created, the Tracking action takes place. Each `Track` processing consists of multiple `Step`;
- "Stepping Action": each `Step` is the smallest unit of the simulation and it represents what has changed, e.g. the distance travelled by the particle and the amount of energy deposited.

Based on a previous simulation in G4beamline developed by the ENUBET collaboration, an independent simulation of the ENUBET beamline has been implemented in GEANT4. The implementation of a highly versatile simulation in GEANT4 allows for the management of all system parameters through external control cards (i.e. simple readable ASCII files). This has paved the way for a more systematic beamline optimization in line with the requirements of the ENUBET project.

2.2.1 Preliminary studies on the ENUBET beamline

The ENUBET facility is implemented in the Detector Construction class by defining materials and geometry: this has been made easily controllable by combining default and user-defined commands in an external macro file, that is an ASCII file containing user interface commands. The macro files can be processed either in batch mode or interactively. This is particularly useful during the design phase of a project since it is not necessary to re-compile the application after modifying, for example, a geometrical parameter or the position of a beamline element.

Each simulation runs using as input files the output of a previous FLUKA simulation of the primary proton interactions (based on the SPS 400 GeV protons) with the target. The statistics accumulated is conventionally reported in terms of POT (protons on target). The simulations of the possible ENUBET targets typically consist of a few hundred MPOT up to a maximum of 1 GPOT, due to storage space reasons. The simulation runs on the available resources at the computing centre CC-IN2P3 in Lyon [76], using the Grid Engine (GE, active until March 2022) and SLURM (available from the beginning of 2022) batch-queuing systems. They allow submitting a portion of the total available statistics as parallel jobs, thus reducing the simulation time sensibly. The fact that mutual interactions between particles (e.g. space charge) are negligible in such a system and are not taken into account by the GEANT4 simulation, makes the problem particularly suited for the High Throughput Computing (HTC) case: thousands of jobs at a time can be launched simultaneously and independently on the computing cluster, significantly lowering the simulation times.

The preliminary layout of the ENUBET hadronic beamline is shown in Fig. 2.5. This simulation does not include the full description of the tagger instrumentation, since it would have been significantly heavier and more complex from a computational point of view. The tagger (yellow in figure) here is represented by a hollow Iron cylinder 40 meters long, with a diameter of 1 m. It consists of one bending dipole (orange) with a 1.8 T field that produces a 7.4-degree bending angle. The first quadrupole triplet (grey) serves as an initial focusing system, while the other 3 quadrupoles are used to constrain the beam envelope within the decay tunnel. The total

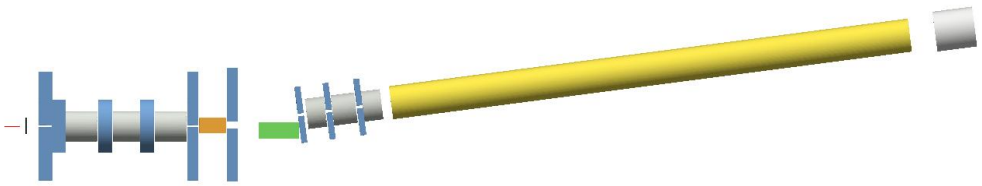

Figure 2.5: GEANT4 layout of the first ENUBET secondary beamline.

configuration in terms of focusing (F), defocusing (D), and bending (B) magnets is FDF B FDF. Each magnet has a 15 cm aperture.

The first target considered is a Beryllium cylinder 1.1 m long, with a diameter of 3 mm. This target has been later replaced with a graphite target of 1.4 m, which offers higher yields of K^+. Double-slit and hollow-cylinder collimators (blue) are made of Iron. A thin (5 cm) Tungsten absorber ("W foil", black) is placed downstream of the target in order to filter out positrons coming from the target itself. The total length of the beamline, from the target to the beginning of the decay region, is about 20 meters. A simple cylinder placed at the end of the decay tunnel serves as a hadron dump (light grey), while a proton dump (green) for stopping non-interacting protons is placed on-axis with respect to the incident 400 GeV proton beam.

The GEANT4 code allows saving information about particle decays and interactions at different stages of the simulation. For this purpose, some virtual detectors are placed along the beamline, at the decay tunnel entrance, walls, exit, and a few tens of meters downstream of the hadron dump, where the neutrino detector could be placed (they are not shown in Figure). The most important quantities that can be extracted by the simulations are:

- the fluxes of kaons and pions at the tunnel entrance in the ENUBET momentum range;
- the overall particle distributions at the tagger entrance;
- the signal and background components on the tunnel walls;
- the neutrino spectra at around 50 m from the end of the decay tunnel (i.e. where a short baseline neutrino detector could be placed).

The exact position, material composition and dimensions of the elements for this beamline version (e.g. the proton dump) were not fully optimized. This beamline is unrealistic: it features only one dipole and the collimators are wide open (i.e. $\gtrsim$ the magnets apertures). The design has not been completed since a new version has been developed to improve beam containment and decrease off-momentum background.

2.2.2 ENUBET beamline design

The beamline described in Sec. 2.2.1 has been improved in an effort to decrease the beam halo background, particularly from muons, and the untagged neutrino component at the far detector

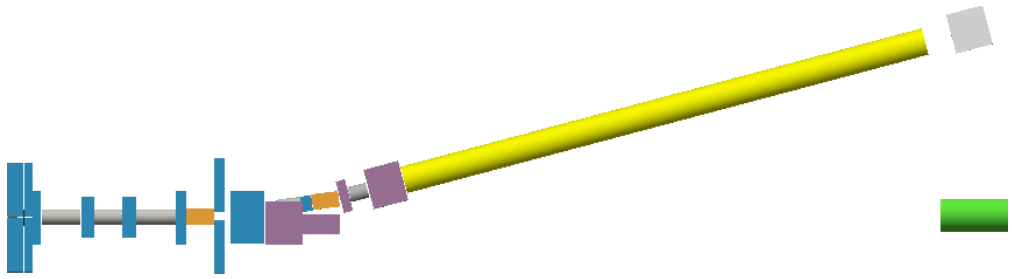

Figure 2.6: First design of the ENUBET double dipole beamline.

(which means that neutrinos created in the transfer line's straight section have a lower probability of reaching the detector), thanks to a larger bending angle.

This new beamline, also called the TLR5_v5 version[1], is depicted in Fig. 2.6. It contains all normal-conducting magnets: a quadrupole triplet for initial focusing of the secondary beam (in grey), a double bend momentum selection section composed of two bending dipoles (orange) with a momentum collimator (blue) and a quadrupole in between (grey, covered by the collimators). The dipoles each have a 1.8 T magnetic field, providing 7.4°each for a total bending of the beam with respect to the primary protons axis of 14.8°. A final quadrupole after the bending section is used to correctly focus the beam into the decay tunnel. The magnets have an aperture of 15 cm and are made of Iron.

The targets separately employed as inputs of this beamline are a Graphite and an Inconel (a Nickel-Chromium alloy) rod, respectively 70 cm and 50 cm long, both 60 mm in diameter. Downstream of the target and before the first quadrupole there is a 5 cm thick Tungsten foil (Fig. 2.7a). Its thickness has been optimized to eliminate most of the positrons generated by the interactions in the target. Collimators in the first part of the transfer line, up to the second dipole, are made of Copper (blue collimators in Figure). A copper block downstream of the first dipole contains two pipes, one is used for the primary 400 GeV protons, and a second tilted pipe (7.4°, as the first bending) transports the ENUBET hadron beam and serves as a momentum collimator for the bending section. In the second part of the transfer line, the collimators are made of Inermet180 (violet). Inermet180 is a Tungsten-Nickel-Copper alloy (respectively 95%, 3.5%, 1.5%) that has much greater machinability than pure Tungsten, a similar density and good shielding behaviour against radiation. Another shielding block around the quadrupole placed between the two dipoles is also made of Inermet180. At the tagger entrance is placed an Inermet180 block 2.65 m long with a conical aperture (Fig. 2.7b). The length and two radii (4.5 cm and 8 cm) of the cone were chosen balancing the reduction of background with the total π^+/K^+ flux. The tagger (yellow) is a 40 m-long hollow cylinder (made of Iron for simplicity, as the full detector geometry has not been implemented in this simulation) and the hadron dump (light grey) is a box made of Iron placed at about 1 m from the end of the tagger. The design of the proton dump (green) is more advanced with respect to the previous beamline (Fig. 2.7c). It is composed of three cylindrical layers: a Graphite core (20 cm in radius, 3 m long), surrounded

[1] In the present work, TLR + number will define a beamline with a specific optic implementation, while the _version will indicate a change in the absorbers, shielding or collimator configuration.

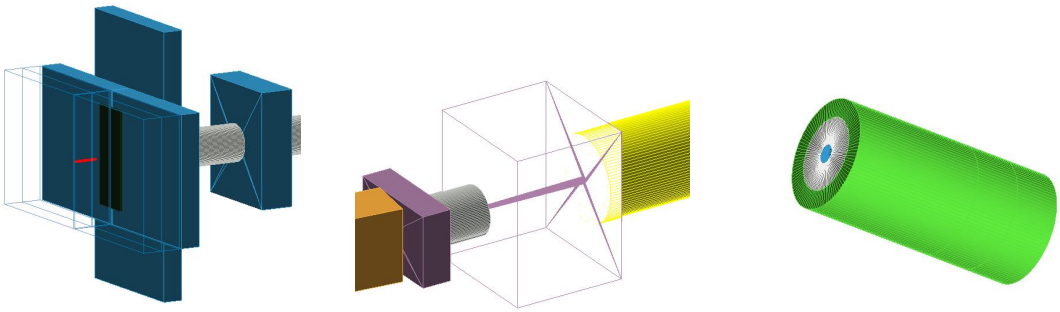

(a) Tungsten foil (black) placed downstream of the target (red).

(b) Inermet180 block (violet) at the tunnel entrance.

(c) 3-layers proton dump: Graphite (blue), Aluminum (white) and Iron (green).

Figure 2.7: Details of the ENUBET beamline elements: Tungsten absorber (a), Inermet180 collimator (b) and proton dump (c).

by Aluminum (a cylinder with an outer radius of 80 cm and a length of 4 m), which in turn is surrounded by Iron (for a total of 1.2 m in radius and 4 m in length).

From the FLUKA studies of ionizing doses and neutron fluence on the elements of the beamline, the design has been updated including proper shielding. The GEANT4 code includes a feature that allows producing automatically the geometry input file for the FLUKA simulation, so as to be able to quantitatively perform detailed shielding studies using the latter program. Figure 2.8 shows how the beamline has been surrounded by concrete.

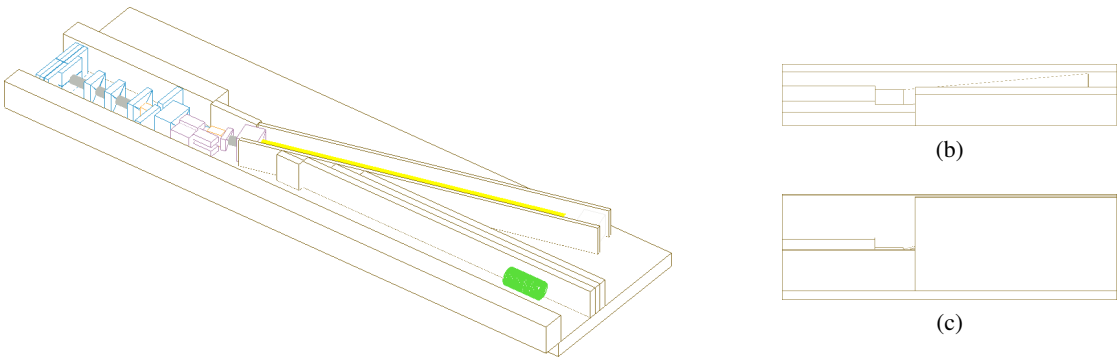

(a)

(b)

(c)

Figure 2.8: The ENUBET beamline is enclosed by concrete, section (a), side view (b) and top view (c).

The simulation output contains all the information useful for many aspects of ENUBET, such as particle production, decay into secondaries, momentum and position of each particle crossing one of the virtual detectors. This is the result of a major code update that will be described in Sec. 2.5. The following Figures contain a general overview of the results obtained with this version of the beamline; there are many applications of the structure of the output files that can

be exploited for the design needs of ENUBET (e.g. see Sec. 2.2.3 or 2.4.2).

The particle rates at the tunnel entrance are shown in Fig. 2.9. The spectra at this stage of the beamline are a good way to evaluate right away the properties of the beam and find any indication of possible implementation problems or bugs in the code. This beamline allows to achieve the following fluxes at the entrance of the decay tunnel: 3.16×10^{-3} π^+/POT and 2.58×10^{-4} K^+/POT in the $8.5 \pm 5\%$ GeV momentum range. As a comparison, the spectra

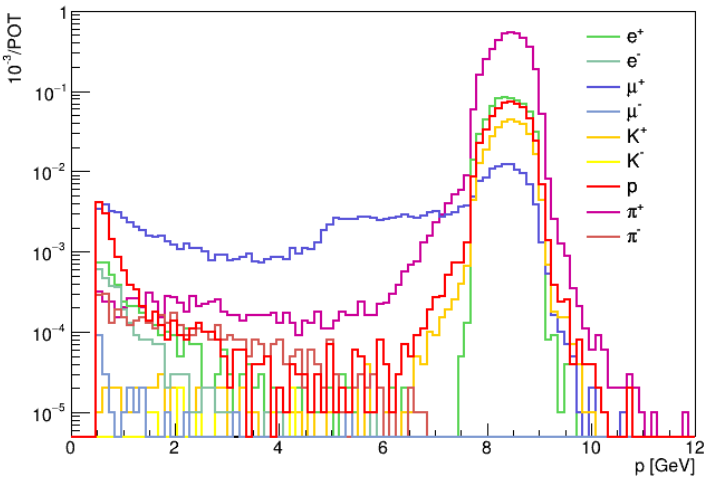

Figure 2.9: Particle budget at the decay tunnel entrance.

obtained with and without the concrete shielding are shown in Fig. 2.10.

At the tagger level, the signal (particles coming from kaon decays in the tunnel region) and background (particles produced in the transfer line and not coming from positron- or muon-producing kaon decays) contributions can be broken down: Figure 2.11 summarizes the momentum and impact point of positrons, pions and muons that hit the tunnel walls.

Figure 2.12 shows the neutrino spectra at a far detector of 6×6 m^2 placed at about 60 meters from the end of the decay tunnel. It is possible to identify the neutrinos produced inside the tagger region (and thus possibly tagged). The GEANT4 simulation of the ENUBET beamline also permits separating the various contributions in terms of flavour and decay process. These are shown in Fig. 2.13. The decay information about the particles simulated throughout the beamline, such as the position of the decay and the parent identification, allows the reconstruction of neutrino rates. The rates in Fig. 2.13 are calculated by weighting the fluxes with the neutrino cross-sections.

2.2.3 Tuning of the beamline parameters

Dealing with a secondary beamline such as the ENUBET beamline is not a simple task. There are many parameters involved for each element: sizes and apertures of collimators, material choice of absorbers, and position of elements. While this is also true for any primary beamline or accelerator, the current case differs for the presence of non-avoidable background and halo

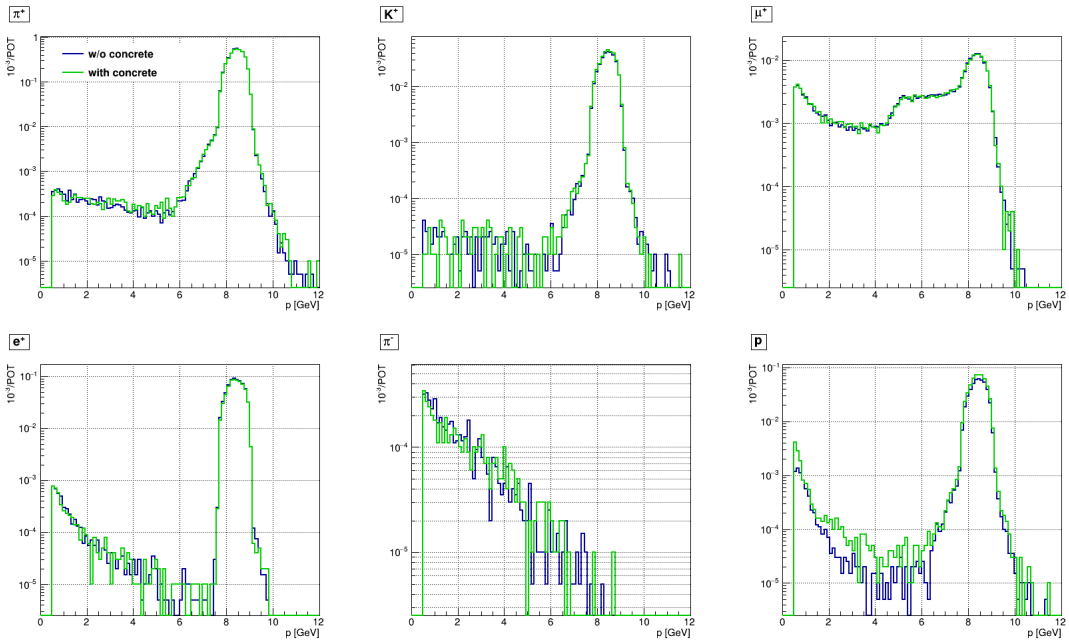

Figure 2.10: Comparison of momentum distributions of particles at the decay tunnel entrance, with (green) and without (blue) the concrete shielding.

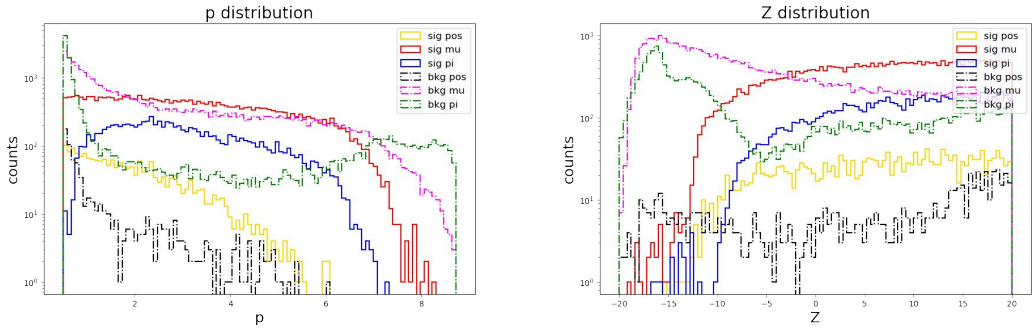

(a) momentum (b) impact point

Figure 2.11: Momentum p (a) and impact point z (b) of particles hitting the tagger walls.

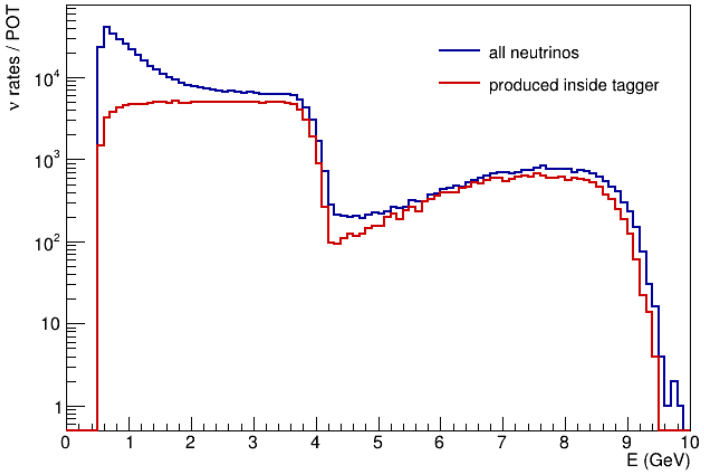

Figure 2.12: All neutrinos at the detector (blue) and neutrinos produced inside the tagger (red).

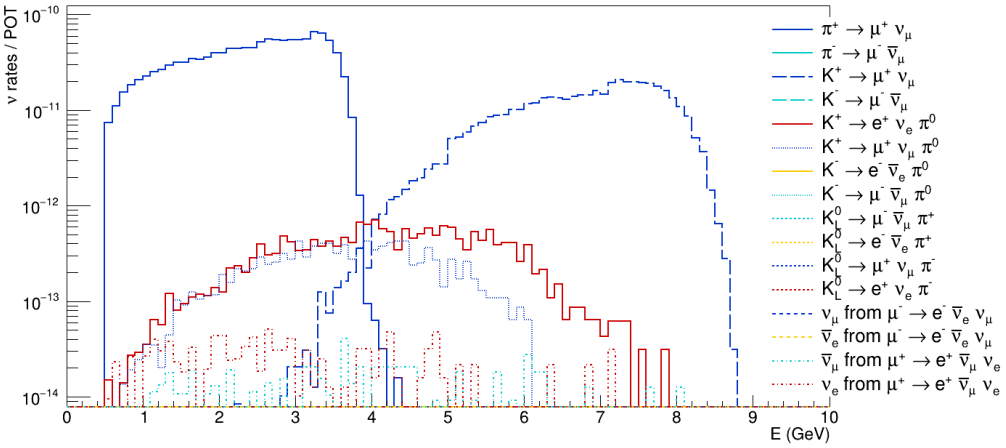

Figure 2.13: Rates at the neutrino detector for neutrinos produced inside the decay tunnel, breakdown by decay mode. These rates have been scaled using the neutrino cross-section.

particles produced from the target at wide angles and transversal coordinates. These particles not only are non-negligible in number and travel along the beam but get multiplied and increased by further particle showers due to the interaction of the beam or other background particles with beamline elements. A quantitative study and design of such beamline hence cannot only depend on a pure optical simulation but has to be passed several times through a full and typically heavy particle tracking and interaction simulation. An interesting study is to look at how the distributions of kaons at the tunnel entrance and background on the tunnel walls change with the tuning of some of the beamline parameters. For this task, a statistics of about 100 MPOT is found to be a good trade-off between acceptable simulation running times and low enough statistical uncertainty in order to meaningfully compare different results.

Regarding the material choice, one of the studies performed concerns the collimators at the end of the transfer line. After the second bending the collimators are made of Inermet180 (a Tungsten alloy). A possible variation is to place Tungsten collimators instead. Figure 2.14 shows the distributions of momentum and entering angle of particles at the tagger entrance, comparing the spectra for the simulation with Inermet180 collimators and the one with Tungsten collimators. There are no evident differences in the distributions, but for statistical fluctuations in counts. The choice of Inermet180 is nevertheless justified by its advantageous properties discussed above.

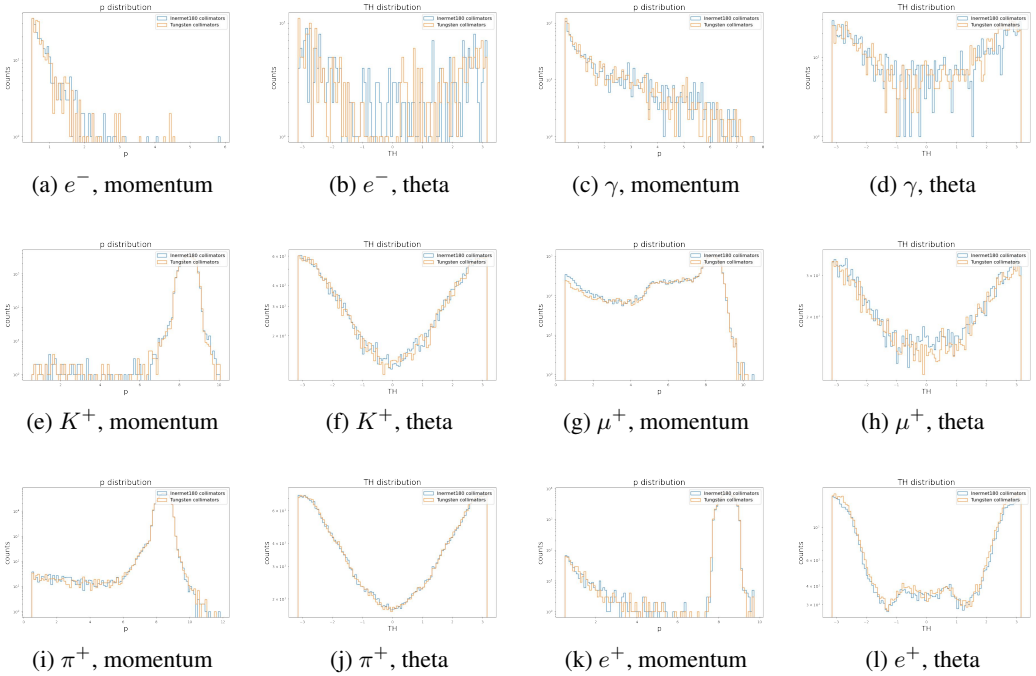

(a) e^-, momentum (b) e^-, theta (c) γ, momentum (d) γ, theta

(e) K^+, momentum (f) K^+, theta (g) μ^+, momentum (h) μ^+, theta

(i) π^+, momentum (j) π^+, theta (k) e^+, momentum (l) e^+, theta

Figure 2.14: Momentum and angular distributions of particles at the tagger entrance level, for Tungsten (blue) or Inermet180 (orange) collimators, for 100 MPOT.

The Tungsten foil at the beginning of the transfer line has been the object of careful analysis. It is placed right after the target and before the first quadrupole triplet, in between the first collimators (see Fig. 2.7a). Its main purpose is to shield the transfer line from positrons that are produced inside the target and that would otherwise be transported down to the tagger, where they would be a background for the K_{e3} positrons. Figures 2.15 and 2.16 show what happens if one tries to remove the foil from the beamline. The amount of positrons reaching the decay tunnel increases by a factor ~ 40 and they largely contribute to the low energy background in the second part of the tunnel. The Tungsten foil does produce positrons itself through gamma conversion, but the positrons coming from the target (labelled as "World" in Fig. 2.17)and reaching the tagger would be much more without it.

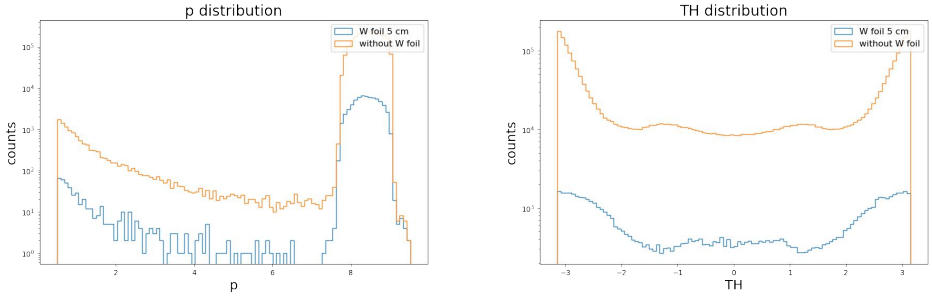

(a) Momentum distribution (b) Angular distribution

Figure 2.15: Positron distributions at tagger entrance, with (blue) and without (orange) the Tungsten foil, for 100 MPOT.

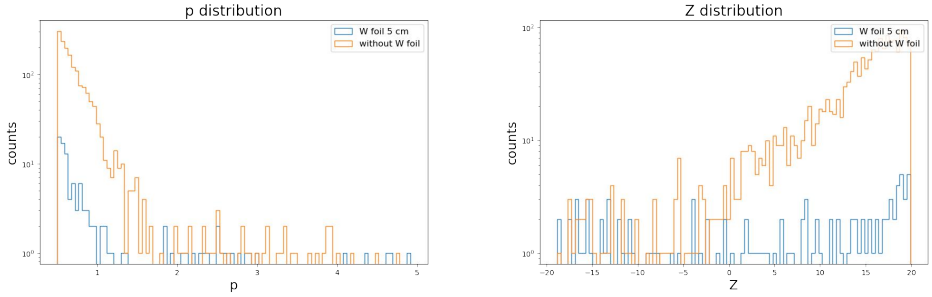

(a) Momentum distribution (b) Impact point distribution

Figure 2.16: Background positron distributions on tagger walls, with (blue) and without (orange) the Tungsten foil, for 100 MPOT.

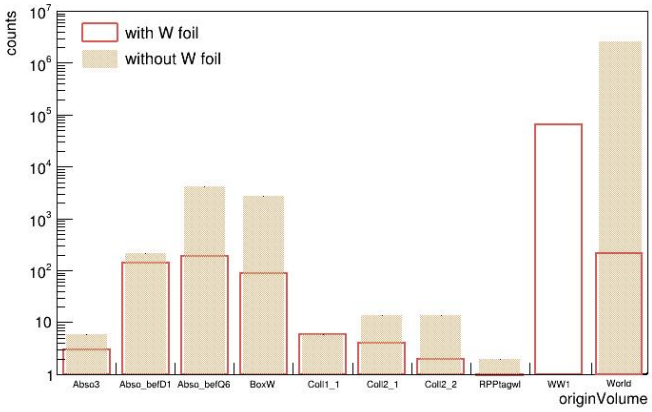

Figure 2.17: Origin of positrons that reach the entrance of the tagger (for 100 MPOT)

This procedure of adjustment and tuning of the most important elements of the beamline has been repeated several times. Given the complexity of the problem, it should be kept in mind that finding the best geometry for a particular element is not trivial and one must be aware of all the possible implications of each adjustment.

2.3 Magnetic fields

Secondary beamlines such as the ENUBET beamline feature several magnetic elements to focus and bend the beam. Therefore it is of great importance that magnetic fields are well simulated in GEANT4.

The ENUBET beamline contains two types of magnets: quadrupoles and dipoles. They have been simplified in the following way:

- a quadrupole (Fig. 2.18a) is represented by a hollow cylinder;
- a dipole (Fig. 2.18b) is made as a hollow rectangular parallelepiped.

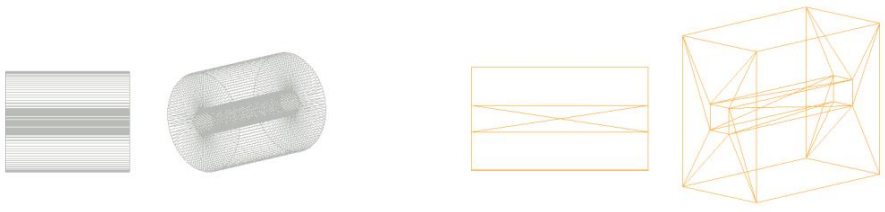

(a) Quadrupole (b) Dipole

Figure 2.18: A quadrupole (left) and a dipole (right) modelled in GEANT4.

In a GEANT4 simulation, uniform or non-uniform electromagnetic fields can be configured and tracks can be propagated inside of them to a certain level of accuracy (more on this in Sec. 2.3.2). The particle's equation of motion in the field is integrated in order to propagate a track inside it. The curved path is divided into linear chord segments, that are chosen so that they closely approximate the trajectory.

The simplest way to create a field is to associate it with a logical volume. The first step is to create a class with one primary method that determines the field value at a given point.

In the case of a quadrupole magnet, the components of the ideal magnetic field in the plane transversal to the beam axis are given by

$$B_x = Ky, B_y = Kx, B_z = 0$$

where z is the beam axis and K is the field gradient. The field is stronger near the edges of the magnet, while at the center is zero. From Eq. 2.3, it can be seen that a quadrupole acts as a transversal focusing or de-focusing element according to the sign of K. It can also be shown that if a quadrupole focuses particles on one axis it de-focuses on the other, but the overall effect of a quadrupole triplet (either FDF or DFD) is a net focusing on both axis.

A dipole produces instead a constant field inside the magnet that can be used to bend a beam and change its reference trajectory. Its components for bending in the x-direction are

$$B_x = 0, B_y = K, B_z = 0$$

Once the field classes are defined in the simulation, they can be associated with any logical volume through the GEANT4 Field Manager class.

In the ENUBET beamline, this has been achieved by creating virtual volumes placed inside the magnets. An empty cylinder is placed inside each quadrupole: it fits the cavity inside the quadrupole so that it does not overlap with the physical volume of the quadrupole. Similarly, there is a parallelepiped inside the hole that creates the dipole cavity. Figure 2.19 shows the magnetic field that has been created in GEANT4 in one of the beamline quadrupoles. These maps have been created by printing out the calls of the "Quadrupole class", i.e. the field value seen by each particle crossing the volume containing the field.

The quadrupole field gradient can be reconstructed with a linear fit of $|\vec{B}|(r)$, as illustrated in Fig. 2.20, showing that the simulation indeed reproduces the desired field in the magnet.

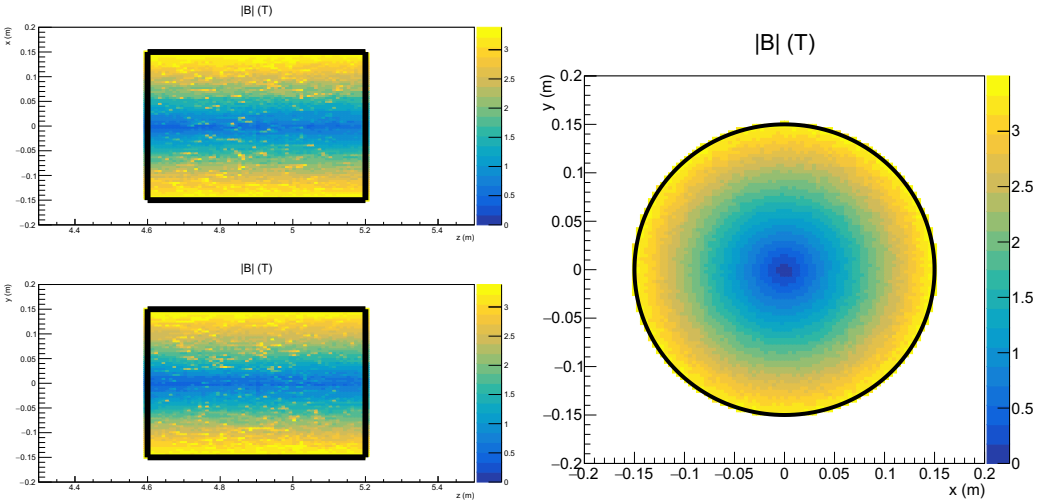

(a) *xz* and *yz* planes

(b) *xy* plane

Figure 2.19: A quadrupole magnetic field simulated in GEANT4 using the method described in Sec. 2.3. Black lines mark the inner cylinder limits. Near the quadrupole's borders, the field is stronger, while it is zero in the middle. These plots have been obtained by simulating 100000 particles from the target through the beamline.

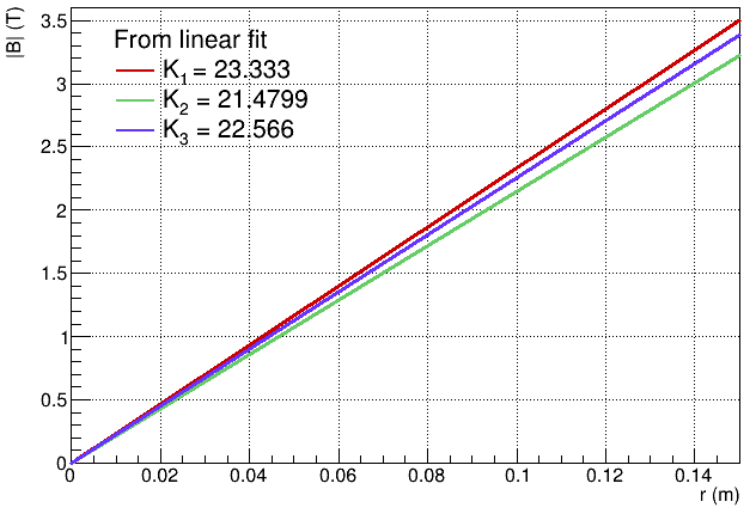

Figure 2.20: Quadrupole magnetic field value as a function of r, for three different simulated quadrupoles.

2.3.1 Fringe fields

A more realistic description of dipole and quadrupole magnets includes the fringe field. The fringe field is the peripheral field that extends outside of the magnet core. In this region, there is a transition from the nominal field to zero, and they can affect the motion of particles passing through magnets.
For simplicity, the fringe field implemented in the GEANT4 beamline simulation extends outside of the magnet aperture only in a cylinder extending the aperture along z.
The drop of the magnetic field outside the magnet volume is described by the Enge function [77]:

$$\frac{1}{1+e^{E(z)}} \tag{2.2}$$

where

$$E(z) = \sum_{n=0}^{5} a_n \left(\frac{z}{D}\right)^n$$

z is the distance from the edge of the magnet ($z = 0$ is on the edge, $z > 0$ is outside the magnet) and is divided by the aperture D. The six a_n coefficients of the Enge function are derived by experiments or models. The maximum extension of the fringe region is calculated from the nominal field length and width.

The main problems with implementing the fringe fields in GEANT4 are the overlapping volumes. Volumes are defined as overlapping when they intersect themselves so that some points in space do not have a distinct identity and belong simultaneously to two separate volumes. In this case, the behaviour of GEANT4 is unpredictable and may lead to wrong simulation results.

The extension of the field region outside of the magnet volume causes overlaps between the volumes that contain the field with several parts of the ENUBET beamline. A new description of the magnetic fields has been implemented to overcome this problem.

The "Dipole" and "Quadrupole" classes derive from a generic "Element" class and contain the description of the dipole and quadrupole magnetic fields. This still needs to be associated with a physical volume, but it is no longer created inside each magnet's volume. A new "Global Field" class is assigned to the GEANT4 Field Manager and can have any number of overlapping "Element" objects added to it. The computation of the field value at a given point hence consists of the following steps:

- a beamline element ("Quadrupole" and "Dipole") derives from the "Element" class and implements the computation of the field for the specific element;
- the constructor of each element in the "Global Field" class contains information on the dimensions and position of the magnet. The "Element" class computes a coordinate transformation, from global to local, so that no field is assigned to points outside of the magnet;
- for a given point the "Global Field" class sums up the contributions from its list of elements, returning the total field value at that point.

In this way, as illustrated in Fig. 2.21, the definition of a global field overcomes the problem of overlapping volumes. Figure 2.22 shows a comparison between the two methods described

for the implementation of the magnetic fields. These are the momentum and z distributions for some of the main signal and background particles in the ENUBET beamline, at the tunnel level, obtained without the application of the fringe fields. The spectra are compatible as expected, given the absence of volume overlaps in this case. It should be noted that the problem of over-

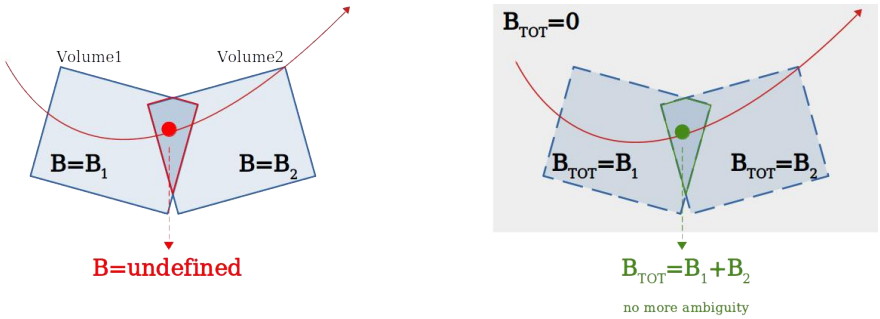

Figure 2.21: The differences in the two methods of field implementation. When a field is added to every single volume (left), a wrong field is assigned to the overlapping region. Thanks to the Global Field method (right), every point in the space has its own field value assigned.

lapping fields is indeed present in the ENUBET beamline; Fig. 2.23 shows that the differences in spectra obtained in a beamline where the fringe fields are not implemented carefully, avoiding the overlap issue, differs significantly.

The following Figure 2.24 is the application of the fringe field to the quadrupole in Fig. 2.19 and to a dipole. It can be seen that the field extends outside of the magnet along its axis. Figures 2.25, 2.26 and 2.27 show the difference in spectra obtained with and without the application of the fringe fields to the simulation.

The differences between the improved simulation and the approximate one are substantial and will require further investigation in the future. Typically, as the modified fields act on the focusing properties of the magnets, a re-design of the optics should suffice to recover the same beam transport properties. In the following studies, the approximate simulation will be used. Regardless, the process and development of the ENUBET beamline have been automatized and scripted to a level in which, when something needs to be changed, the full beamline can be readily re-adjusted to an optimal configuration. Such changes are expected in the development of such a complex and non-ideal facility, and that is why building solid technical tools and methods is of paramount importance.

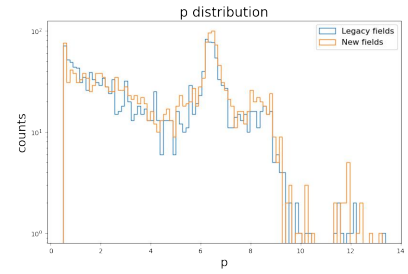

(a) π^+, background

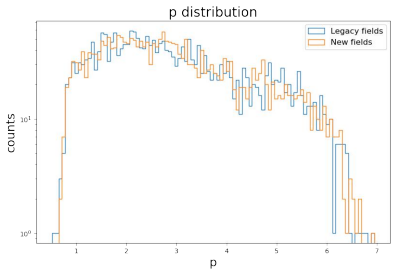

(b) π^+, signal

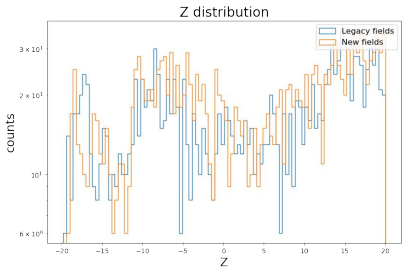

(c) π^+, background

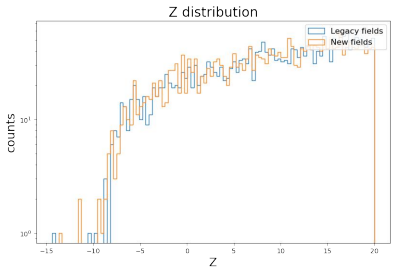

(d) π^+, signal

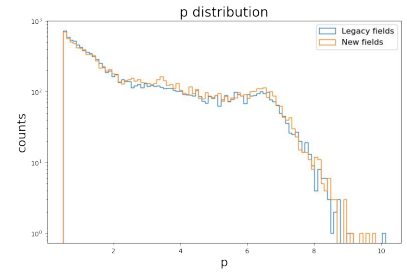

(e) μ^+, background

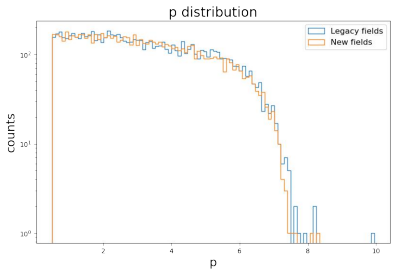

(f) μ^+, signal

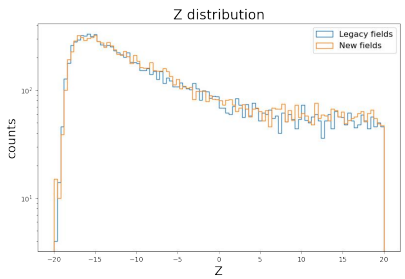

(g) μ^+, background

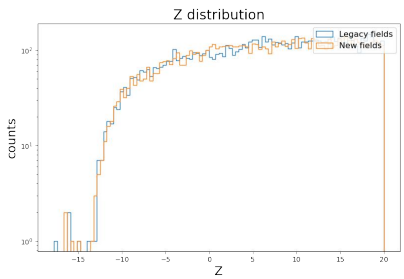

(h) μ^+, signal

Figure 2.22: Momentum and z distributions for background (left) and signal (right) pions (top) and muons (bottom) on the tunnel walls. Blue lines correspond to the spectra obtained with the method of filling volumes with the magnetic field. Orange lines: global field method. Fringe fields are not simulated.

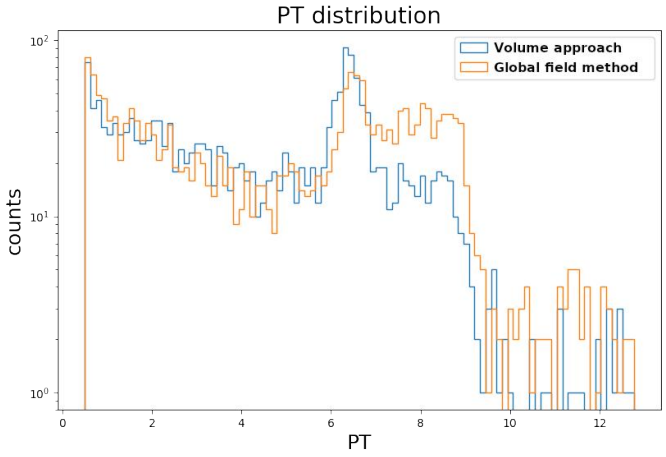

Figure 2.23: Momentum of background pions hitting the tagger walls, for the two implementations of the fringe fields: with the volume approach (blue) and the global field method (orange).

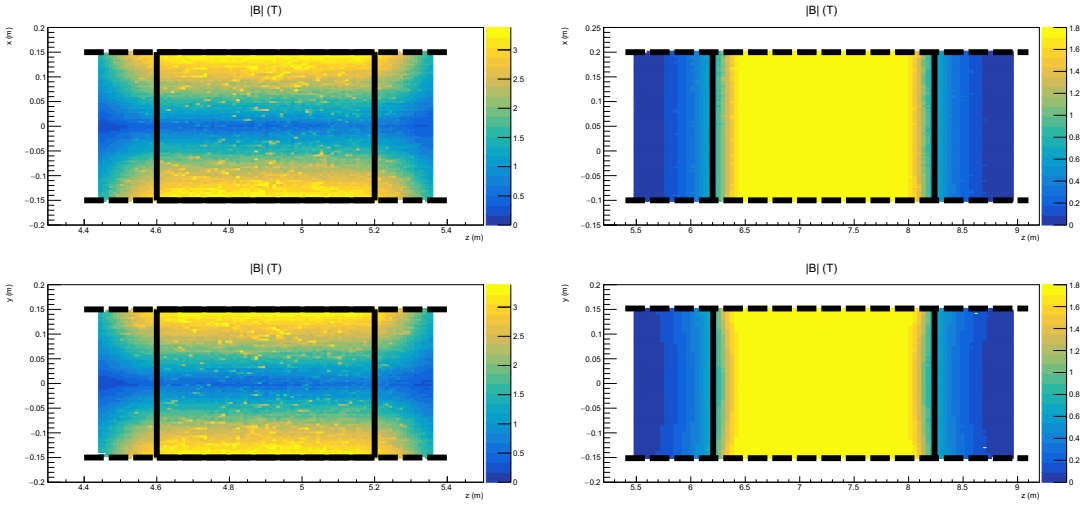

(a) Quadrupole (b) Dipole

Figure 2.24: The field extends outside of the magnet region (black lines), both for the quadrupole (left) and the dipole (right), with reduced intensity.

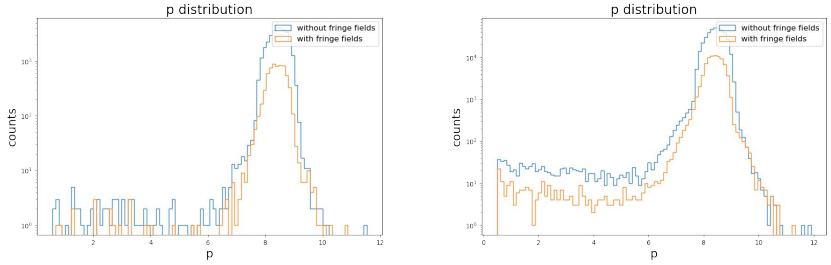

(a) K^+ (b) π^+

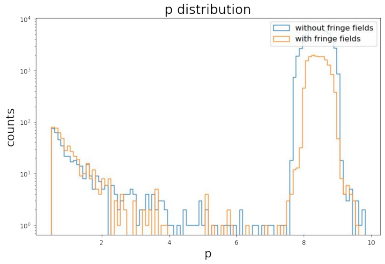

(c) e^+

Figure 2.25: Momentum of particles arriving at the tagger entrance, when the fringe fields are/are not applied (orange/blue).

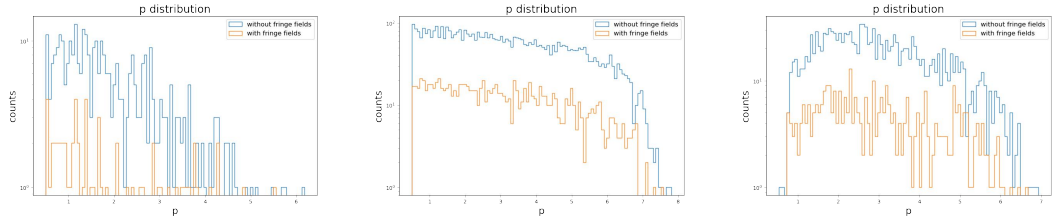

(a) e^+ momentum (b) μ^+ momentum (c) π^+ momentum

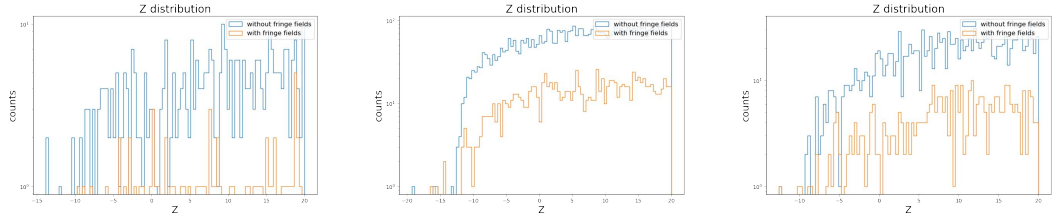

(d) e^+ z (e) μ^+ z (f) π^+ z

Figure 2.26: Momentum (top) and impact point on tagger (bottom) distributions for the signal particles hitting the tagger walls, when the fringe fields are/are not applied (orange/blue).

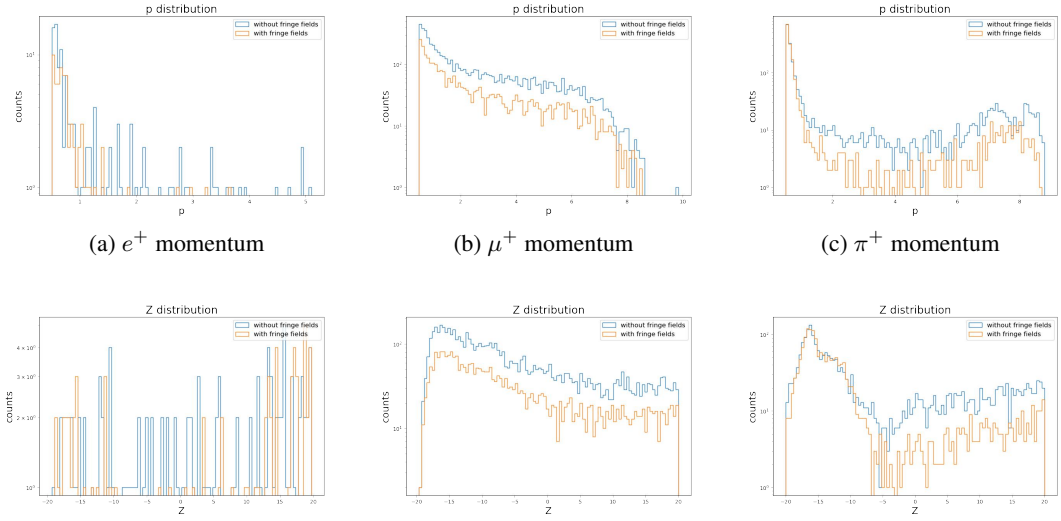

(a) e^+ momentum (b) μ^+ momentum (c) π^+ momentum

(d) e^+ z (e) μ^+ z (f) π^+ z

Figure 2.27: Momentum (top) and impact point on tagger (bottom) distributions for the background particles hitting the tagger walls, when the fringe fields are/are not applied (orange/blue).

2.3.2 Tracking Parameters

As mentioned above, it is possible to modify the field tracking parameters in order to achieve a specific level of precision when tracking particles through an electromagnetic field. GEANT4 divides the track's curved path into linear chord segments to compute the particle's motion in a field, selecting the chord segments to approximate the curved path within a preset tolerance. To better understand the underlying mechanism, it is useful to look at how GEANT4 propagates a particle, including all of its interactions with matter and physics processes (e.g. decays).

A physics step in GEANT4 determines the maximum step for applying physics processes. The user can select a maximum for this value, which is set by default at 100 mm. It is chosen then as the minimum of this defined value, the distance to the next volume boundary, and the smallest value that any ongoing physics process has determined (the process that requires the shortest length limits the step, as for instance, the decay time of a particular decay channel). One physics step can include more integration steps and so creates several chords.

The precision of the propagation of particles through the simulation may be adjusted using a number of parameters:

- δ_{Chord} for the precision of hitting a volume;
- $\delta_{Intersection}$ for boundary crossing;
- $\delta_{OneStep}$, ε_{min}, ε_{Max} for the integration accuracy.

The δ_{Chord} parameter is an upper bound for the sagitta, i.e. the maximum distance between the real trajectory of a particle and the chords that approximate it. GEANT4 must choose such

segments such that the sagitta is smaller than δ_{Chord} (Fig. 2.28a). Since this is the maximum error in the approximation of the curved path to the linear chords, it is related to the accuracy of intersecting a volume placed along the particle trajectory: it is the maximum distance by which the trajectory could cross the volume, but the chords would not.

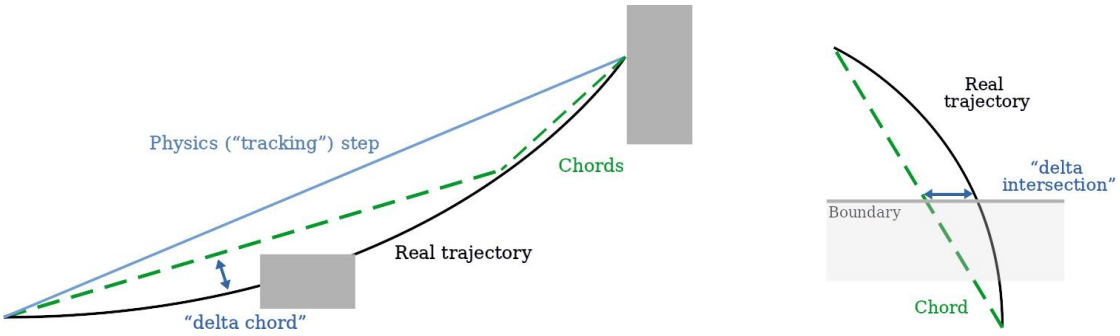

(a) "delta chord" (b) "delta intersection"

Figure 2.28: Due to the approximation of the curved trajectories by straight-line chord segments, the δ_{Chord} parameter is the maximum sagitta allowed (left), while $\delta_{Intersection}$ is the accuracy for the boundary intersections (right).

$\delta_{Intersection}$ is the maximum error allowed in the intersection of a track with the boundary of a volume (Fig. 2.28b). As a result, the number of boundary crossings is directly proportional to the precision of the position of the track after a certain number of them.

It is important to establish an acceptable level of accuracy when using integration to calculate the trajectories, this results in a compromise between acceptable errors and reasonable simulation times. The three parameters relevant for adjusting the integration accuracy are $\delta_{OneStep}$, ε_{min}, ε_{Max}. The size of an integration step must be limited so that the final position and momentum errors are small enough. ε is a relative tolerance: it is the limit on the estimated error of $\Delta p/p$ and $\Delta x/x$ for each integration step (p and x being the momentum and position). ε_{Max} is an upper limit for large steps, while ε_{min} is the minimum value. $\delta_{OneStep}$ is the maximum distance between the endpoint of an integration step that does not cross a volume and the curve endpoint.

A summary of the GEANT4 tracking parameters in a magnetic field is shown in Figure 2.29. So, GEANT4 internally splits a trajectory into chords that are chosen in such a way that:

- the chord's sagitta s is smaller than δ_{Chord};
- the error on the step endpoint is smaller than $\delta_{OneStep}$;
- the distance d between the intersection of the track with a volume boundary and the chord is smaller than $\delta_{Intersection}$.

These parameters are set by default by GEANT4 as in Table 2.1. $\delta_{Intersection}$ and $\delta_{OneStep}$ parameters are related since it is reasonable to have similar accuracies on the endpoint of integration steps and on the intersection with a volume edge. The GEANT4 User's Guide [78]

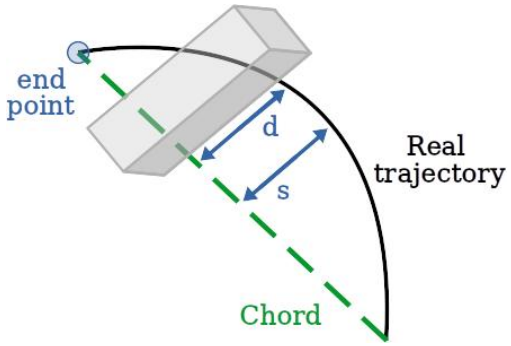

Figure 2.29: Summary of GEANT4 tracking parameters: $s < \delta_{Chord}$, $\Delta_{endpoint} < \delta_{OneStep}$ and $d < \delta_{Intersection}$.

Parameter	GEANT4 default	G4beamline default
δ_{Chord}	0.25 mm	3 mm
$\delta_{Intersection}$	0.01 mm	0.1 mm
$\delta_{OneStep}$	0.01 mm	0.01 mm
ε_{min}	$5 \cdot 10^{-5}$	$2.5 \cdot 10^{-7}$
ε_{Max}	0.01	0.05

Table 2.1: GEANT4 and G4beamline default tracking parameters.

recommends keeping these two parameters within one order of magnitude of each other. The most significant parameter of the two is $\delta_{Intersection}$ since the error limited by $\delta_{OneStep}$ is comparable to a statistical uncertainty, while $\delta_{Intersection}$ is correlated to a potential systematic error on the momentum reconstruction of tracks because the intersection point will always be on the inside of the real curved trajectory. Setting a too small δ_{Chord} in terms of CPU performance is quite expensive since it is proportional to the number of steps, while lowering $\delta_{Intersection}$ is less expensive since it is proportional to the number of crossed volume boundaries.

Table 2.1 also shows the G4beamline default values. The plots shown in Fig. 2.30 indicate that, looking at the momentum and angular distributions at the entrance of the tagger, there is no significant difference in tracking particles with the default parameters or with the G4beamline's default ones. G4beamline's values are appropriate for beamlines of typical sizes of a few tens of metres, such as the ENUBET transfer line. Since the particle budget at the decay tunnel has not changed, and the simulation time is advantageous with these values the GEANT4 simulation has been set up with the G4beamline default values.

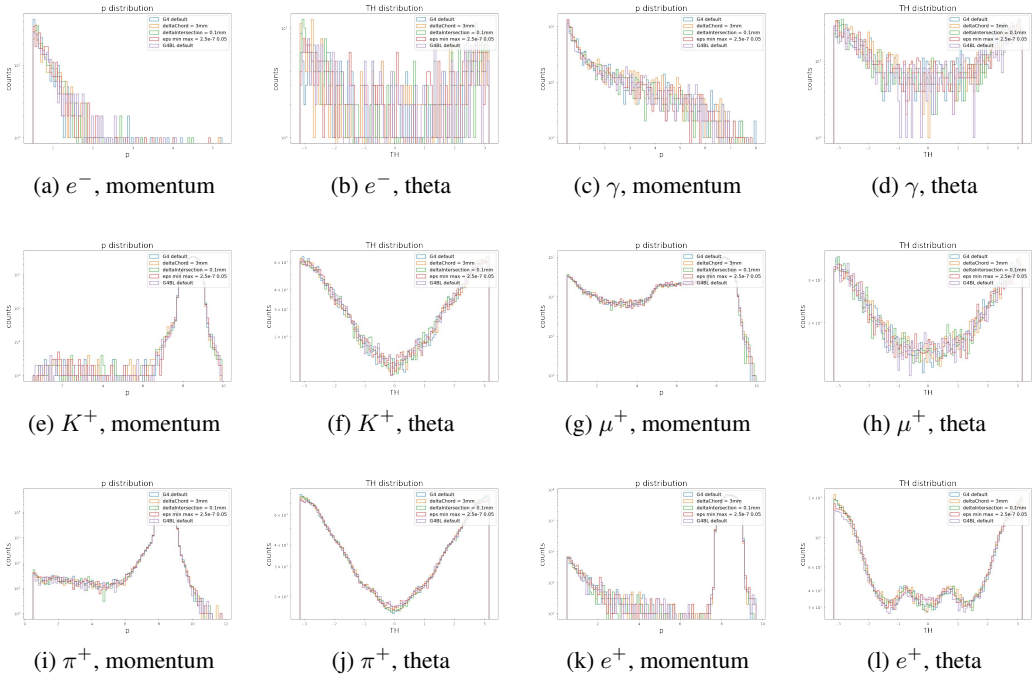

(a) e^-, momentum (b) e^-, theta (c) γ, momentum (d) γ, theta

(e) K^+, momentum (f) K^+, theta (g) μ^+, momentum (h) μ^+, theta

(i) π^+, momentum (j) π^+, theta (k) e^+, momentum (l) e^+, theta

Figure 2.30: Momemtum and angular distributions of particles at the tagger entrance level, for different values of the tracking parameters (100 MPOT).

2.4 Most recent beamline design and its optimization

A new beamline design, named TLR6_v2, that permits a large increase in the statistics has been reached after several dedicated studies on the target, optics, and collimation. It employs two dipoles as the previous design (two identical normal-conducting dipoles with a 1.8 T field for a 14.8°total bending with respect to the primary proton beam), and features an improved shielding to reduce contamination from electron neutrinos in the sub-GeV range coming from kaon decays in the target region. The optics has been optimized considering a 10% momentum bite. This configuration differs from the previous one in the number, location, field, and length of the quadrupoles, and also because a new and more efficient target has been designed by the collaboration [53]. The new target design has been reached by scanning different target geometries and materials so to maximize the kaon yield. The result is a Graphite rod with a 3 cm radius and a length of 70 cm. The new beamline shown in Fig. 2.31 contains the improved Graphite target (red) followed by a Tungsten foil (black) and a quadrupole triplet (grey) as a focusing system. Between the two dipoles (orange) there are now two focusing quadrupoles: all together making up the momentum selection section. An additional quadrupole is placed after the second dipole. All of the magnets have apertures of 15 cm. The collimators (blue) are made of Copper up to the second bending dipole, where there is one Inermet180 collimator (violet). The tagger (yellow) is 40 m long and is followed by the hadron dump (light grey). The proton

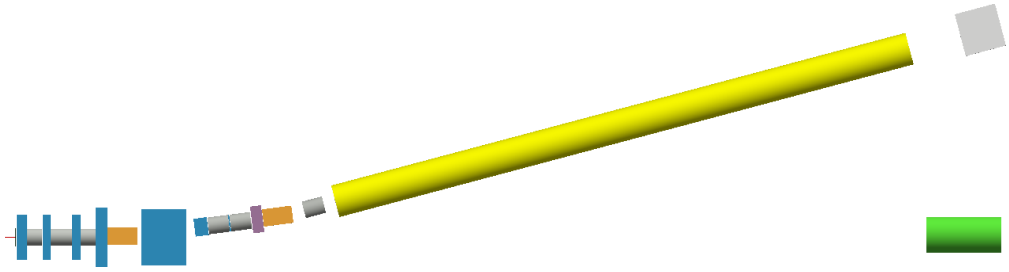

Figure 2.31: ENUBET beamline TLR6_v2 design.

dump (green) has the same layered design as the previous beamline described in Sec. 2.2.2. As in the previous version, this beamline has been enclosed by concrete for a more realistic shielding.

2.4.1 Optimization procedure

Given the complexity of the problem and the computational length to quantitatively evaluate the performance of a beamline candidate, a manual approach can easily become unfeasible when multiple variables are included. Exploiting the flexibility of the GEANT4 control card and the very detailed particle information that can be gathered from the developed code, it was very convenient to implement a systematic optimization method for the beamline. A generic optimization framework (the "optimizer") based on a genetic algorithm was developed based on the work done for optimizing the complex geometry of the magnetic horn [53, 63]. The optimizer is a standalone program that automatically launches GEANT4 simulations of different beamline configurations in the computing cluster, waits and analyzes the results, and decides which new configuration to launch, looping on these steps until convergence. The application of this optimization method has significantly improved the quality of the design of the ENUBET secondary beamline.

The use of a simple manual scan can be convenient when there are only one or two free parameters. If the optimization problem involves a large number N of variables, the number of configurations to be tested grows as the power of N. The use of a genetic algorithm allows searching for a global optimum across a large parameter space without being caught in local minima. The more parameters are present, the more time is needed to reach the convergence of the algorithm. A set of parameters (e.g. a beamline configuration) corresponds to a point in the N-dimensional parameter space and is called an "individual". The set of possible configurations tested in parallel is the "population". Once the free parameters of the problem are chosen, the basic working principle of the algorithm is the following:

- the initial population is randomly generated with parameters within a predefined range;
- the simulation runs in these configurations;
- the Figure Of Merit (FOM), which is a function of the simulation output that describes the success of the optimization, is evaluated;

- a set of best candidates is selected, according to the value of the FOM, they are called "elite" configurations and are kept for the next iteration;
- a new population is generated, based on the parameters of the elites.

The procedure is iterated until an established maximum number of generations is produced, or when a satisfactory Figure Of Merit is reached.

The use of a batching system is particularly advantageous since several points in the parameter space can be simulated in parallel at every iteration. In this fashion, the length of a single job gives the length of one iteration of the optimizer. When the submitted jobs are time-consuming, in order to reach a better performance the optimizer allows to split the single configuration into parallel jobs, at the expense of having more jobs running and risking higher waiting times.

The optimizer employs a custom genetic algorithm implemented by the collaboration. After the first population is generated, it iterates over the following steps: launch of GEANT4 jobs, wait for all jobs to finish, run of the FOM computing code, run of the genetic algorithm to compute the next population, log of the results in a database.

2.4.2 Collimator optimization

The optics of this beamline version has been finalized but the design of the collimators of the second part of the transfer line still has to be completed (Fig 2.32). These collimators are essential in the ENUBET beamline since without them the background on the tagger walls could reach problematic levels. One possibility is to design a collimator right before the tunnel entrance, in a similar fashion as the previous beamline: an Inermet180 box with a conical aperture.

(a) Old beamline (b) New beamline

Figure 2.32: The collimators at the end of the previous transfer line (left) and the available space for inserting additional collimators in the new beamline version (right).

The first step in the design of this new object to be inserted in the transfer line is the choice of the degrees of freedom. For this shape, there are 5 free parameters: the dimensions of the box and the two radii of the inner conical opening, with the constraint of having the aperture smaller than the transverse dimensions. The position is fixed at the center of the gap between the last quadrupole and the tagger entrance, in order to exploit as much length as possible (about 70 cm). One must also choose an appropriate Figure of Merit, taking into account that a reduced statistic will be available since the simulation time is limited by the requirement of reaching the convergence of the algorithm in a reasonable amount of time (of the order of a couple of weeks). A reasonable choice for this specific problem is to consider a function that describes the signal-to-noise ratio at the tagger level. The goal of this study is indeed to maximize the S/N

ratio and a good statistics can be achieved by considering as signal the kaons that arrive at the tunnel entrance and as background the particles (electrons, positrons and charged pions) that hit the tunnel walls and do not come from kaon decays inside the decay volume. The expression of the FOM is the following:

$$\mathrm{FOM} = \frac{(e^+ + e^+ + \pi^+ + \pi^-)_{tagger\ walls\ bkg}}{K^+_{tagger\ entrance}} \tag{2.3}$$

where this expression will be minimized, and having the signal at the denominator is avoids the risk of reaching a zero background and so an undefined FOM.

The optimizer has been set up considering the total running time of the optimization process and the amount of statistics needed for the FOM computation. On the GE batch-queuing systems up to 3000 jobs can be launched by a single user in parallel. In order to get a 500 kPOT statistics per beamline configuration, the single configuration is split into 30 parallel jobs, each of them running over 1/6 of a target file (100 kPOT) so that the total simulation time per configuration decreases from 9 to about 2 hours with a 500 MeV momentum cut. The resulting number of configurations per iteration is 90: the first iteration has a population of 100 and the number of elites is set to 10. The convergence is expected in $\mathcal{O}(100)$ iterations.

Figure 2.33 shows the optimization results after 100 iterations. The first plot (2.33a) shows the evolution of the average figure of merit of the elites for each iteration and can be used as a convergence indicator. In Fig. 2.34 the evolution of some of the parameters is shown. The value of each parameter becomes stable towards the end of the optimization process, while for the first iterations it is quite variable since the algorithm is scanning the entire parameter space and finds better and better configurations. The best candidate is illustrated in Fig. 2.33b. The transverse dimensions are similar to the collimator of the previous beamline, while the length is necessarily shorter. The optimizer went in the direction of increasing the apertures of the collimator. The values found are at the upper limit of the allowed range. This can be seen also in Figure 2.35 which shows the distributions of the values of the radii at a given iteration. As the optimization proceeds, the values go from an almost flat distribution across the range to a distribution peaked at the higher edge.

This can be seen also in Fig. 2.36, which contains the scatter plots of the optimization variables with the FOM in colour scale. The highest values of the Figure Of Merit can either be concentrated at specific values of the parameters, or they can be spread in the space. The values of the cone radii significantly influence the FOM, while this is not the case for the box dimensions. More in detail, the scatter plots of the FOM versus the optimized parameters shown in Fig. 2.37 confirm that the minimum FOM can be reached for a wide range of the collimator dimensions, while this is not the case for the collimator radii.

The highest value of the Figure Of Merit is $\mathrm{FOM} = -1.3$. It is still lower than the nominal beamline's value, which is -0.64, however, this was expected since the nominal beamline without any collimators at the end of the transfer line is not realistic, as the beam halo and background particles diverging from the beamline would not be under control, nor if some misfocusing would have to happen. The results in terms of background reduction and signal enhancement are shown in Fig. 2.38. Fig. 2.38a to 2.38d show the signal distributions at the tagger entrance: positive pions and kaons momentum and angular distributions are nearly unaffected by the op-

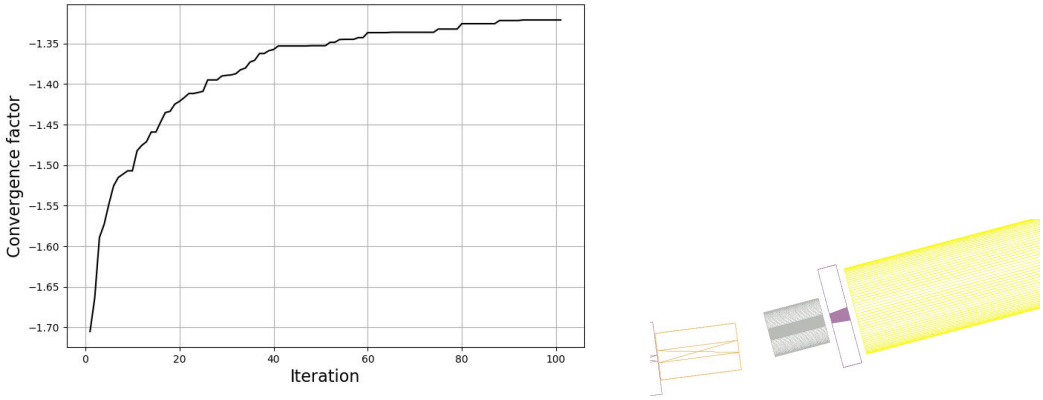

(a) Evolution of the average of the figure of merits of the best 10 configurations.

(b) Optimized collimator.

Figure 2.33: First optimization results.

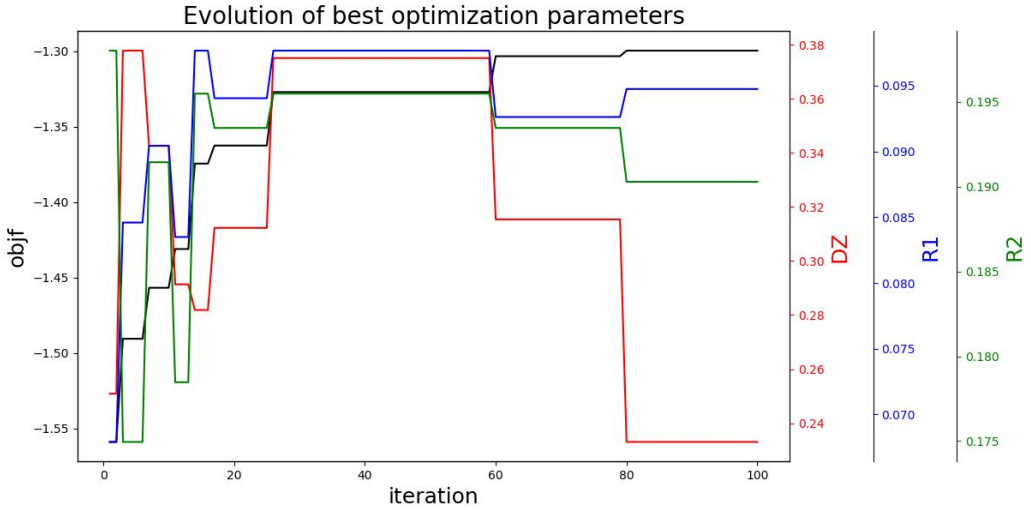

Figure 2.34: Evolution of the most significant parameters of the best configuration for every iteration, where “objf” is the FOM. In particular, DZ is the half-length of the collimator and R1, R2 are the radii of the cone, in meters.

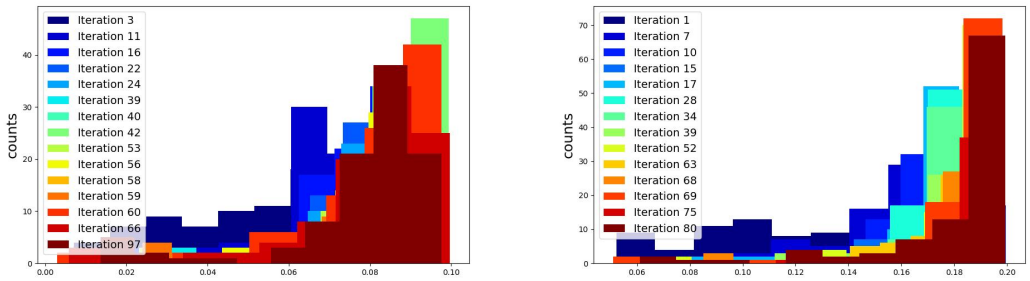

(a) R1 (b) R2

Figure 2.35: Distributions of the cone radii of the population at a given iteration.

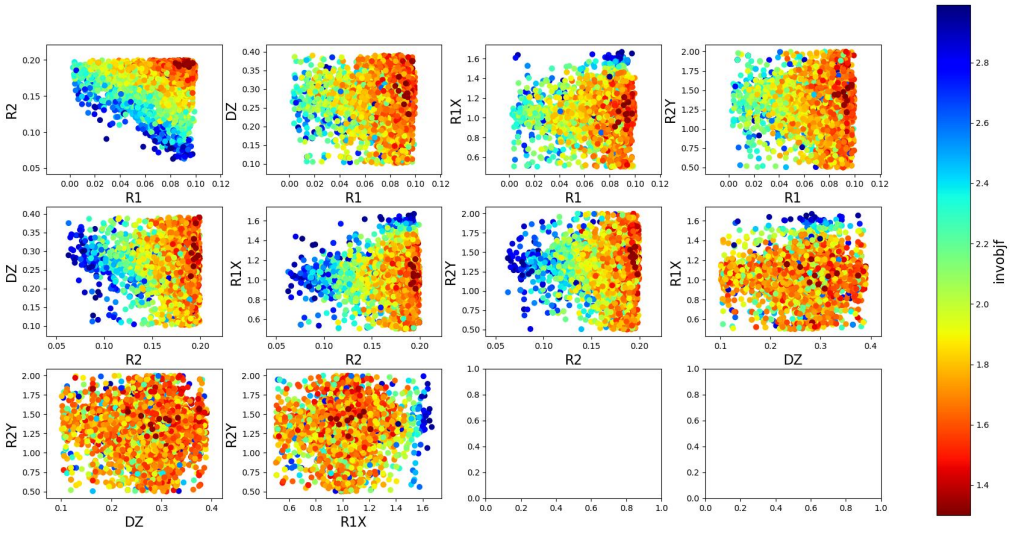

Figure 2.36: Two dimensional scatter plots of the optimization variables. The colour scale corresponds to the inverse FOM value (so that red corresponds to the smaller value of the FOM, which means a maximized S/N ratio, as in Eq. 2.3).

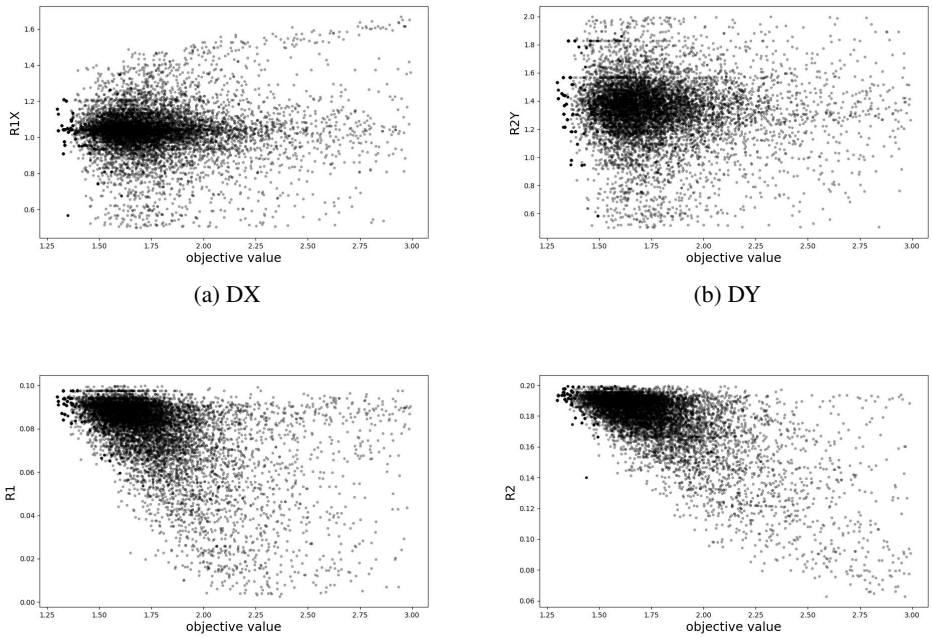

(a) DX (b) DY

(c) DX (d) DY

Figure 2.37: Scatter plots of FOM versus the transverse dimensions parameters (top), and FOM versus the aperture radii (bottom).

timization procedure. Looking at the signal distributions of pions, positrons and muons on the tagger walls (Fig. 2.38e to 2.38g) one can notice again that they have similar shapes. The backgrounds (Fig. 2.38h to 2.38j) seem to be slightly reduced, except for the low energy pions. Most of them (Fig. 2.39) are produced by the collimator itself, meaning that the collimator is too short and acts as a second target, producing more particles than it absorbs.

A second optimization was then configured with a change in the code that allows placing a longer collimator, moving forward the tagger and the hadron dump accordingly, at the expense of the transfer line length. The gap between the last quadrupole and the tagger entrance is about 70 cm in the initial version of the beamline, while in the previous beamline the collimator was 2.6 m long. The range of the length parameter is set so that the optimized collimator can be between 1 and 4 m long. Furthermore, a new Inermet180 collimator is placed between the second dipole and the last quadrupole, as in the last beamline version. In order to keep a reasonable number of parameters, the transverse dimensions of the first collimator were fixed from the previous beamline (it has been proven from the previous results that they were not influential parameters, see e.g. Fig 2.36 and 2.37), while the ones of the last collimator were fixed from the previous optimization result. The total number of parameters is, therefore, 5: the apertures in x and y of the first collimator, the length of the last collimator and its 2 cone radii.

The setup is similar to the first optimization: an initial population of 100 individuals, with

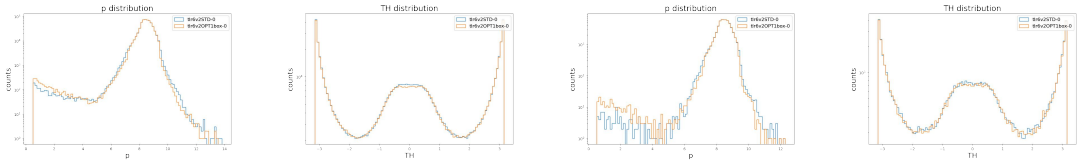

(a) $p_{\pi+}$ at tagger entrance (b) $\theta_{\pi+}$ at tagger entrance (c) p_{K+} at tagger entrance (d) θ_{K+} at tagger entrance

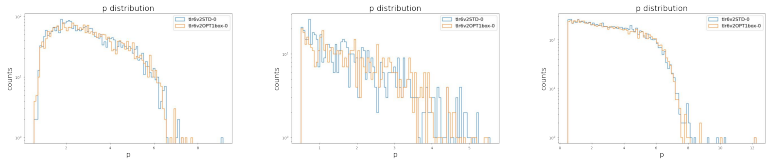

(e) signal $p_{\pi+}$ on tagger walls (f) signal p_{e+} on tagger walls (g) signal $p_{\mu+}$ on tagger walls

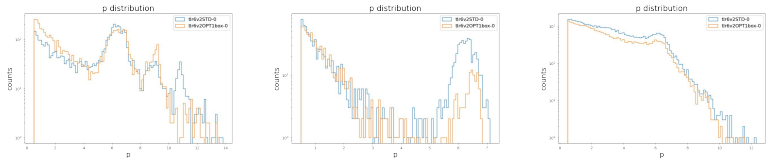

(h) background $p_{\pi+}$ on tagger walls (i) background p_{e+} on tagger walls (j) background $p_{\mu+}$ on tagger walls

Figure 2.38: Distributions of signal and background for the nominal (blue) and optimized (orange) beamline.

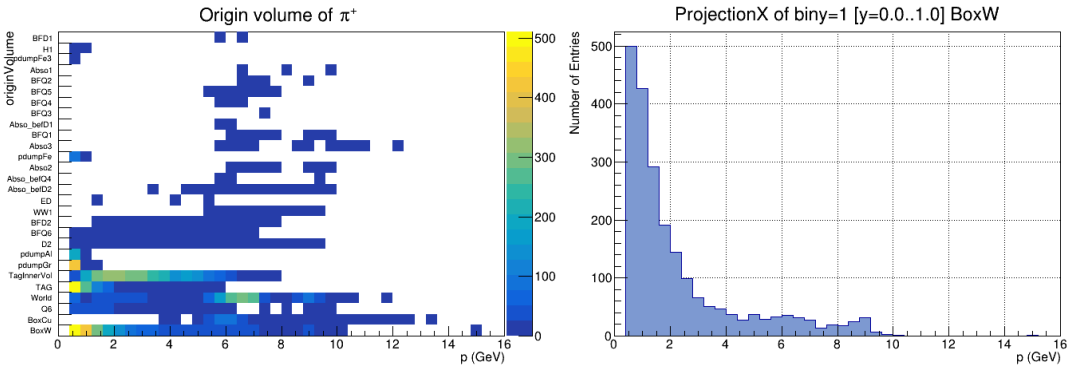

(a) Origin volume of π^+ at different momenta. (b) Momentum distribution of π^+ coming from the collimator.

Figure 2.39: Origin of background pions on tagger walls.

10 elites. The 100 iterations of the previous case were obtained in 19 days since the estimated running time was slowed down by the job's queue time: out of the 3000 parallel jobs, only 2000 of them could run simultaneously. The issue can be avoided by processing 1/4 of each target file, and grouping them by 20, for the same total of 500 kPOT. The estimated time per iteration considering a 500 MeV momentum cut is about 3 h.

The following Table 2.2 and Figures 2.40, 2.41 , 2.42 show the optimization results after 100 iterations.

Parameter	Old beamline	New beamline
Collimator 1		
x aperture	41 mm	53 mm
y aperture	35 mm	37 mm
Collimator 2		
Width	3 m	2.5 m
Height	3.5 m	3.44 m
Length	2.5 m	2.15 m
Entry radius	4.5 cm	8.8 cm
Exit radius	8 cm	11.8 cm

Table 2.2: Old collimator parameters and new optimized ones.

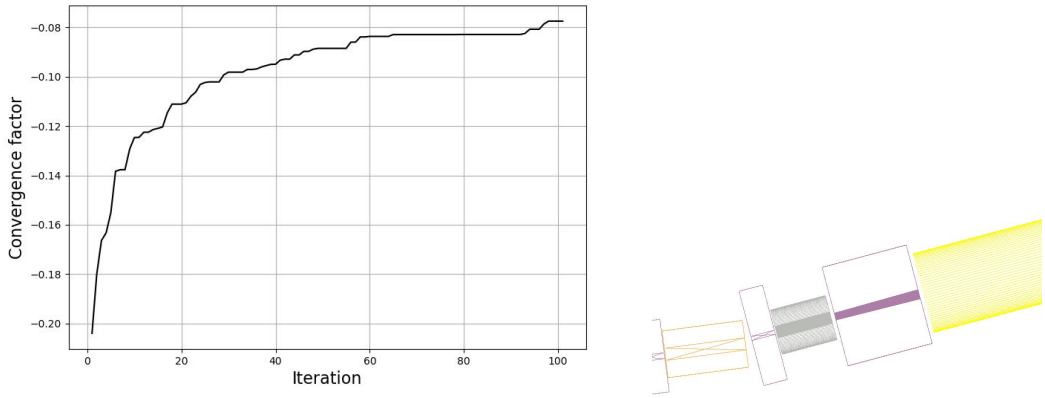

(a) Convergence indicator

(b) Optimized collimators

Figure 2.40: Collimators optimization results.

A full simulation (1 GPOT) run with the two optimized collimators shows that the positron signal is good (Fig. 2.43a and 2.43b) and there is a background reduction at the tagger level (Fig. 2.43c to 2.43h are the distributions of momentum and longitudinal impact point on the tagger) with respect to the nominal bare beamline (TLR6_v2). However, the signal and background positron distributions are very similar. Background positrons (Fig. 2.43h) are shifted towards the

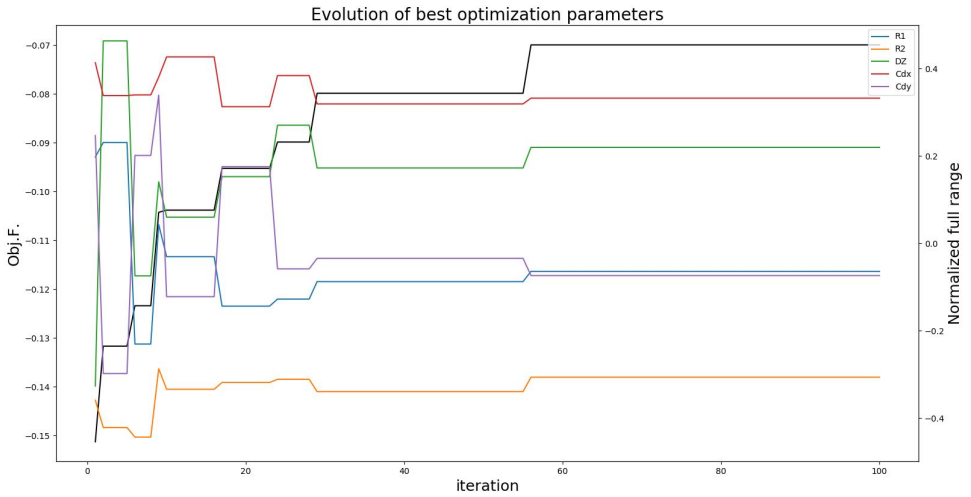

Figure 2.41: Evolution of the best parameters, in a normalized range.

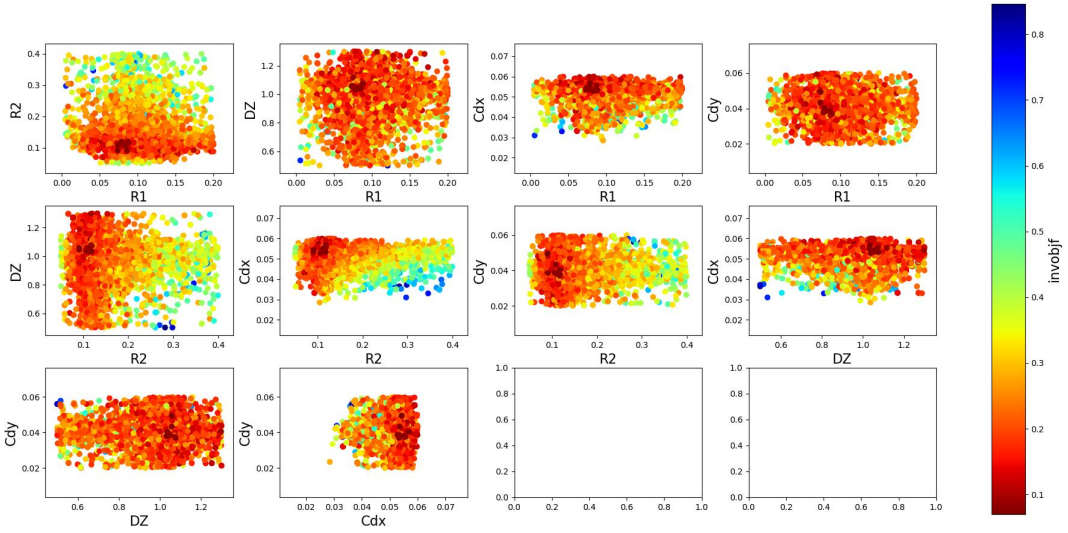

Figure 2.42: Two dimensional scatter plots of the optimization variables with the FOM in colour scale.

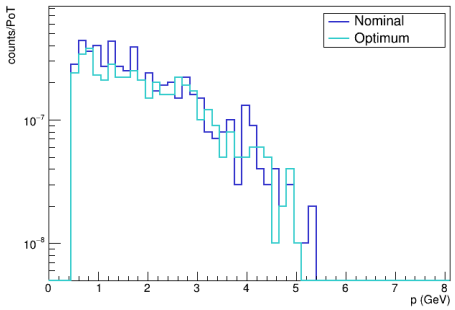

(a) e^+ signal, momentum

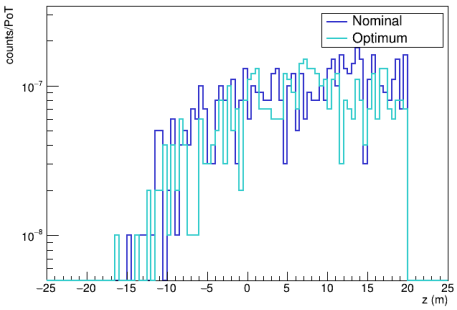

(b) e^+ signal, impact point

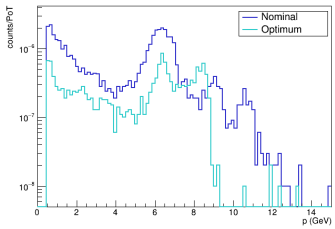

(c) π^+ background, momentum

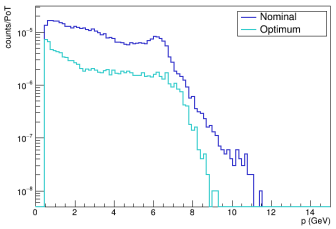

(d) μ^+ background, momentum

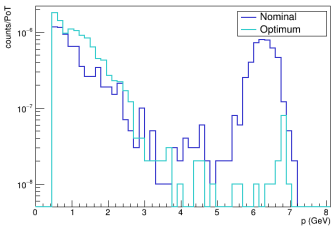

(e) e^+ background, momentum

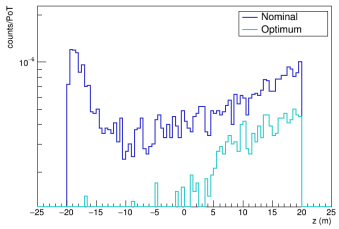

(f) π^+ background, impact point

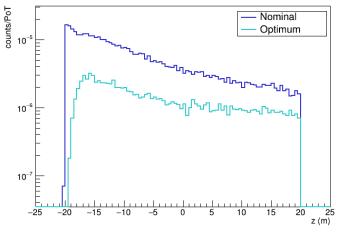

(g) μ^+ background, impact point

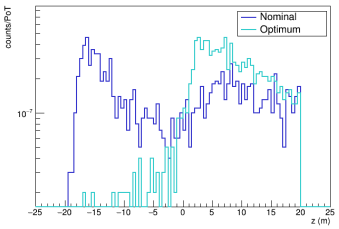

(h) e^+ background, impact point

Figure 2.43: Distributions of momentum and impact point on tagger (in tagger coordinates, where the origin is at its center) for signal positrons and background particles, in the nominal (blue) and optimized (light blue) versions of the beamline.

second half of the tunnel where they are nearly indistinguishable from the signal (Fig. 2.43b). Additionally, their energy distribution is comparable to that of K_{e3} positrons (Fig. 2.43a and 2.43e). The resulting performance of this beamline, which will be referred to as TLR6_v3 (in terms of tagger efficiency and S/N, as described in Sec. 1.5.4), is only moderately improved with respect to the TLR6_v2. This is due to the fact that the FOM used to improve the S/N ratio only considers the inclusive number of hitting particles and ignores their distribution along the tunnel.

A possible solution would be to implement a FOM taking into account the shape of the positron distribution at the tagger level in the momentum-impact point plane. This approach, although more fine-tuned for a better optimal solution, is significantly time-consuming from a computational point of view, since it requires more statistics to analyse a two-dimensional distribution, compared with the current FOM that integrates all countings (already a 1D distribution could reach computationally prohibitive times). Nevertheless, an attempt to enhance the signal and background particles is needed (more details in Sec. 2.4.3).

Investigating the positron origin in this beamline configuration (with the two Inermet180 collimators at the end of the transfer line) it emerges (Fig. 2.44) that most of the positrons are produced by gamma conversion: not only from the Tungsten foil (as expected) but most of them are generated by the second to last collimator.

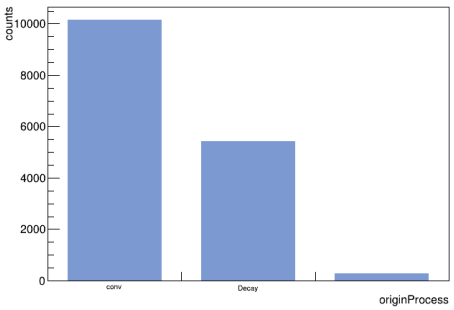

(a) Positron origin process.

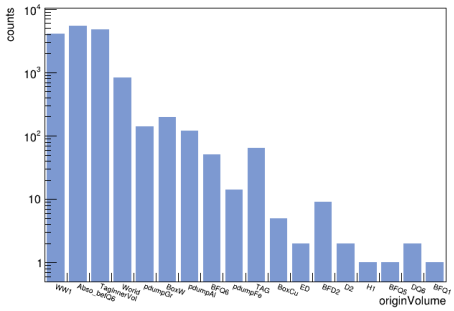

(b) Positron origin volume.

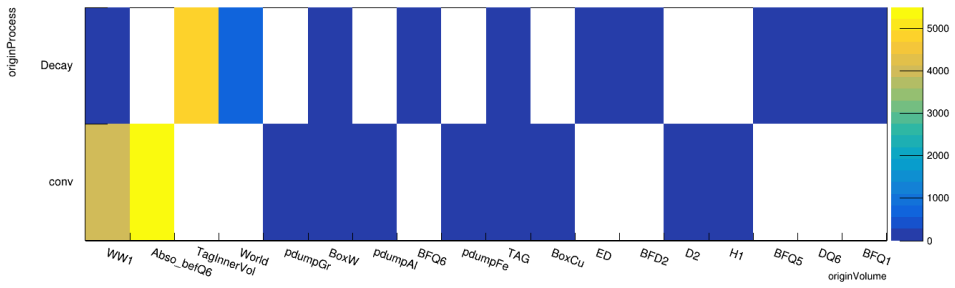

(c) Scatter plot of origin process and volume

Figure 2.44: Origin of positrons at tagger level classified by physics process and volume where it occurred.

Despite the presence of the second to last collimator, the total number of positrons (in Fig. 2.43e) is similar with respect to the nominal beamline, meaning that the last collimator is used for suppression. Because of the parameters' bounds set in the optimization process, not having this collimator within the magnet aperture was not possible. The first option is to temporarily remove this collimator from the beamline, called TLR6_v4, while a better way would be to run a new optimization procedure with improved boundaries on the apertures of this collimator (as done in Sec. 2.4.3). The new positron distributions obtained with the TLR6_v4 are shown in Fig. 2.45.

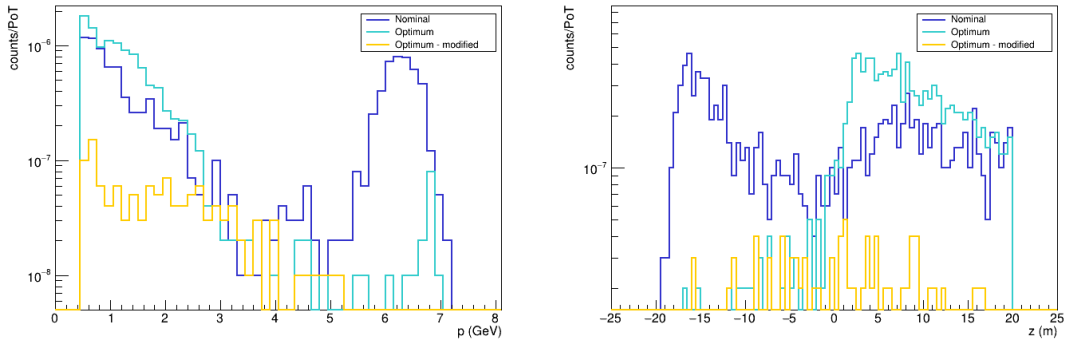

(a) Momentum

(b) impact point

Figure 2.45: Distributions of momentum and impact point on tagger for background positrons, in the nominal (blue), optimized (light blue) and modified without the second to last collimator (orange) versions of the beamline.

After the satisfactory results shown in Fig. 2.45, some manual fine-tuning has been performed so to have an additional verification of having reached an optimal beamline configuration, and eventually to slightly improve it if possible. A first attempt was to change the collimator material: the results shown in Fig. 2.46 imply that the current Inermet180 case is already a better choice than Copper and Iron for the amount of background at the tagger, while, as expected from the previous studies (Sec. 2.2.3), Tungsten gives very similar results.

A second attempt was to modify the Tungsten foil thickness (i.e. the length in z of the positron filter placed downstream of the target). The foil thickness used so far by the TLR6 beamlines is 10 mm (it was 5 cm in the TLR5_v5): a scan of different foil thicknesses from 5 mm to 5 cm showed that it would be possible to further improve the S/N but inevitably losing some flux. Also, the no-foil option has been tested. Despite the fact that the particle flux is sensibly higher, the signal-to-noise ratio gets substantially worse (see e.g. Sec. 2.2.3), thus the final choice in the beamline design is to keep the 10 mm foil at the beginning of the transfer line.

2.4.3 Latest optimization results with a boosted statistics approach

A new procedure in the optimization process, that increases the available statistics on the FOM computation by a factor of $\sim$ 10 has been developed and tested. The code upgrade consists in

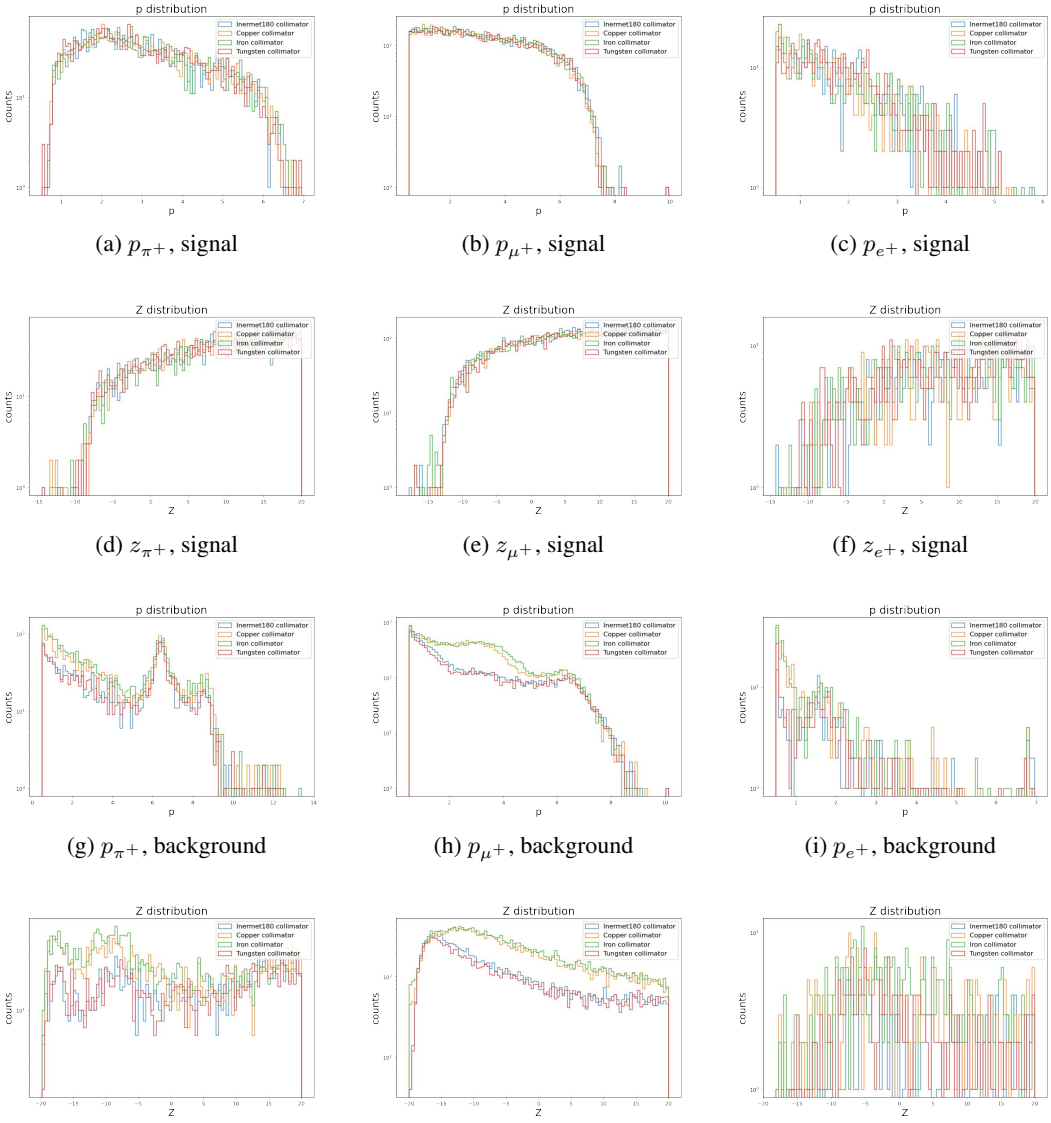

(a) $p_{\pi+}$, signal (b) $p_{\mu+}$, signal (c) p_{e+}, signal

(d) $z_{\pi+}$, signal (e) $z_{\mu+}$, signal (f) z_{e+}, signal

(g) $p_{\pi+}$, background (h) $p_{\mu+}$, background (i) p_{e+}, background

(j) $z_{\pi+}$, background (k) $z_{\mu+}$, background (l) z_{e+}, background

Figure 2.46: Distributions of signal and background on tagger walls for different collimator materials: Inermet180 (default, blue), Copper (orange), Iron (green) and Tungsten (red).

dividing the beamline simulation into two separate simulations, one for the determination of the signal and one for the background (which are the ingredients of the Figure of Merit). This is needed because different approximations have been used for the two cases, in order to maximize the statistics of each sample without losing accuracy. The boosting is performed in the following way:

- Signal: when kaons reach the tunnel entrance, K_{e3} branching ratio is set to 100% and the positron signal hits on the tagger walls are recorded: this increases the statistics of signal positrons by about a factor 20, while giving also access to all their distributions and keeping the same simulation time;

- Background: the positron contribution can be increased by means of a dedicated simulation which only includes e^+, e^-, γ, plus an energy cut in the target particles. This leads to an increase of a factor $\lesssim 10$ in the statistics, for the same simulation time, while keeping the distributions close to the nominal ones. Unfortunately, an analogous trick cannot be done for the pions, due to the complicated nature of hadronic showers, so they have been excluded from the FOM (in any case, they can be discriminated to a good level by the detector).

The choice of the number of parallel jobs to be submitted to the computing cluster has been chosen in order to match the statistics of the signal and background simulation, and also in order to ensure a reasonable time ($\lesssim 10$ h) for a single iteration. The result was 200 jobs for the signal sample, and 500 for the background, each one about 8 h duration, for an order of ~ 100 counts per iteration.

A new optimization with a reduced number of beamlines per iteration (20, 4 elites), resulting in 1200 jobs per iteration, was set up. Both collimators were inserted in the beamline, as in the TLR6_v3 version, allowing the algorithm to scan a broader range of the aperture parameters. The results reached are comparable to the TLR6_v4, and the increased statistics both confirmed the accuracy of the earlier studies and provided two final collimators.

2.5 Results

The GEANT4 code has been significantly upgraded over the past years. From the initial and most simple output configuration, which contained histograms of the relevant quantities recorded at the virtual detectors (e.g. the one at the tagger entrance and the tagger itself), the output file now contains 3 tree structures for three different levels: the tagger entrance (particles crossing a virtual detector placed at the tunnel entrance), the tagger walls (particles hitting the tagger cylinder) and the neutrino detector (a 6×6 m^2 virtual detector placed at about 60 meters from the end of the decay tunnel). This structure can be in principle implemented for any other relevant beamline element or area, at the expense of the output file dimensions. The saved data contain: particle PDG code, hit point coordinates, current momentum, PDG code of the parent and its momentum, type of generating process with the list of secondaries produced, and the origin volume name. This upgrade allows gathering useful information on the beamline.

All the information can be exploited in different ways, in order to debug the code or to better understand the properties of the beam, as seen in the previous studies. However, the useful plots that characterize the beamline are typically the spectra of particles at the tagger entrance, and the momentum and position distribution of particles along the tunnel walls. The following distributions are related to the last beamline version, the TLR6_v4, which is the current reference ENUBET beamline.

At the tunnel entrance (distributions plotted in Fig. 2.47) the rates obtained for a momentum of 8.5±5% GeV are 3.97×10^{-3} π^+/POT and 3.61×10^{-4} K^+/POT.

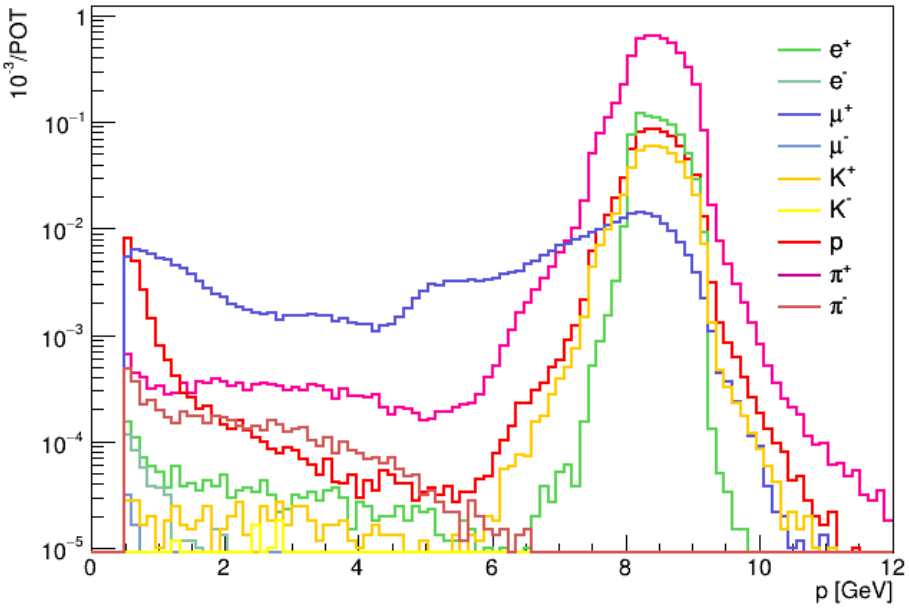

Figure 2.47: Particle budget at the decay tunnel entrance.

On the tagger walls, it is possible to discriminate between the signal and the background particles, by selecting the particles that originated inside the decay tunnel by decays of pions or kaons and hitting its walls. Figure 2.48 shows the momentum and longitudinal impact point (in tagger coordinates) of particles hitting the walls. The products of kaons transported by the transfer line that decay inside the tagger are considered signals. The main background consists of the off-momentum beam halo transported at the entrance of the tunnel.

The neutrinos that cross the virtual neutrino detector mentioned above are plotted in Fig. 2.49. There is a high contribution of neutrinos in the low energy range of the spectra, however, most of them are not originated inside the tagger. Figure. 2.50 shows only the neutrinos that are potentially tagged in the decay tunnel, and, thanks to the GEANT4 data structure, the different contributions of the various possible decay modes. Figure 2.51 shows where all the electron neutrinos arriving at the detector originated. Neutrinos produced inside the tagger have a spectrum peaked at ~ 4 GeV. The contributions from the decay along the beamline cover mostly the low-energy part of the spectra, most of them are produced by the absorbers in the first part of the transfer line and there is also a relevant contribution from the concrete shielding that surrounds the facility. While the low energy contribution could be easily dismissed by applying energy cuts, there are some neutrinos coming from early kaon decays that cannot be eliminated, however, it is a small contribution that can be corrected in the ENUBET implementation by relying on these simulations.

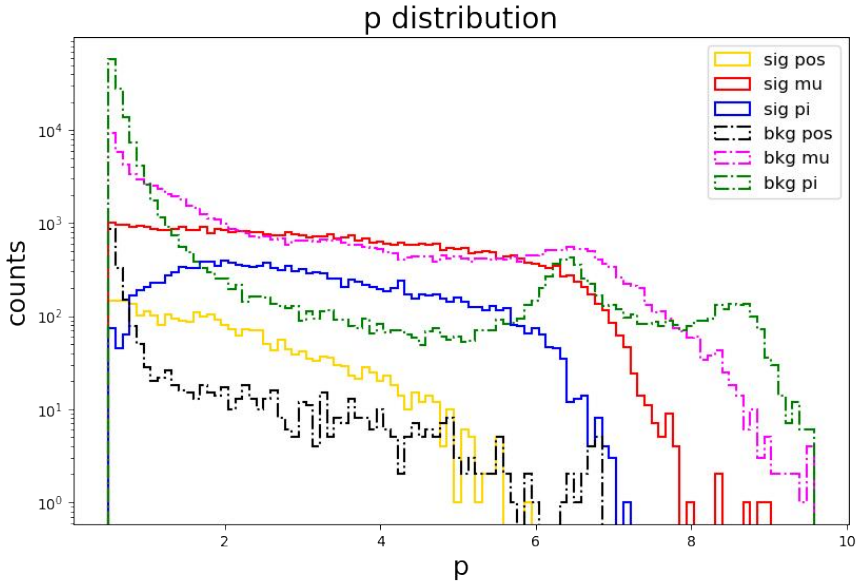

(a) Momentum

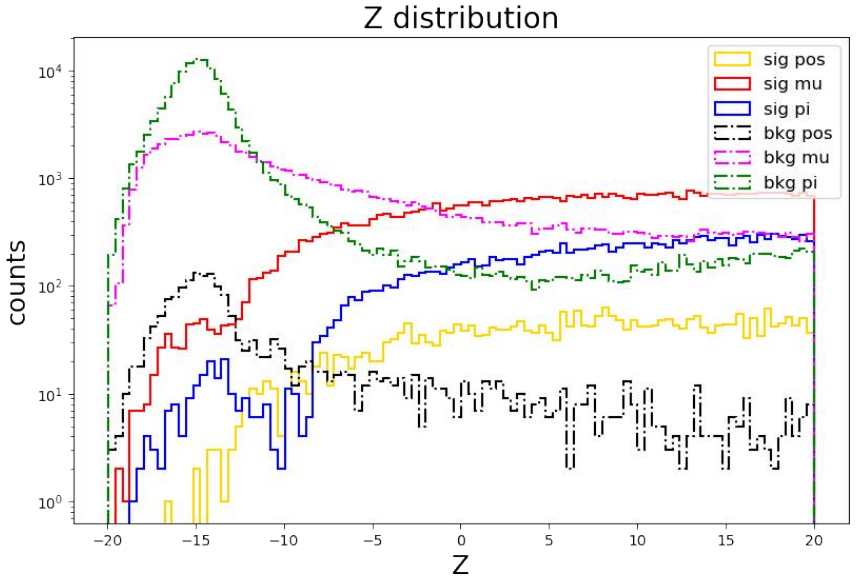

(b) Impact point

Figure 2.48: Momentum p (a) and impact point z (b) of particles hitting the tagger walls.

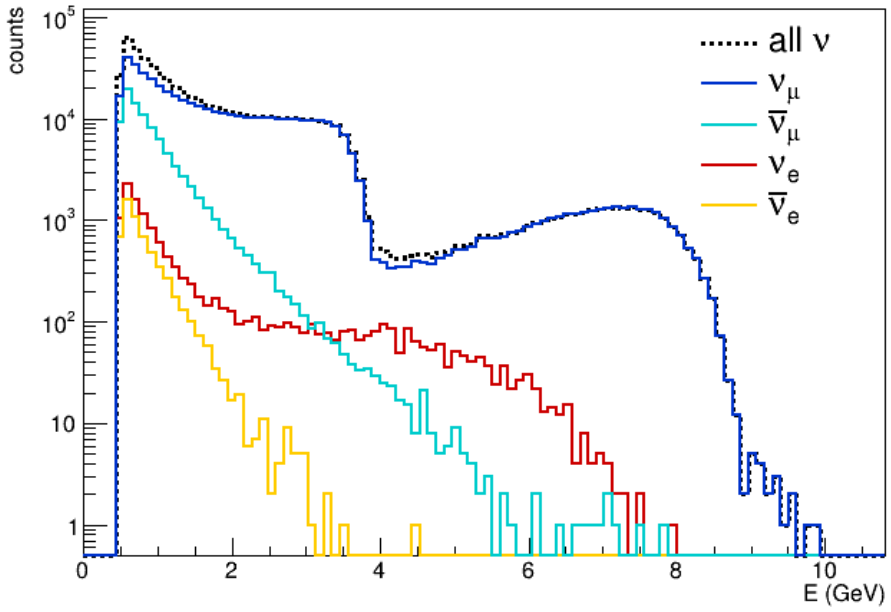

Figure 2.49: All the neutrinos arriving at the neutrino detector, divided by flavour.

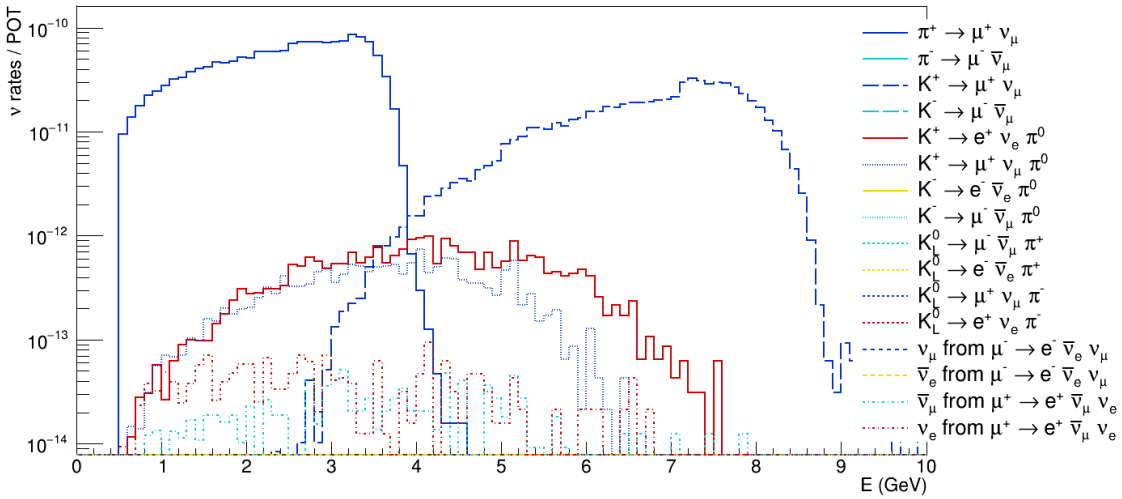

Figure 2.50: Rates at the neutrino detector for neutrinos produced inside the decay tunnel, breakdown by decay mode, scaled by the cross-section.

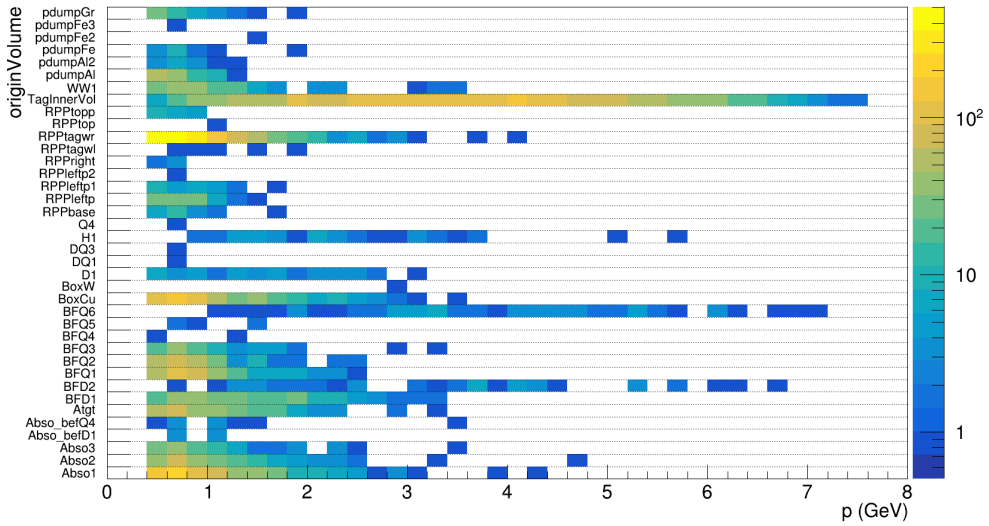

Figure 2.51: Origin of the electron neutrino along the beamline, counts in colour scale.

A summary of the results achieved with the various beamlines tested is in Table 2.3.

Beamline version	K^+ flux (10^{-4}/POT)	π^+ flux (10^{-3}/POT)	ν_e from K over total ν_e	ν_μ from K over total ν_μ	ν_μ from π over total ν_μ	Years for 10^4 ν_e^{CC}[2]
TLR5_v5	2.58	3.16	0.91	0.11	0.89	3.5
TLR6_v2	2.35	2.52	0.90	0.14	0.86	3
TLR6_v3	3.54	3.85	0.90	0.12	0.88	2
TLR6_v4	3.61	3.97	0.90	0.12	0.88	2

Table 2.3: Comparison of performances of the different beamlines studied. Neutrino percentual numbers take into account only neutrinos produced inside the decay tunnel, in terms of fluxes.

2.5.1 Cuts and simulation time

Three different cuts have been implemented in the GEANT4 simulation at three different levels: according to the momentum of the particle, the charge of the particle or the type of particle (with the possibility of keeping or killing the selected particles). All these cuts can be set from the control card. They are available at the Primary Generator Action level, which means directly for the particles coming from the target files, during the Stepping Action and at the level of the output tree storage. The three sets of cuts are completely independent one from the other.

The implementation of the momentum cut in the simulation was driven by the need of reducing the simulation running time since most of the CPU time is consumed by the handling

[2] Assuming 4.5×10^{19} POT/y and a, 500 t, 6×6 m^2 LAr detector 50 m away.

of low-energy particles. The total time required for processing 100 kPOT, which corresponds to a single input target file, is about 160 hours with the Grid Engine batching system. This is prohibitive because of the total statistic available (1 GPOT), the number of possible parallel jobs (2000) and the total given running time on the cluster (24 hours per job). Applying a momentum cut at the target and Stepping Action levels the time consumed improves considerably, reaching 30 hours for a 100 MeV cut and around 8 for 500 MeV (see Fig. 2.52). The choice of running all GEANT4 simulations of the beamline applying a 500 MeV cut is a compromise between the need for a speed-up and the physics results that can be obtained from the simulation. Particles below 500 MeV are not reconstructed by the ENUBET Event Builder. However,

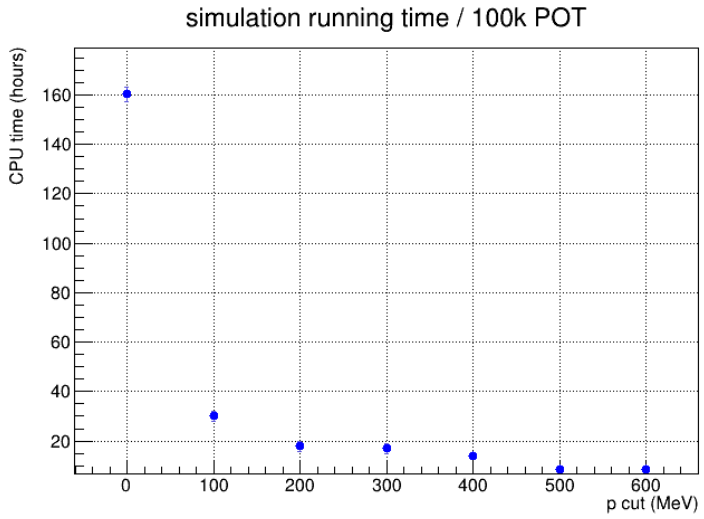

Figure 2.52: Simulation running time for 100 kPOT for different momentum cuts.

they could still contribute to the rate on the tagger walls and in worsening the performance of the positron identification. The plan for the future is to run a new simulation including particles below 500 MeV once the beamline design is definitively finalized, in order to understand if some further adjustments are needed.

2.5.2 Validation of the results

The validation of these results has been done by comparing the spectra of particles at the tagger entrance obtained with the ones obtained using the G4beamline simulation. In general, it is not always clear how to compare the results of two simulations. One must consider that there may be small discrepancies in the geometry (which are not easily identified in a simulation as complex as the ENUBET facility), differences in the cuts applied, or in the physics that is being simulated (even if G4beamline is a software based on GEANT4). Figure 2.53 shows the momentum distributions of some of the particles transported by the ENUBET transfer line. The agreement between the two simulations is good. This is important because the developed GEANT4 simulation allows a significantly increased flexibility and control over many beamline and particle quantities.

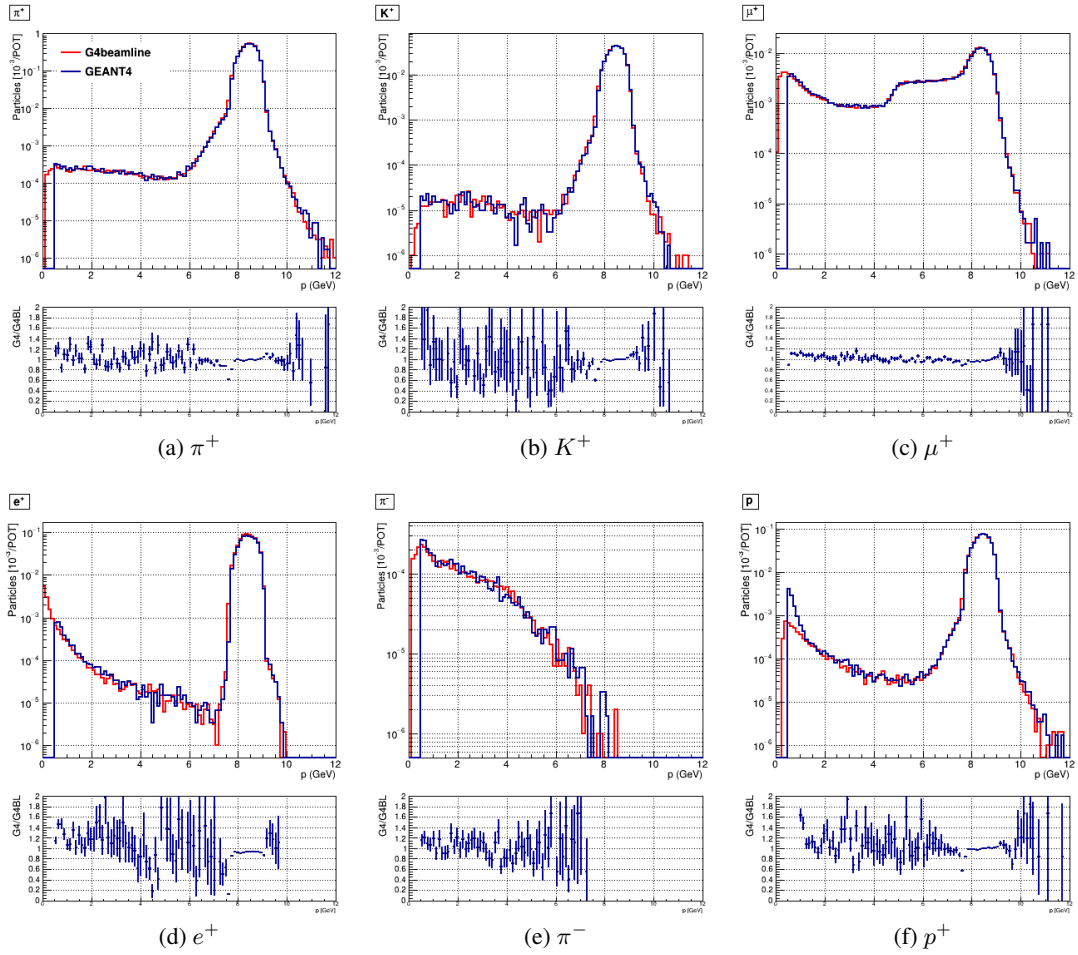

(a) π^+ (b) K^+ (c) μ^+

(d) e^+ (e) π^- (f) p^+

Figure 2.53: G4beamline (red) and GEANT4 (blue) spectra at tagger entrance, with their ratios.

2.6 Partial conclusions on beamline status

The G4beamline simulation is the current reference for the ENUBET collaboration. However, the information gained with GEANT4 is valuable and it is worth continuing to study and develop it. Instead of moving to just one of them, the information from the two simulations will eventually be averaged. In the real-life case, it is important to know that the signal-to-noise ratio is adequate and that the tagger can accurately count correctly.

The detector simulation of Sec. 1.5.3 takes as input the distributions at the tunnel entrance provided by the GEANT4 (or the G4beamline) simulations. Using the information from the GEANT4 output, in particular the particle distributions at the decay tunnel entrance, the detector simulation is run and its own output is used for particle reconstruction and to evaluate the tagger discrimination capability.

The resulting ENUBET performance for signal efficiency and signal-to-noise ratio (S/N) for positrons and muons reconstruction is:

- Positrons: $\sim 22\%$ efficiency, ~ 2 S/N.
- Muons: $\sim 24\%$ efficiency, ~ 6 S/N.

Moreover, the results in terms of neutrino flux would allow to detect 10^4 ν_e^{CC} in 2.4 years, which is a reasonable time for ENUBET operations.

Additionally, the propagated information available from the particle at the target level and along the beamline is used to evaluate the systematics on the neutrino flux (as described in Sec. 1.5.5). Thanks to the GEANT4 information it will be possible to include also the beamline efficiency, by the tuning of the beamline parameters, in the systematics assessment. The resulting uncertainty on the neutrino flux that results from the inputs given by the beamline simulation is $\sim 1\%$, which is in line with the ENUBET purpose.

Chapter 3

Prototypes for the ENUBET tagger

This Chapter describes my work on the hardware R&D for the ENUBET tagger. After an overview of the needs of ENUBET and of the previous prototypes and tests (in which I took part since 2018, in the framework of my master thesis), Section 3.2 is dedicated to the assembly of the prototype referred to as "Enubino". Enubino implemented for the first time the same light readout and geometry that was later implemented in the final prototype of ENUBET. This scheme solves the problem of collecting light coming from different radial layers and bringing it to Silicon PhotoMultipliers (SiPMs) that are placed outside the irradiated area. It also solves in a clean way the problem of making fibers pass through a thick neutron shield made of Borated Polyethylene. I assembled this detector prototype at the Legnaro INFN National Laboratories, where I also worked on its characterization with cosmic rays and on the test of several SiPM models. Section 3.3 describes the CERN test beam I took part in, to study the performance and validate the Enubino concept. The analysis I performed on the test beam data is also described in Section 3.3: I studied the uniformity of response, the efficiency maps and the probability of crosstalk between channels. Thanks to these studies, it was possible to understand that this was a viable detector scheme for the implementation in the final prototype of the ENUBET tagger (demonstrator). During the very last part of my thesis, I was also actively involved with the assembly and tests of the demonstrator as described inSection 3.4.

3.1 Introduction

The ENUBET instrumented decay tunnel is equipped with detectors for measuring the lepton rate (positrons and muons) resulting from kaon neutrinos production vertexes, so to directly estimate the overall neutrino flux. A neutrino whose associated lepton is successfully detected in the instrumented decay tunnel is referred to as "tagged" neutrino, and so is the ENUBET tunnel often called the "tagger". In the present design, the tagger is a 40 m long detector with a radius of 1 m. Particles are generated all along the decay tunnel, and the majority of those hitting the tagger walls come from large angle kaon decay products: most of the particles (Tab.1.6) are muons from the $K_{\mu 2}$ decay ($K^+ \rightarrow \mu^+ \nu_\mu$, with a Branching Ratio of $\simeq 63\%$), then pions from the $K_{\mu 3}$ ($K^+ \rightarrow \mu^+ \nu_\mu \pi^0$, BR $\simeq 21\%$) and the $K^+ \rightarrow \pi^+ \pi^+ \pi^-$ (BR $\simeq 6\%$) decays, and positrons from the K_{e3} decay ($K^+ \rightarrow e^+ \pi^0 \nu_e$, BR $\simeq 5\%$). The main task of the tagger is to

separate positrons and muons arising from kaon decays from other background particles: pions from kaon decays[1] and residual secondary pions transported by the transfer line. The detector will need to distinguish between electromagnetic (EM) showers, Minimum Ionizing Particles (MIPs), and hadronic showers.

Since the majority of particles hit the tunnel walls at angles typically lower than 100 mrad, a good detector option is a calorimeter with longitudinal segmentation, where the modules are built into cylindrical layers so that the axis of the modules is parallel to the beam. The average polar angle depends on the initial momentum of the parent particle and the parent decay kinematics: for the ENUBET secondary beam centered at 8.5 GeV, the beam divergence is $\simeq 3$ mrad [49]. At this energy the average emission angle of the positrons from the K_{e3} decay is about 88 mrad (Fig. 1.7), while the muons from $\pi^+ \rightarrow \mu^+ \nu_\mu$ are emitted at an average of 4 mrad and exit the tunnel without hitting its walls.

The collaboration reached a final design for the detector instrumenting the tunnel as a result of a rich R&D program: a campaign of dedicated simulation studies, measurements, and several test beams carried out at the CERN Proton Synchrotron (PS) T9 beamline [79–82]. In particular, it was found that an iron-scintillator sampling calorimeter, made of compact modules, meets the ENUBET criteria: particle identification capability, cost-effectiveness, and radiation hardness. With respect to the original design presented in [79], radiation hardness was finally achieved by using a Borated Polyethylene shield and long Wavelength Shifting (WLS) fibers to host SiPM away from the inner volume as will be detailed later. Fig. 3.1 shows the general structure of the ENUBET instrumented tunnel.

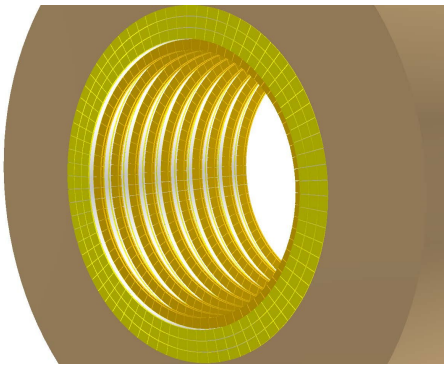

Figure 3.1: A scheme of the ENUBET calorimeter: this section of the decay tunnel, which has a radius of 1 m, is instrumented with three layers of calorimetric modules (green), an inner layer of scintillator tile doublets (a photon veto layer, orange) and an outer layer of Borated Polyethylene (brown). The description of each of these components will be given in detail in the next Sections. The detector will be placed inside the whole decay tunnel, for a length of 40 m, which corresponds to 364 longitudinal layers of modules (10 modules only are displayed in Figure).

[1] It should be noted that pions from kaon decays are also an interesting sample: the flux of ν_μ and ν_e could be inferred from the overall kaon rate, inferred in turn from pion decays corrected for the respective branching ratios (which are known with good precision). The usage of this sample is under scrutiny.

It is possible to successfully tag the neutrinos from the beam only if the background of charged and neutral pions and photons is adequately suppressed. This is especially true for positrons from kaon decays, due to the low branching ratio which makes them much less abundant than pions (from the beam or other kaon decays). Differently, the signal-to-noise ratio of the selected leptons would be too low and, additionally, the problem of pile-up in the readout chain might further compromise the result. A collimated beam of incoming hadrons being well contained in the tagger volume is thus an essential prerequisite. The discrimination between MIPs, hadronic and electromagnetic showers is achieved by measuring the different patterns of the energy deposition in the granular structure of each calorimeter layer, as shown schematically in Fig. 3.2. The current tagger design foresees the use of modules that sample electromagnetic

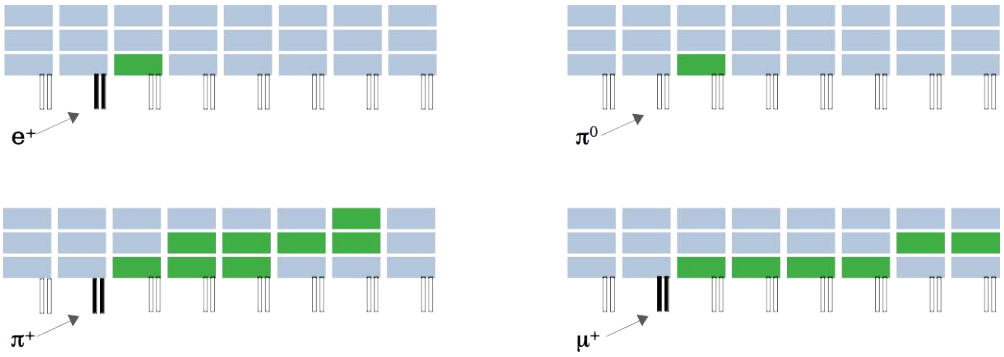

Figure 3.2: ENUBET event topology (schematic): EM shower from a positron, top left; EM shower from a π^0, top right; hadronic shower from a π^+, bottom left, and MIP muon track, bottom right. The modules involved in a typical e^+, π^0, π^+ or μ^+ event are marked in green. In the π^0 case, photons coming from its decay do not leave any signal in the t_0 doublet or might give, in case of conversion, a double-MIP signature.

and hadronic showers every 4.3 radiation lengths (4.3 X_0), which correspond to 0.45 interaction lengths. This design ensures that a positron typically deposits most of its energy in a single detector module. The pattern of energy deposition inside the calorimeter and the differences in electromagnetic and hadronic shower development are both considered to ensure an effective e^+/π^+ discrimination. The basic components of the calorimeter are modules 11 cm long and with a section of 3×3 cm^2. The Molière radius (that determines the transverse dimension of the EM showers) is 1.72 cm for Iron, so each module provides lateral containment up to 2 Moliere radii. Two modules can completely contain electromagnetic showers from positrons in the region of interest of 1-3 GeV, while hadronic showers induced by pions are more penetrating and involve more modules.

A photon veto layer, also referred to as "t_0 layer", is included in addition to three calorimetric layers, to cope with the abundant presence of photons coming from the decay of neutral pions. It is the innermost layer of the tunnel instrumentation and it is made up of two scintillator tiles for each module in the inner calorimeter layer. These tiles are 0.7 cm thick, corresponding only to 0.012 X_0. Typically a charged particle passing through a scintillator tile (such as the t_0 tiles) produces light, leaving a detectable signal. Neutral pions decay into two photons, each one can

be either converted into an electron-positron pair in the scintillator material or hit the calorimeter (with an EM shower indistinguishable from the positrons one, but without giving a signal in the t_0 tiles). An e^+/e^- pair will hit the veto with a larger signal than a positron only, allowing the distinction between a signal positron and a background from neutral pions. Figure 3.3 illustrates the principle of operation of the t_0 doublet. The different patterns of energy release in the

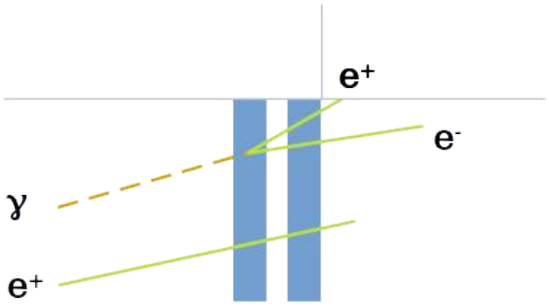

Figure 3.3: Working principle of the t_0 layer. The photon veto is composed of doublets of plastic scintillator tiles mounted below the calorimeter modules. The correlation between the two signals allows distinguishing between the passage of 1 or 2 MIPs.

calorimeter modules are at the basis of the ENUBET reconstruction algorithm, which relies on a multivariate approach that was described in Sec. 1.5.4.

Each module is read out by WLS fibers that carry the scintillating light to Silicon Photomultipliers (SiPMs). A SiPM is a matrix of avalanche photodiodes operated in discharge mode (Geiger mode) [83]. Each of them is followed by a quenching resistor, and all of the pixels are read out simultaneously on the same substrate. The total signal of all pixels is proportional to the number of photoelectrons on the SiPM, in ideal operating conditions. One advantage of employing SiPMs as scintillation light detectors is their compactness, which enables longitudinal sampling and reduces dead zones by allowing them to be incorporated directly into the calorimeter bulk. This allows for the design of so-called Ultra Compact Modules (UCMs) [84]. SiPMs, however, are quite susceptible to radiation damage, especially from neutrons. Dedicated tests (described in Sec. 3.1.2) studied these effects. The design of the ENUBET calorimeter is flexible and the SiPMs can be either embedded in the calorimeter or removed from it. Eventually, the "lateral" light readout system (employing LCMs, Lateral Compact Modules) alternative replaced the initial "shashlik" configuration for the calorimeter modules [85]. The next Sections summarize the validation of the calorimeter prototypes in both shashlik and lateral readout modes.

The design of the calorimeter has been improved during the past two years and the innovations have been tested thanks to a small prototype, "Enubino", that features the definitive detector solutions of the tagger. The final goal of ENUBET regarding the instrumentation of the decay tunnel is to build and test a tagger prototype, referred to as the "Demonstrator" that extends to a much larger scale the detector concept first tested on the ENUBINO prototype.

3.1.1 Calorimeter prototypes

The first prototypes tested by the ENUBET collaboration were shashlik calorimeters: sampling calorimeters composed of light collection tiles and absorber tiles sandwiched together, with readout optical fibers running perpendicularly to the tiles. Due to the size of the light collection devices (PhotoMultipliers, PMT), the primary disadvantage of shashlik calorimeters in the past was their lack of longitudinal segmentation: the dead zones resulting from fiber extraction and transport to the PMTs were too wide to maintain a good energy resolution. However, the advancements in SiPM technology made it possible to get over this obstacle. SiPMs are small sensors; a compact device can be created by directly connecting the SiPMs to the optical fibres and enclosing them within the calorimeter's main body. This method combines good compactness and a practical cost-saving solution.

The SCENTT Collaboration [84] created the shashlik-based reference module (UCM) of ENUBET in 2016. It is made of 3×3 cm^2 iron tiles that are 1.5 cm thick, interleaved with 0.5 cm thick plastic scintillators. The scintillator material used was either EJ-200 [86] or BC-412 [87]. A diffusive TiO_2 coating (EJ-510) was applied on the scintillator surfaces to improve light collection efficiency. Comparing this method to more traditional procedures used in shashlik devices (e.g. insertion of Tyvek foils between the scintillator and absorber tiles), this technique significantly simplifies the construction of the modules. Nine Kuraray Y11 fibres, with a diameter of 1 mm, were used to gather the scintillation light. They pass through the five iron and scintillator tiles in the UCM, each one through one hole per square centimetre (of a diameter of 1.2 mm). To avoid oxidation, an electrolytic zinc plating was applied after drilling the iron tiles. Each fiber was coupled to one 1×1 mm^2 SiPM, that was housed on a shared printed circuit board where the output signals from the same tile are summed and sent to the front-end electronics. The longitudinal sampling of the calorimeter was determined by the length of the fibers crossing the scintillator and absorber tiles; the transverse granularity of the modules was fixed by the tile size and the total number of summed SiPMs. Fig. 3.4 shows a schematic representation and a picture of a shashlik module.

Shashlik calorimeters composed of UCMs were built and tested by the ENUBET Collaboration in 2016 [79]. In July 2016, the first shashlik calorimeter (Fig. 3.5a) was tested with a particle beam composed of electrons, muons, and pions in the 1–5 GeV energy range. The prototype was an array of 4×3 UCMs (in the transverse and longitudinal directions). With a length of 12.8 X_0, it could contain 90% (80%) of the EM showers at 1 (5) GeV, while the containment in the transverse direction amounted to 92% at 5 GeV. Each fiber is read out by 1×1 mm^2 20 μm SiPMs, produced by FBK, operated at an overvoltage (OV) of 5 V. An energy resolution of 18% (11%) at 1 (4) GeV was shown by the test beam, corresponding to a stochastic term of 17.5%, in compliance with the Monte Carlo simulations. The response of the calorimeter was linear up to 5 GeV where a 3% non-linearity was found.

A calorimeter consisting of 56 UCMs was tested in the same conditions in November 2016 (Fig. 3.5b) together with an energy tail catcher, built with the same technique used to create the UCM, but with a coarser granularity (larger scintillator tiles). The full containment of electromagnetic showers and the longitudinal containment of hadronic showers are made possible by 7 modules in the longitudinal direction and 4×2 modules in the plane perpendicular to the beam.

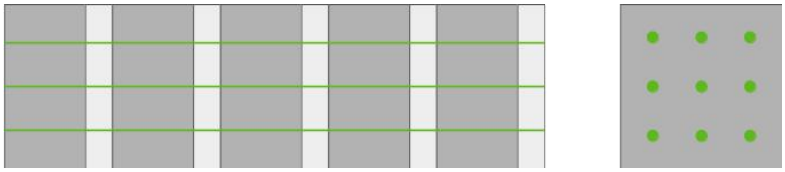

(a) Shashlik structure

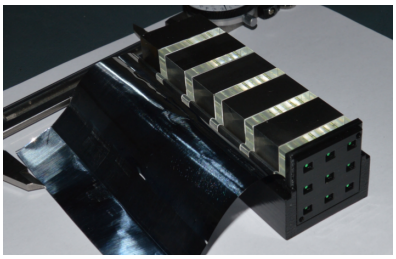

(b) An UCM realized by the SCENTT Collaboration

Figure 3.4: A shashlik UCM.

1×1 mm^2 SiPMs with a cell size of 20 μm, produced by FBK [88] but with different specifications with respect to the previous test beam, were employed and operated at 8 V overvoltage. The resulting energy resolution was 17% at 1 GeV.

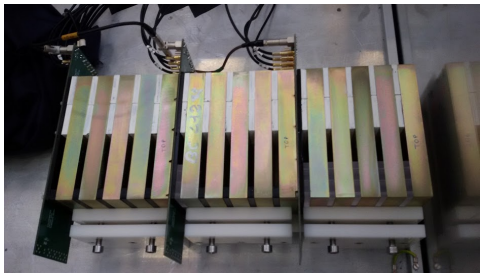

(a) 4×3 prototype

(b) $4\times2\times7$ prototype

Figure 3.5: Shashlik prototypes tested in 2016.

The tests of the shashlik prototypes validated the performances in terms of electromagnetic resolution predicted by the Monte Carlo simulations and demonstrated that fine-grained segmentation can be achieved by embedding the SiPMs in the bulk of the calorimeter.

As an alternative to the common plastic scintillator, the ENUBET collaboration tested a silicon-based scintillator shashlik prototype in 2017 [81]. Polysiloxane-based materials provide some advantages with respect to conventional plastics scintillators: increased radiation tolerance, slower ageing, a lack of irreversible damage from mechanical deformation, and the absence of drilling requirements for shashlik applications. All these benefits come at the ex-

pense of a lower light yield: the thickness of the active material was increased to 1.5 cm for each layer, with respect to 0.5 cm for the previous prototypes, to compensate for the loss. The Polysiloxane mixture can be poured into separated compartments, ensuring a good coupling to fibers. The prototype (Fig. 3.6) had 2×2×3 UCMs with iron and scintillator layers 1.5 cm thick. It presented performances comparable to conventional plastic scintillators: an energy resolution of 17% at 1 GeV and good linearity in the 1-3 GeV energy range.

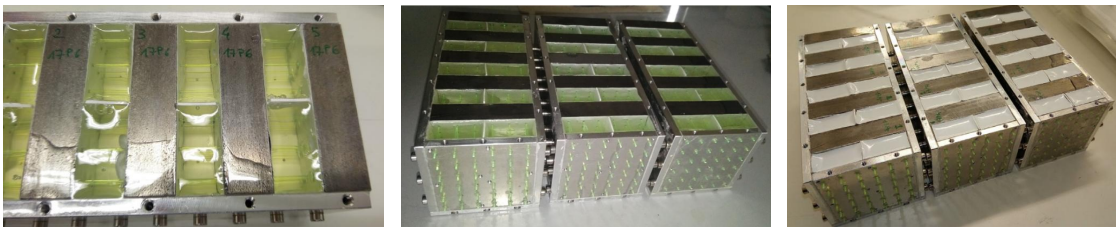

(a) Polysiloxane poured into the compartments

(b) Hardened Polysiloxane

(c) Polysiloxane painted with diffusive coating

Figure 3.6: Polysiloxane prototype.

SiPMs are sensitive to radiation damage. One benefit of using SiPMs as scintillation light detectors is their compactness, which enables longitudinal sampling and reduces dead zones by allowing them to be incorporated into the calorimeter UCMs. As a result of this solution, the SiPMs are exposed to fast neutrons generated by hadronic showers. SiPM irradiation may cause damage to the crystal lattice, which in turn causes signal loss and an increase in dark current. Therefore, the SiPMs were tested in a dedicated irradiation campaign at the CN facility at INFN-LNL, where SiPMs with different cell sizes were irradiated with fast neutrons up to 2×10^{11} n/cm^2. This fluence represents the cumulative dose of the ENUBET innermost calorimeter layers during the course of the experiment. The dark current after breakdown increases by more than two orders of magnitude at this dose. At a fluence greater than 3×10^{9} n/cm^2, sensitivity to a single photoelectron is lost. The response to electrons and MIPs of a UCM with an irradiated board (of nine 1 mm^2 SiPMs with 15μm cell size) is comparable with the response prior to irradiation. The results [80] support the use of irradiated SiPM for the ENUBET light readout system if there are enough photoelectrons to detect the MIP (more than 50 p.e. per MIP). This requires either increasing the scintillator thickness for the typical UCM prototype (of about 1 cm) or increasing the efficiency of light collection at the SiPM to fiber interface. As a result, the lateral light readout system (the concept of removing the fibres from the calorimeter) replaced the shashlik option in the new prototypes.

In 2018 the ENUBET collaboration developed a new calorimeter prototype, the lateral calorimeter, employing this readout scheme. Its LCMs were very similar to the first shashlik UCMs: it was made of a stack of Iron tiles (1.5 cm thick) as the absorber material and EJ204 [86] plastic scintillator as the active material (0.5 cm thick). However, the fibers were extracted by the sides of each scintillator tile. The fibers could then be bundled together on top of the calorimeter so

that the light readout sensors (SiPMs) were no longer inside it. This, added to the advantage of not having to drill the iron and scintillator tiles, is an appealing solution for the building of the ENUBET calorimeter. The scintillator tiles were first painted with the diffusive TiO_2-based coating and then two WLS Saint Gobain BCF92 fibers (diameter: 1 mm) were glued to each side. The three layers of LCMs are shifted of 3.5 mm with respect to each other, because of the extraction of the fibers: they must be coupled only to one scintillator tile, without gathering light from the above plane. Iron tiles include grooves on both sides to facilitate fiber passage (as shown in Fig. 3.7b

(a) Calorimeter with t_0 layer (b) Grooves detail

Figure 3.7: Lateral calorimeter prototype.

The first prototype was tested in May 2018. It consisted of 18 modules and was read out by 4×4 mm^2 SiPMs, produced by AdvanSiD [89]. Each SiPM read 10 fibers, corresponding to 5 scintillator tiles (1 LCM). This determines the longitudinal sampling (as well as the transverse granularity). The SiPMs operated at overvoltages from 3.5 to 5.5 V. A second larger prototype was then tested in September 2018. Employing the same method, two new blocks of LCMs have been built. Scintillator tiles were 0.4 mm thicker, resulting in a LCM length of 10.2 cm, instead of 10.0 cm. One block was equipped with Saint Gobain BCF92 fibers, and the second one with either Saint Gobain BCF92 or Kuraray Y11. In addition, an Aluminum-based paint was used on the fiber ends that were glued to the scintillator tiles to improve light transmission within the fiber. The same AdvanSiD 4×4 mm^2 SiPMs were used. The complete prototype consisted of 84 LCMs in a $3\times4\times7$ structure. In addition, this prototype was equipped with a t_0 layer built similarly to the LCMs (Fig. 3.7a).

The test beam campaign showed [82] that in the energy range of interest for ENUBET (1-3 GeV), the calorimeter response to pions, electrons, and muons was in good accord with predictions; minor inconsistencies in the electron response were found above 4 GeV. At 1 GeV, the electromagnetic resolution was 17%, and the sampling term was the dominant contribution between 1-3 GeV. The partial saturation of the SiPMs and the non-uniform response of the LCMs caused non-linearities in the electron response, which were observable at higher energies. The photon veto was tested both separately and in combination with the calorimeter. The 1 MIP sample could be separated from the 2 MIP component with a purity of 95%.

3.1.2 Silicon PhotoMultipliers

The lateral readout system requires to employ large-area SiPMs, in order to bundle together the 10 fibers corresponding to each LCM. The SiPMs used during the lateral calorimeter tests were manufactured by AdvanSiD [89]. They were tested together with the calorimeter during the test beam, but also later in dedicated setups. test beam results indicated a non-linearity in the calorimeter response to electrons (3%/7% deviation at 4/5 GeV). The majority of this impact was attributed to the SiPMs saturation, which is due to their high cross-talk at the utilised bias of 31 V. Cross-talk occurs when a primary avalanche process in a cell triggers a secondary discharge in a neighbouring cell.

Dedicated tests showed that the cross-talk probability P_{x-talk} is $P_{x-talk} = 44\%$ at V_{bias} 31 V (and $P_{x-talk} = 65\%$ at V_{bias} 32 V) [82]. Thus, the number of firing cells on the SiPM increases, from the (ideal) number of photons N_γ impinging on the surface to

$$N_{fired} \equiv (1 + P_{x-talk}) \times N_\gamma$$

Considering the diameter of the fibers (1 mm) and the size of the SiPMs (4×4 mm^2), the covered area is about 50%. The finite number of available cells on the SiPM limits its response. This correction factor was applied to the test beam data, and it was found that the saturation effects completely account for the non-linearities up to 4 GeV.

A possibility would be to increase cell count, and avoid saturation, passing from 40 μm cell SiPMs to 30 μm cell (and below) SiPMs. Three new SiPM models, manufactured by FBK [88], became available before the construction of the last ENUBET prototype and were tested before equipping the Enubino pre-demonstrator (see Sec. 3.2). Later, also a SiPM from the Hamamatsu company [90] was acquired and tested directly on the prototype (Sec. 3.3.3). A summary of the available models is the following:

- AdvanSiD RGB SiPMs (used during the 2018 test beam of the lateral prototype, Fig. 3.8a);
- five FBK RGB HD, in three different cell sizes (Fig. 3.8b);
- one Hamamatsu S14160-4050HS .

The relevant SiPM paremeters are written in Tab. 3.1. They have been all tested on the Enubino prototype as described in the next Sections.

Model	Cell size	Measured V_{bd}
AdvanSiD	40 μm	27 V
FBK	30 μm	27.9 V
	25 μm	28.5 V
	20 μm	28.4 V
Hamamatsu	50 μm	38 V - datasheet

Table 3.1: SiPM parameters.

(a) AdvanSiD (b) FBK

Figure 3.8: SiPMs for the ENUBET calorimeters.

3.2 The "Enubino" prototype

Enubino is the most recent prototype for the ENUBET tagging calorimeter. It employs a novel light readout technique that was tested with cosmic rays at INFN-LNL and with particle beams at CERN-PS East Area, in order to assess its performance. It is composed of five channels, which make up a single azimuthal segment of a bigger prototype (the Demonstrator) that is currently being built as a deliverable of the ENUBET project (see Sec. 3.4).

Out of the five channels of Enubino, two of them read out the t_0 doublet. The remaining three channels are the three LCMs that compose one unit made of three layers of the final calorimeter. The structure of Enubino is shown in Fig. 3.9.

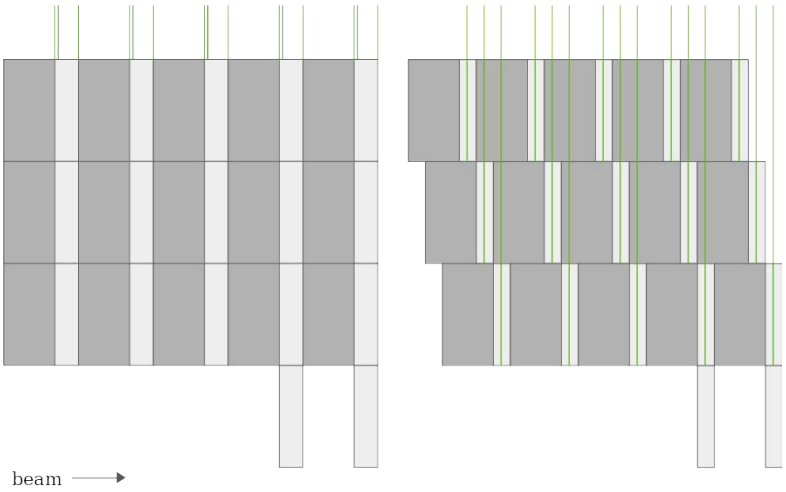

Figure 3.9: Enubino structure (left), compared with the lateral calorimeter layout (right). In ENUBINO the WLS fibers run along the larger face of the scintillators, within "transit", optically isolated grooves and the absorber planes have the same longitudinal position in the different radial channels. In the lateral readout calorimeter fibers were reading light from the scintillators' small sides and absorber planes were staggered and properly machined to allow the passage of the fibers (more challenging for mechanics in case of a large detector).

Similarly to the Lateral prototype, the LCMs of Enubino are composed of five 1.5 cm thick iron slabs interleaved with 0.7 cm (0.5 cm for the Lateral calorimeter) plastic scintillator tiles (made of Polyvinyltoluene); each module has a section of 3×3 cm^2. However, the longitudinal planes are no longer shifted with respect to each other: Enubino employs a new readout scheme that ensures optical isolation between the modules. As a consequence, the iron slabs for each layer are actually a single piece of iron with a section of 3×9 cm^2. Each tile is read out by two WLS fibers, that are collected in the upward direction with reference to Fig. 3.9. Fibers have a diameter of 1 mm each and are glued to the grooves (1 mm deep) hosted by the scintillator tiles. This new readout scheme is shown in Figure 3.10. Enubino employs frontal grooves instead

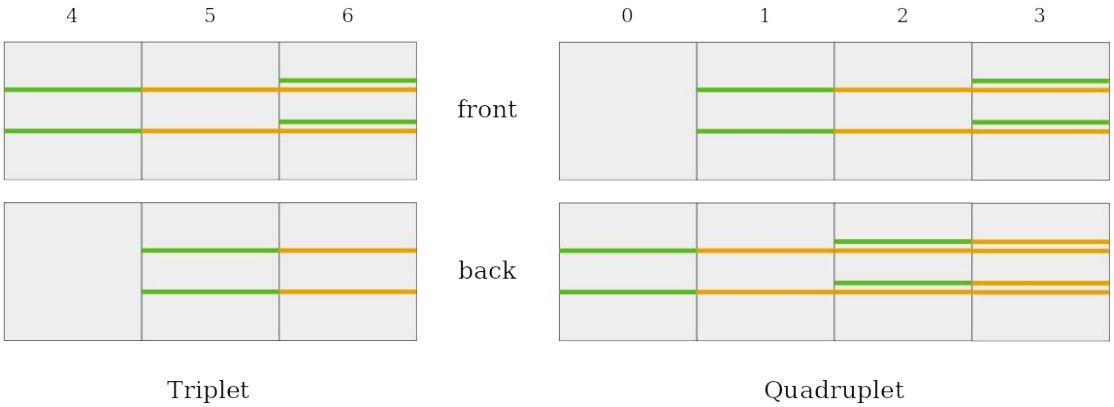

Figure 3.10: Grooves for fibers routing across the Enubino scintillator tiles: readout grooves (green) and transit grooves (orange).

of lateral grooves: this means that the scintillator tiles need to host also the fibres that read the other tiles. “Readout” grooves are defined as the grooves to which the fibers are glued for light collection. “Transit” grooves are meant to host the readout grooves coming from the other tiles and they must not collect light from the tile they are crossing. Each tile has a different layout in terms of the number of collecting and transit grooves, that can be glued either to the front or the back of each tile. Since the t_0 tiles are embedded in the Enubino prototype, Enubino can be seen as composed of three layers of “triplets” and two layers of “quadruplets”. The triplet, composed of tiles conventionally numbered 4, 5 and 6 (Fig. 3.10, left) must host 3 couples of fibers. The readout grooves, marked in green, on tile 5 are on the back face and correspond to the transit grooves (for fibers reading tile 4) on the front face. For tile 6 the readout grooves must be placed in a slightly offset position (2 mm away) with respect to the transit grooves (that host fibers reading tile 4). The same pattern repeats for the quadruplet (Fig. 3.10, right), with the further complication of having a fourth tile from the t_0 layer that must be included in the design. For the quadruplet, tiles are numbered from 0 to 4, so that the first LCM is composed of tiles numbered “1” and “4”, the second one of tiles “2” and “5”, and the third one of tiles “3” and “6”. Tiles “0” belong to the t_0 doublet. The tiles were produced by UNIPLAST and are shown in Fig. 3.11, while Fig. 3.12 shows what a quadruplet looks like.

Enubino is equipped with Kuraray [91] Y11 WLS fibers, that were cut in four different lengths in order to allow around 50 cm for fiber routing above Enubino. A thin layer of

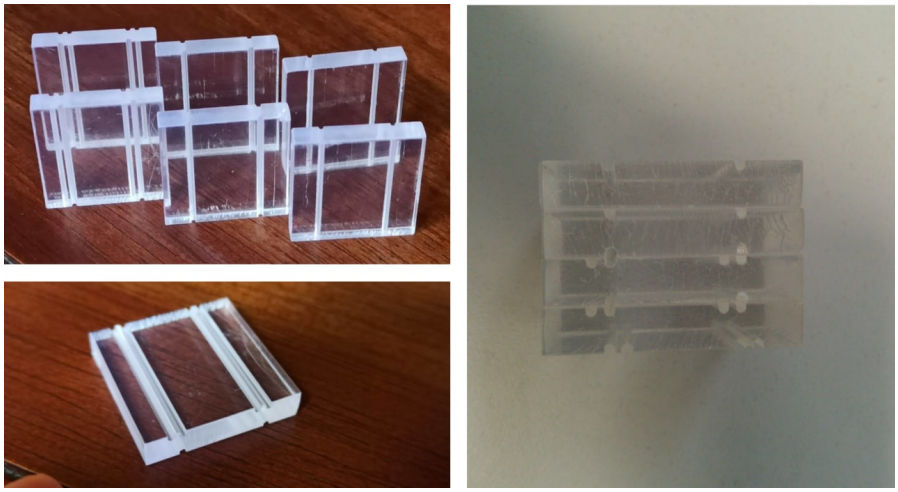

Figure 3.11: Different types of scintillator tiles.

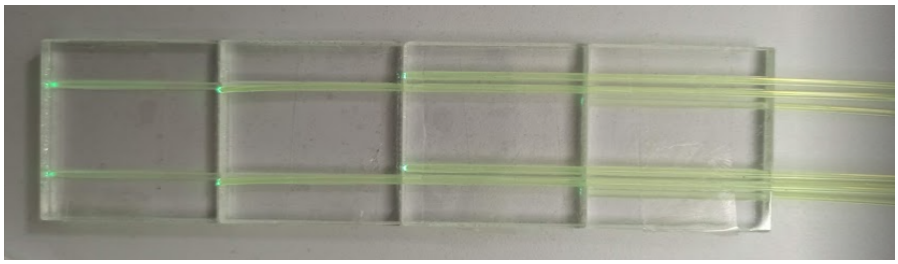

Figure 3.12: Quadruplet of Enubino scintillator tiles.

Aluminum-based paint was applied to the not collecting end of the fiber (the end glued to the scintillator tiles), in order to increase light transmission inside the fiber. A new constraint of this scheme is that the transit grooves must be optically isolated. The procedure observed is the following: first, the end of each fiber must be levelled and polished; then, the Aluminum coating (a commercially available paint) is applied to the fiber. The paint should dry in a matter of hours, in the meanwhile also the grooves must be polished. After the paint is dry, fibers are glued to each tile using the EJ-500 optical cement [86, 92]. The result of this operation is shown in Fig. 3.13. This glue takes a couple of hours to set, but up to 24 hours to completely harden.

Scintillator tiles were then painted with a diffusive TiO_2-based coating (EJ-520 [86, 93]) intended to increase light collection efficiency inside the tiles and make them optically opaque on the outside. Three layers of paint are necessary to adequately cover the tiles while keeping the additional thickness of the paint to a reasonable level. The two key parts of the procedure are the grooves painting and the cleaning of the fibres. Regarding the grooves, if there is too much paint inside they may become clogged. The painted tiles must be put horizontally while drying for the same reason. Scraping out the additional paint (and re-applying the correct amount) is possible, though time-consuming. A second precaution to be taken is not to let too much paint leak on the portion of the fibres that are not glued to the scintillator: even a thin layer can prevent

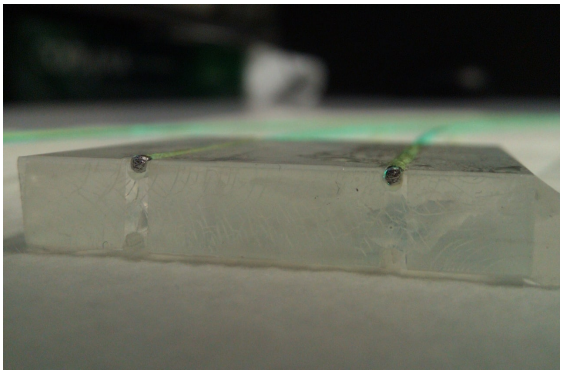

Figure 3.13: Aluminium-painted end of fibres glued to a scintillator tile.

the fibre to fit in their transit grooves. The best way to clean the fibers in case this happens is to use an ethanol-based solvent, that dissolves the paint without damaging the fibres' material. Enubino's painted tiles are shown in Fig. 3.14. Each layer of paint dries in $\simeq$ 20 minutes at 40°, and the painted tile totally hardens after $\simeq$ 24 hours at room temperature.

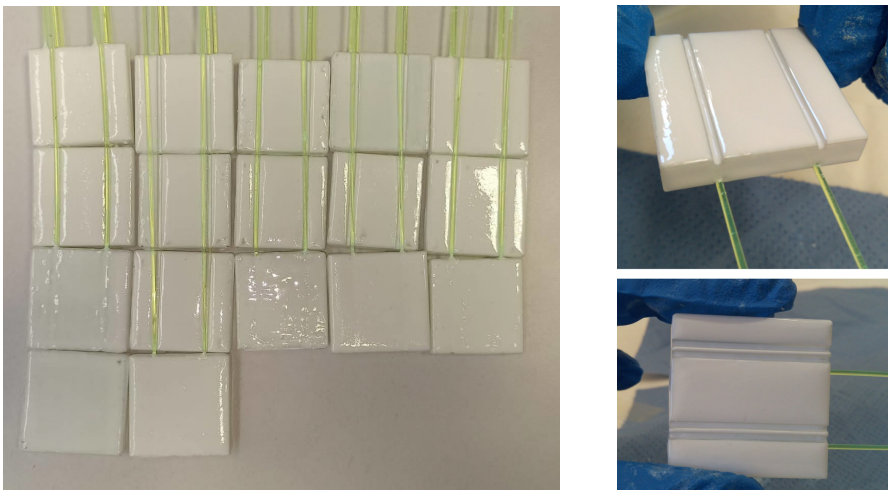

Figure 3.14: Painted scintillator tiles for Enubino.

The SiPMs that read out the scintillation light from Enubino are protected by a shielding of Borated Polyethylene (BPE) 30 cm thick. According to FLUKA simulations [52], a reduction of factor 20 in the neutron flux can be achieved thanks to this shield. The BPE was machined in order to create grooves that serve as fiber routers, as illustrated in Fig. 3.15. There are around 15 cm left after the BPE components for the coupling of the fibers to the SIPMs. Fibers corresponding to the same channel (three LCMs and two t_0 tiles) must be bundled together. The first attempt consisted of a hand-made socket for the SiPMs and a perforated layer to let the fibers pass through without employing glue. However, the fibers retreated easily and did not remain in place against the SiPMs, so the Silicon area was not exactly in front of the fiber holes. The

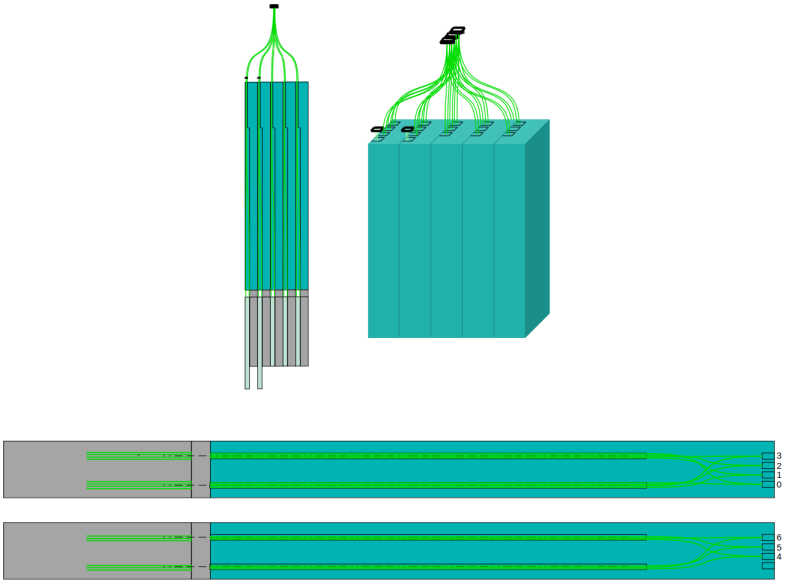

Figure 3.15: Enubino sketch, with fiber routing through BPE.

best option is to glue the fibers to the existing connectors made for the lateral calorimeter and to design and 3D-print the new SiPM sockets (Fig. 3.16).

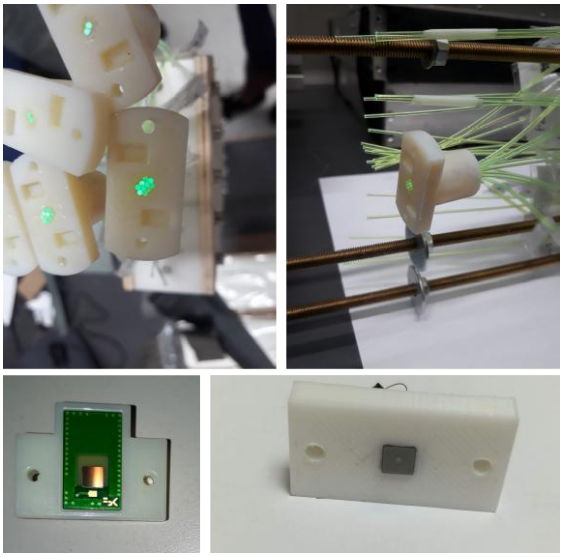

Figure 3.16: Connectors with glued fibers (top) and sockets for the FBK (bottom, left) and the Hamamatsu SiPMs (bottom, right).

The assembly of the prototype is shown in the following Figure 3.17

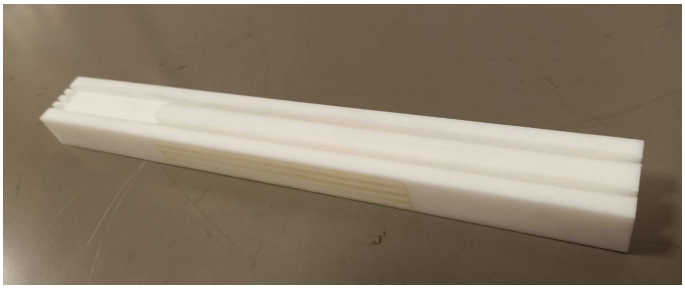

(a) BPE

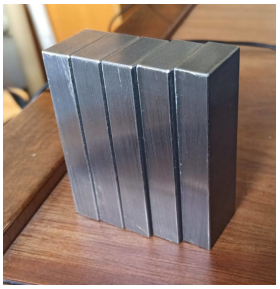

(b) Iron

(c) Fiber routing

(e) Side view

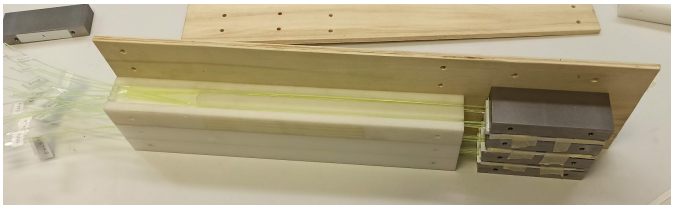

(d) Building of the planes

(f) Assembled Enubino

(g) Detail

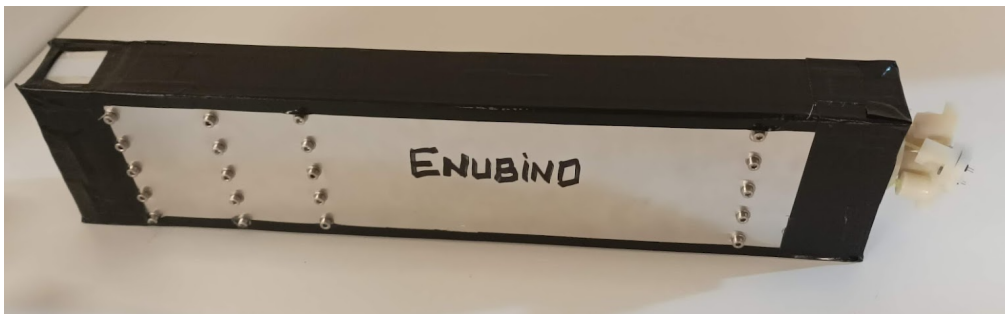

(h) Enubino

Figure 3.17: Assembly of the Enubino prototype at INFN-LNL.

3.3 Results of the Enubino prototype test beam

Enubino was built at the INFN Legnaro National Laboratories, where also the first tests were performed. Enubino was equipped with the five FBK SiPMs and it was positioned inside a darkened box, between two trigger scintillators 3.18.

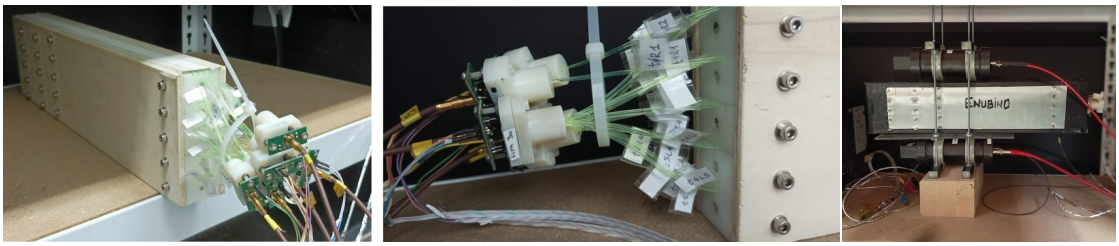

Figure 3.18: Enubino cabling and setup at the LNL.

Cosmic data demonstrated that Enubino indeed produces scintillation light and allowed for the first characterization of the FBK SiPMs. Enubino was then characterised with charged particle beams at CERN-PS East Area [94] in November 2021.

3.3.1 Test beam setup

The SiPMs used to read the channels of Enubino were darkened, and then Enubino was placed on a platform inside the experimental area, aligned with the beam. Some supplementary detectors

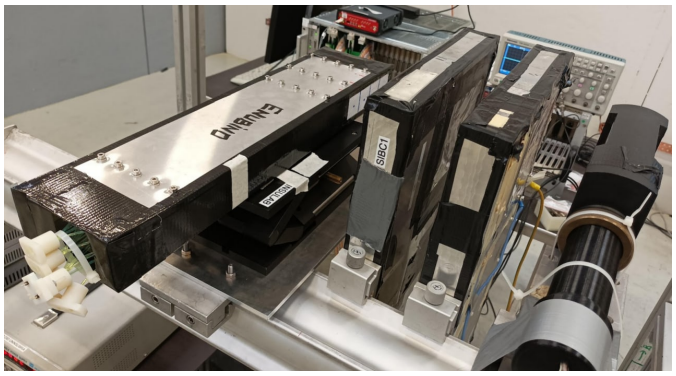

Figure 3.19: Enubino and the auxiliary detectors placed in the experimental area.

were used for the data acquisition and analysis. From upstream to downstream, the arrangement of the detectors in the T9 area (that can be seen in Fig. 3.19) is the following:

- a 10×10 cm^2 plastic scintillator;
- two pairs of Silicon strip planes;
- Enubino.

The plastic scintillator placed upstream of the Silicon chambers served as a trigger for the DAQ (Data Acquisition System). The signal in the plastic scintillator, in coincidence with the beam spill, set off the acquisition. The Silicon strip detectors are used to reconstruct tracks: they are made of two planes each, with the strip orientation of the first plane perpendicular to the one of the second plane. Hence, they give information on x and y of the impact point of particles on them, with a resolution of 30μm. Using the two of them allows the reconstruction of tracks, by projecting the particle tracks down to the upstream face of the calorimeter. The precision is limited by the precision of measured distances between the detectors (about 1 mm). The layout of the instrumentation in the experimental area is summarized in Fig. 3.20.

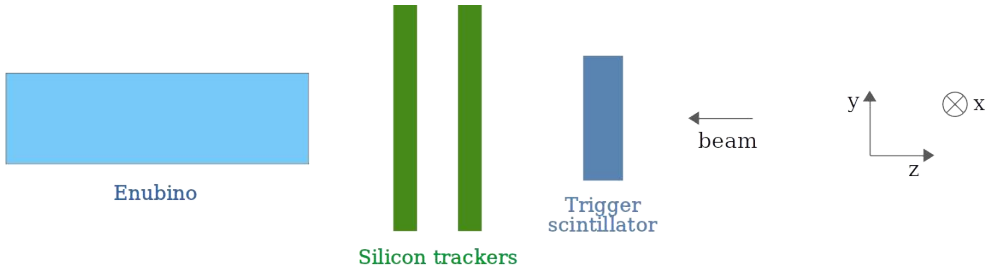

Figure 3.20: Layout of the detectors in the experimental area.

Data were acquired at 15 GeV mainly with the front face of the tiles of Enubino perpendicular to the beam, as shown in Fig. 3.21.

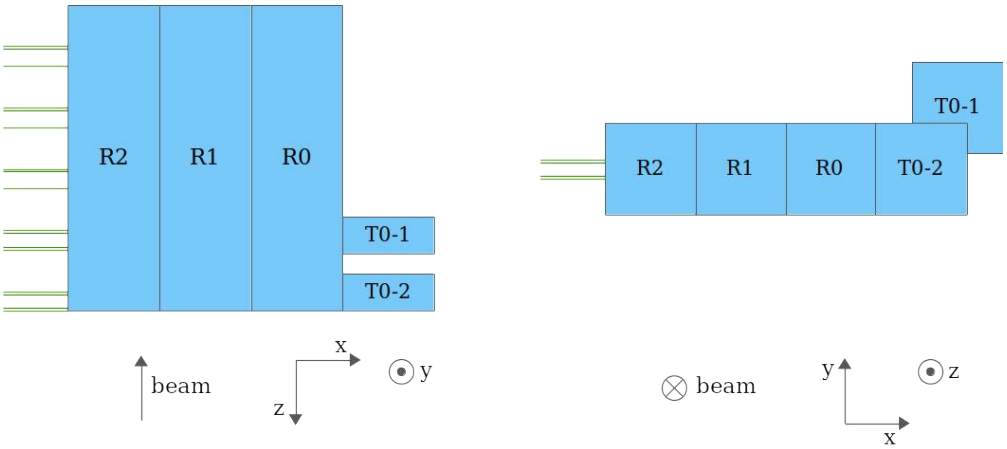

Figure 3.21: Coordinate system of Enubino in the experimental area.

The coordinate system in this Figure has been employed during the data analysis carried out in the next Sections. The naming convention used for the 5 channels of Enubino is the following:

- the channel corresponding to the "external" t_0 tile, which means the tile facing directly the beam in the configuration of Fig. 3.21, is called "T0-2";

- the second t_0 tile is the "T0-1" channel;
- the three LCM channels are named "R0", "R1" and "R2", where R0 is the module closest to the t_0 doublet and R2 is the last module before the fibres' extraction.

Waveform digitizers were used to read SiPM signals (model DT5730, input range 2 V, by CAEN [95]). The information from the trigger, the silicon strip detectors (the 4 hit positions on the strips), and the SiPM outputs (pulse height of the maximum) are collected and stored into ROOT files. These files contain also the complete waveforms for the 8 channels of the digitizer.

The available beam was a narrow positive 15 GeV beam. The measurements from the Silicon trackers of the beam's spatial and angular properties are presented in Fig. 3.22. The beam

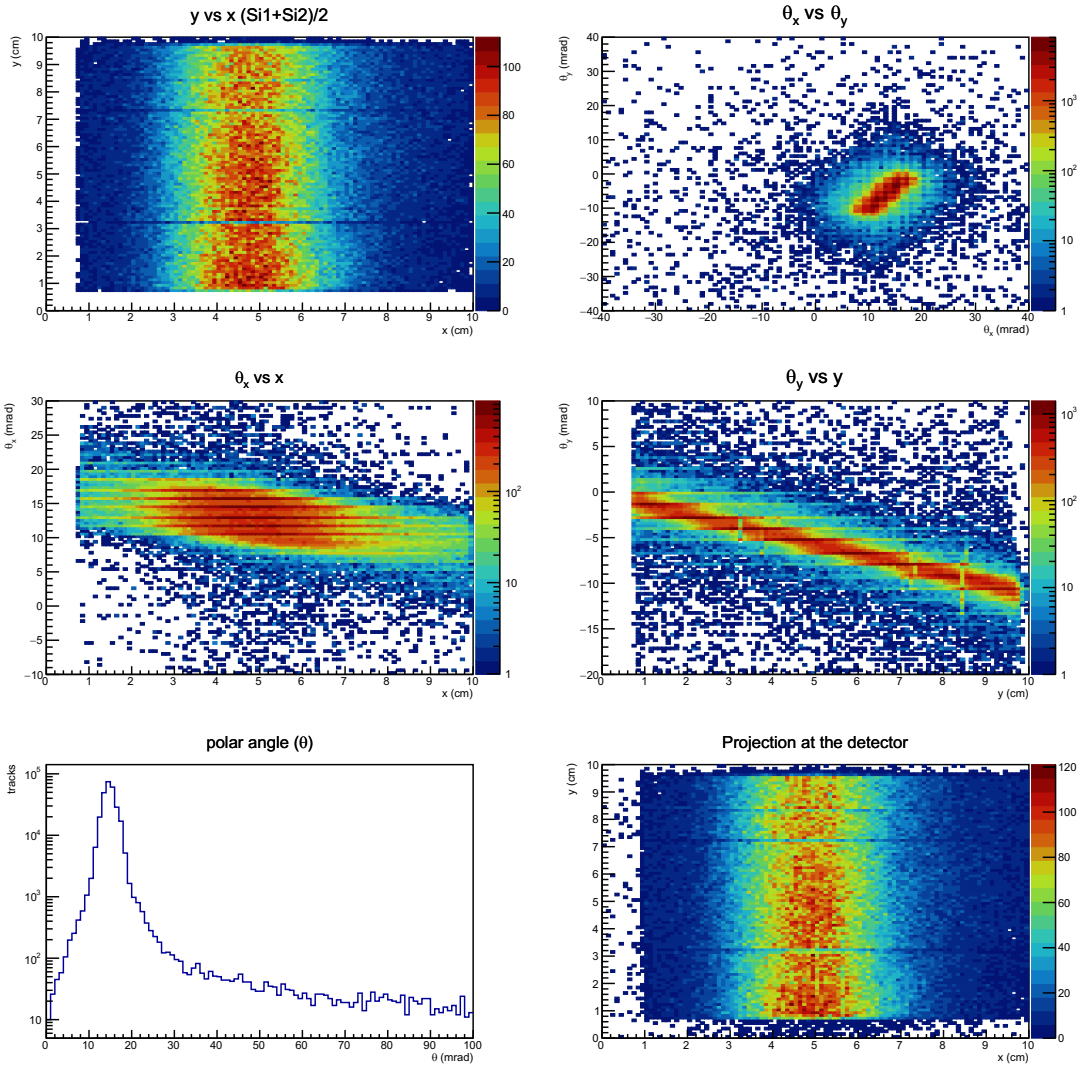

Figure 3.22: +15 GeV beam properties at the level of the Silicon tracker.

profile had a Gaussian shape in the horizontal x direction, with a sigma of σ_H =1.5 cm, and a flat distribution in the vertical y direction. Enubino was placed with its long side along the x direction. Runs at different positions were taken and merged after the Enubino position reconstruction. Particle identification was not possible, since the Cherenkov detectors that are usually present at the T9 beamline were malfunctioning at the time of the test beam. From the available documentation [96] this beam was mostly composed of protons (around 95%), that at 15 GeV behave as MIPs and can be used for the Enubino studies.

3.3.2 MIP identification

The raw spectra obtained from the digitization of the five SiPMs signals are shown in Fig. 3.23a. Information from the trigger scintillator is used to select only on-time events, in order to reject background signals or accidental coincidences. Fig. 3.24 shows for each channel the digitized time of arrival. With the suitable cut (dashed lines in Figure) only on-time particles are selected (Fig. 3.23b).

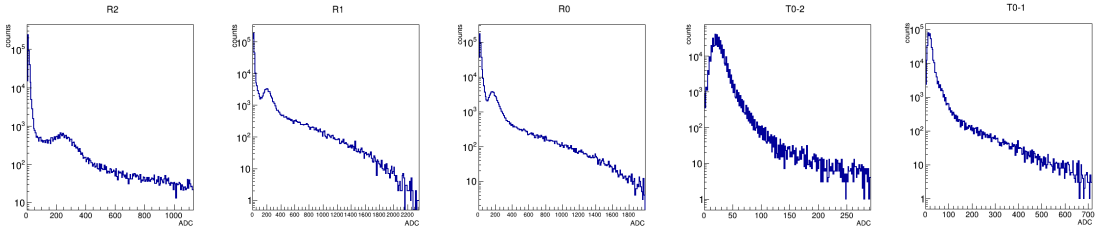

(a) Raw signals

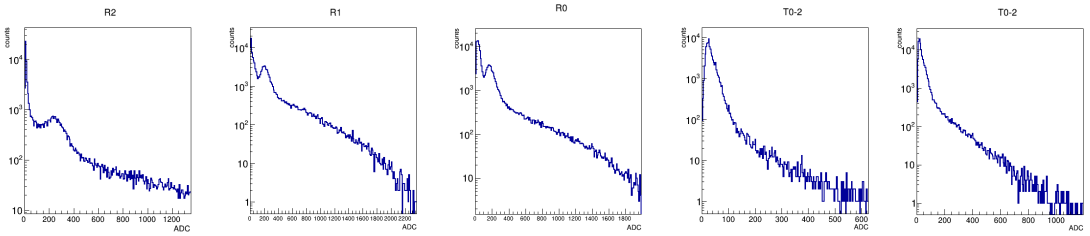

(b) On-time signals

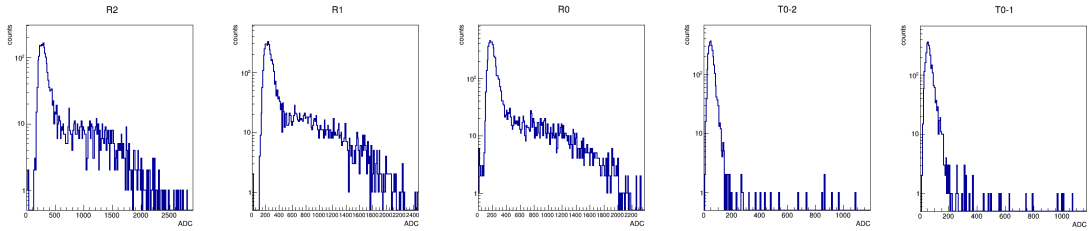

(c) Hitting area of 1 cm^2

Figure 3.23: Cleaning up of the spectra.

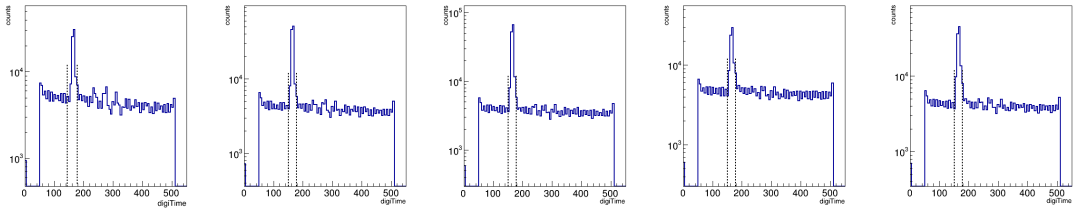

Figure 3.24: Digitized time of arrival.

Because of the absence of other means of particle identification, the only way to get rid of the baseline and get a cleaner signal is to select only particles crossing a fiducial area on the detector. The efficiency map provides the position of Enubino as seen from the beam. The position of Enubino is reconstructed, thanks to the information from the Si trackers, by selecting an ADC threshold and plotting in x and y the ratio between signals above this threshold over all the signals of the reconstructed tracks. The plots in Fig. 3.23c are obtained by selecting only particles crossing a 1 cm^2 area at the center of each module. This allows the elimination of particles hitting Enubino from the side, thus not crossing all five scintillator tiles. The spectra present a peak due to the MIP energy deposit and a tail to its right side, due to the hadronic interactions of protons (Fig. 3.25 shows the difference between the proton beam and cosmic data). The MIP peak is well visible and the MPV (Most Probable Value) of the distribution has been extracted by means of a convoluted Landau-Gaussian fitting function (Fig.3.26).

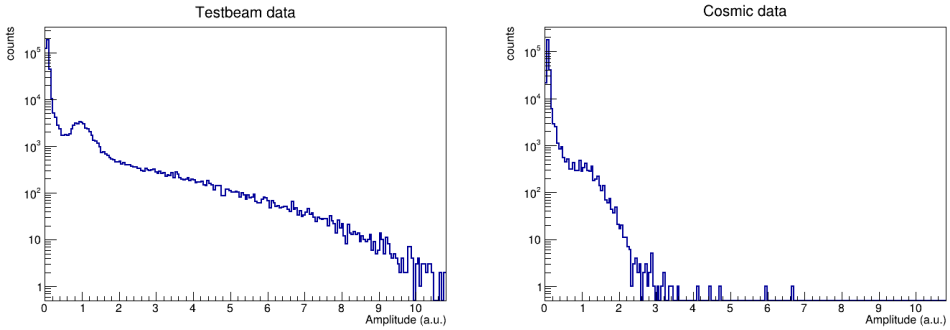

Figure 3.25: Raw spectra of R1 acquired during the test beam (left) and with cosmics (right). In the former case, the tail is due to proton interactions.

The spectra can be either read in terms of ADC counts or, if some comparison with spectra obtained with different instruments is required, they can be transformed in mV. The DT5730 digitizer has a dynamic range of 2 V and a resolution of 14 bit, hence each ADC count corresponds to 0.122 mV.

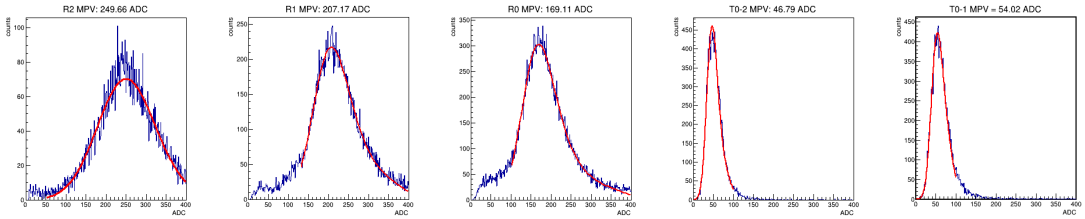

Figure 3.26: Landau fit example.

3.3.3 Studies of different SiPM models

Enubino was equipped first with the five FBK SiPMs. The two 25 μm SiPMs were connected to the two T0s, while the R2 channel mounted the 30 μm and the remaining two 20 μm SiPMs read the other two LCMs. The SiPMs were biased at 36 V, i.e. at 8 V of overvoltage, and the MIP peak was identified as explained in Sec. 3.3.2. The performances obtained on Enubino are shown in Fig. 3.27, blue line. As expected, the larger the cell size, the higher the signal. Dashed lines take into account the thickness of the scintillator crossed by a MIP in each channel: one tile for each t_0 and 5 tiles for the LCMs, thus a comparison can be made by scaling the t_0 signal of a factor 5. The signals from the t_0 tiles will have to be amplified during the ENUBET data acquisition, in order to get a signal of better quality. Figure 3.27 also show the comparison of the MIP signal collected with the AdvanSiD SiPMs. The purpose of this study is to compare the performances of Enubino to the Lateral prototype. Enubino was then equipped with five of the AdvanSiD SiPMs used during the 2018 test beam campaign, biased at 32 V (OV: 5 V), and the signals (yellow lines in Figure, there is again a correction factor due to the thickness of the t_0 tiles, dashed yellow line) were compared to the signals of channels of the Lateral calorimeter equipped with the same SiPMs used on Enubino (green line).

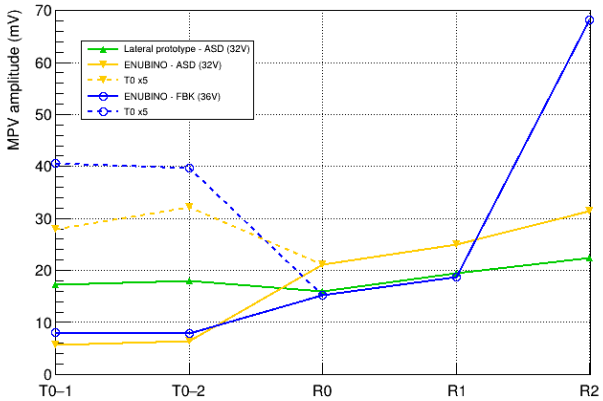

Figure 3.27: MPV of each channel of Enubino equipped with FBK (blue) and AdvanSiD SiPMs (yellow). Dashed lines take into account the thickness of the scintillator crossed by the MIPs. The MPV amplitudes of the lateral calorimeter are also shown for comparison (green).

Enubino performances are good and in particular, with equal SiPMs, the new structure of Enubino results in a slightly higher signal, demonstrating an improvement in the calorimeter design.

The available Hamamatsu SiPM was then tested on the T0-1 channel. A first overvoltage (OV) scan was performed and all the on-time signals are shown in Fig. 3.28. The most suitable bias was chosen by taking into account the distance of the MIP peak from the baseline. This was evaluated by fitting the baseline with a Gaussian and computing the distance as the difference between the MPV peak (from a Landau fit of the signal) and the baseline peak, in terms of numbers of baseline sigma. The results are reported in Tab. 3.2, the scan shows that the best separation of the signal from the baseline is achieved at 4 V of overvoltage.

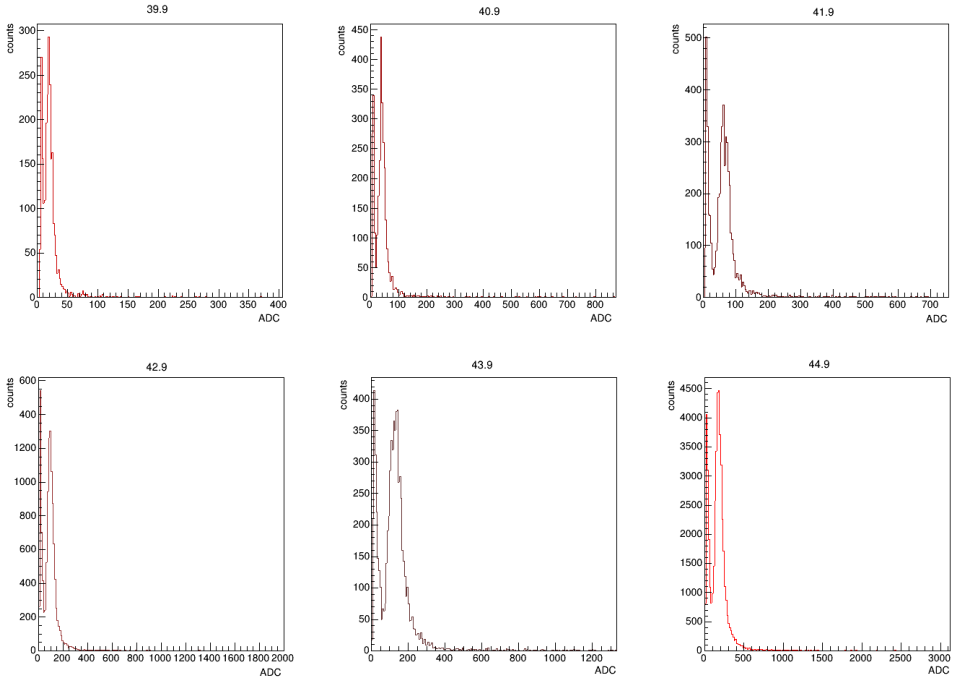

Figure 3.28: Overvoltage scan of the Hamamatsu SiPM.

V_{bias} (V)	OV (V)	Baseline - MPV distance (ADC)	distance / baseline sigma
39.9	2	9.8	7
40.9	3	25.8	9
41.9	4	50.2	19
42.9	5	65.0	6
43.9	6	89.1	8
44.9	5	121.9	6

Table 3.2: Overvoltage scan of the Hamamatsu SiPM.

The same spectra, cleaned of the baseline as described in Sec. 3.3.2, are shown in Fig. 3.29, and the MPV from the Landau fit of the spectra are summarized in Tab. 3.3.

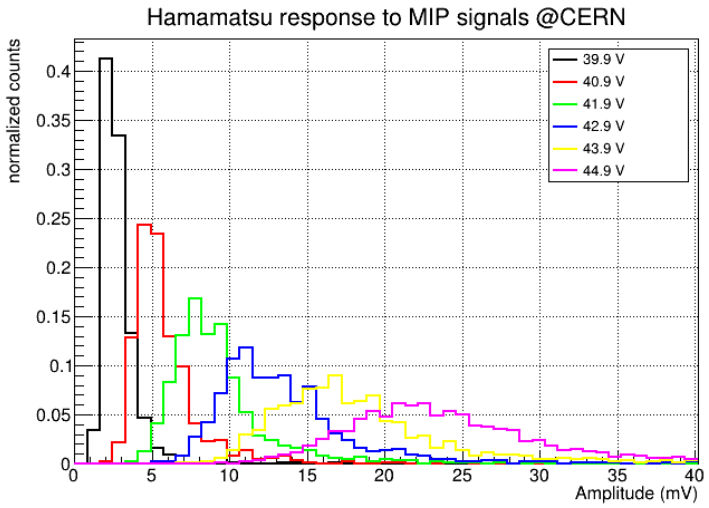

Figure 3.29: Spectra obtained with the Hamamatsu SiPM for different V_{bias}, obtained during the test beam.

V_{bias} (V)	MPV amplitude (mV)
39.9	2.24 ± 0.02
40.9	4.56 ± 0.05
41.9	7.38 ± 0.06
42.9	10.90 ± 0.1
43.9	14.9 ± 0.1
44.9	20.64 ± 0.05

Table 3.3: MPV amplitudes for the Hamamatsu SiPM at different V_{bias}, obtained during the test beam.

The SiPM was then moved to one of the LCM channels (in particular, on R1) and data were acquired to compare the performances with the other SiPMs. The amplitudes of the MIP peaks found as the MPV of the Landau fit of the signal distributions are shown in Fig. 3.30.

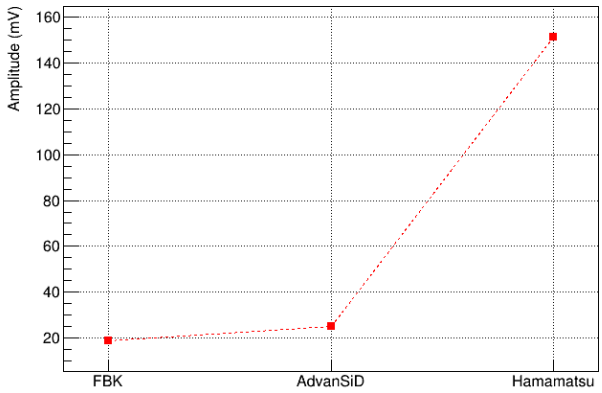

Figure 3.30: Amplitudes of MIP peaks on channel R1, for the FBK 20 μm, AdvanSiD and Hamamatsu SiPMs.

3.3.4 Efficiency study

The light collection efficiency of Enubino has been evaluated considering MIPs impacting the front face of the calorimeter or the t_0 tile and crossing the entire module (i.e. all the 5 scintillator tiles of the LCMs). First, the baseline was evaluated with a gaussian fit of the tracks not hitting the module, then a grid of 1×1 mm^2 was defined on the 3×3 cm^2 surface of the modules. The same study was repeated for vertical slices of 30×1 mm^2 and horizontal slices of 1×30 mm^2. The efficiency is then the ratio of two quantities:

- on-time signals with points of impact on the slices or grid, at 3 sigmas from baseline;
- all tracks with points of impact on the slices or grid.

Enubino satisfies the expectations: the maps of efficiency in Fig. 3.31 indicate high efficiency.

In the case of the horizontal slices, Fig. 3.32 shows the profile of channel R2, and Tab. 3.4 contains the efficiency values for the five Enubino channels.

Channel	Efficiency (%)
T0-1	97.4±0.1
T0-2	94.0±0.3
R0	98.2±0.3
R1	98.1±0.2
R2	98.0±0.1

Table 3.4: Efficiency of Enubino, horizontal slices. The evaluation of the efficiency has been performed taking into account the border effects (due to the alignment of the experimental apparatus), i.e. considering only the central part of the tile.

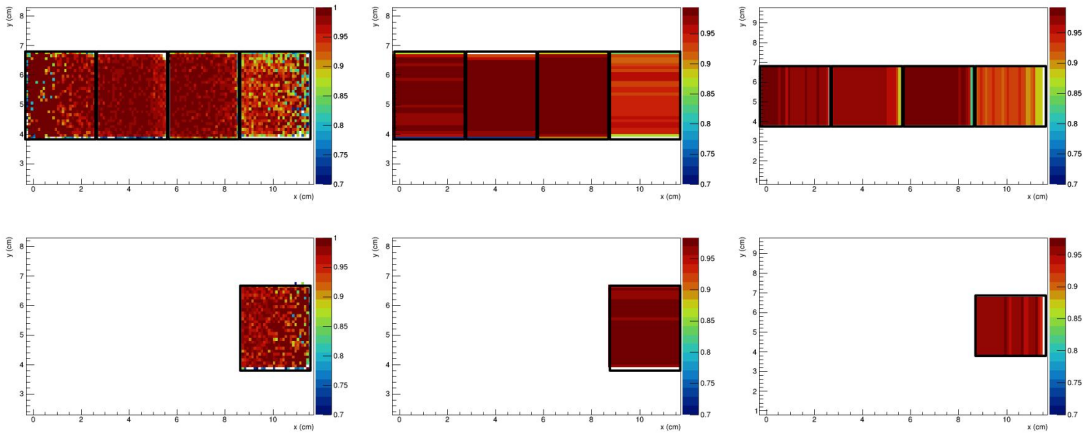

(a) 1×1 mm^2 grid (b) 1×30 mm^2 horizontal slices (c) 30×1 mm^2 vertical slices

Figure 3.31: Efficiency maps of Enubino. Data were taken with FBK SiPMs.

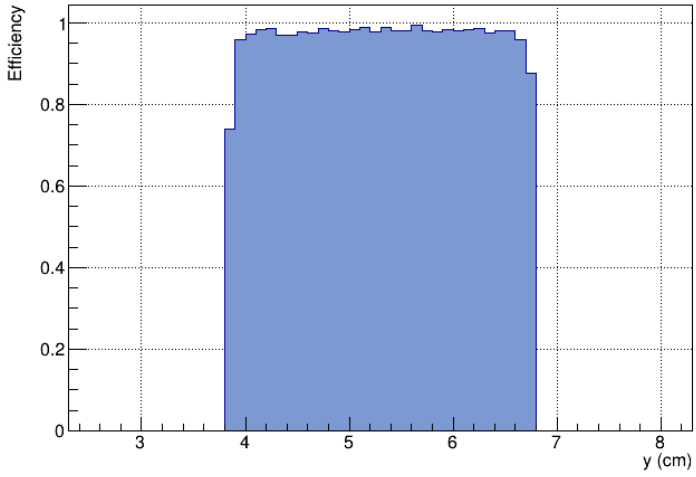

Figure 3.32: Efficiency of module R2. The efficiency of each module is constant along the tile surface.

3.3.5 Study of the uniformity of response

It is possible to evaluate the uniformity of response of Enubino using MIPs, in order to evaluate the impact of the new geometry. The uniformity is estimated, for each portion of the surface Enubino, by looking at the MIP MPV of the signals released in that portion, and displaying it on a 2D histogram. On-time MIP signals were selected, with a correction with the equalization factors: the differences in the SiPM response affect the amplitude of the MIP peak. The implementation of this step requires a Landau fit of the signal of each entire module, then the signals are scaled choosing one of the modules as reference. The impact regions of the particles on the front face of Enubino can be either the cells of a grid or horizontal/vertical slices. Thanks to the Silicon trackers, particles that cross almost perpendicularly the modules can be selected. This reduces the statistic available to perform the fit of the signal. However, a comparison between the uniformity estimated by selecting perpendicular tracks or tracks just crossing Enubino (Fig. 3.33) in the case of horizontal slices shows that the behaviour is about the same. Requiring that the particles exit from the back face of each module, crossing Enubino entirely, is then a sufficient condition. Some border effects due to the errors in the reconstruction of tracks are still visible in the three cases.

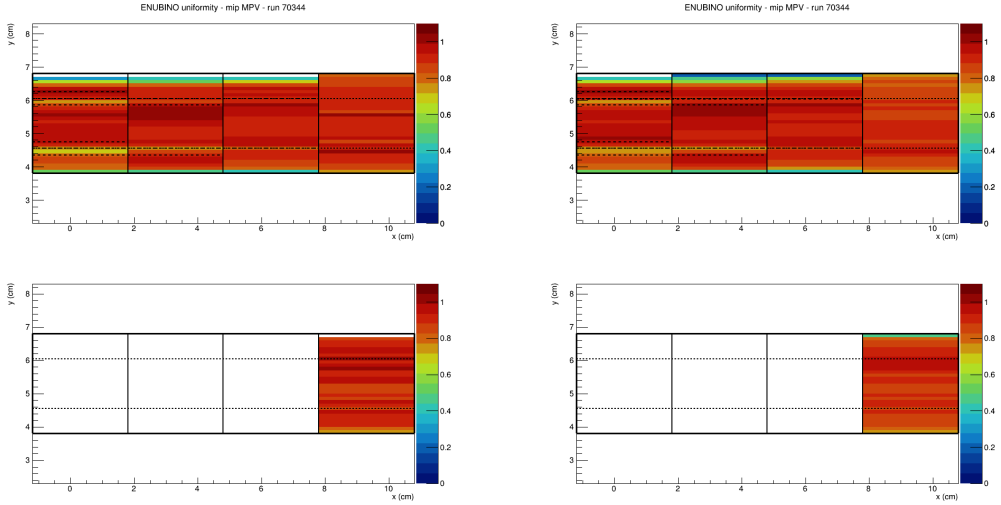

(a) Exit point on the entire 3×3 cm^2 back face

(b) Exit point on the corresponding slices on the back face

Figure 3.33: Uniformity of Enubino on 1×30 mm^2 horizontal slices.

An example of a Landau fit in the cells of a grid is shown in Fig. 3.34. It is a coarser grid than the one defined for the efficiency study, in order to have more statistics for fitting the signal.

The horizontal slices have a height of 1 mm, which is equal to the fiber diameter. Dashed lines in Fig. 3.33 show their position across the modules of Enubino. In this case, there is a slight disuniformity on the R2 module at the level of the position of the fibers. R2 is the outer module

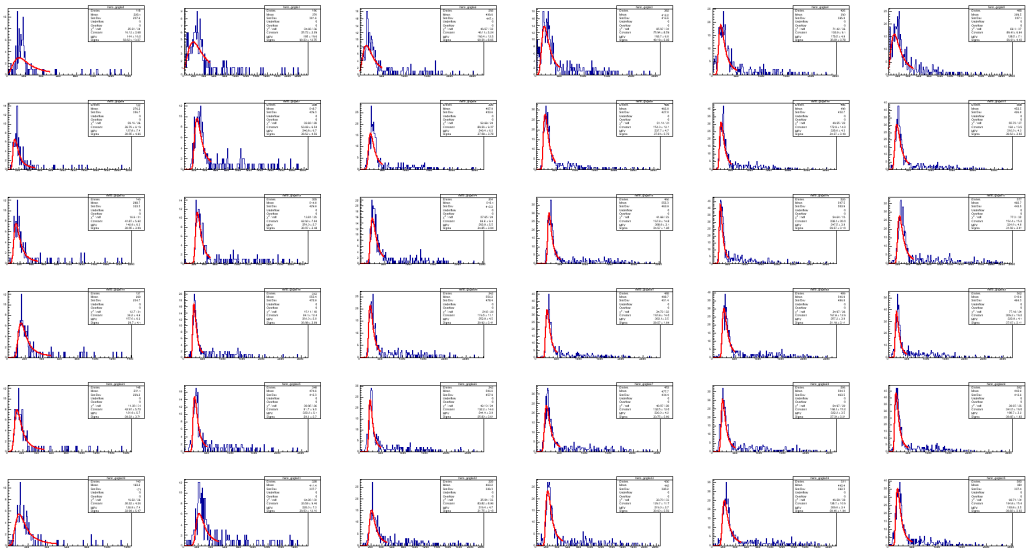

Figure 3.34: Landau fit of MIP signals in a 5×5 mm^2 grid.

before the fibres are extracted, thus it is the module that is crossed by the larges numbers of fibers. This means that the thickness of the scintillator is thinner in that region, and this implies a smaller distance travelled by MIPs, thus a lower energy deposition. This can be seen also in the residual plot in Fig. 3.35, where the percentage difference of the signal in each slice, with respect to the average of every single signals, is shown. There is a valley corresponding to the position of the fibers, that gets more evident getting to the R2 module.

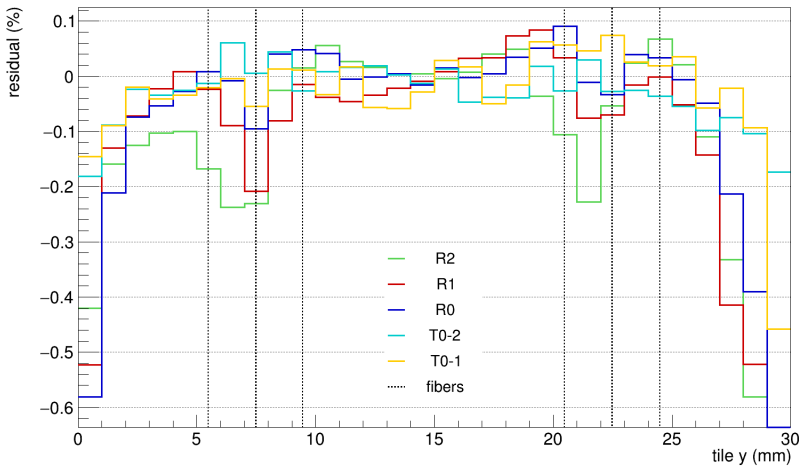

Figure 3.35: Residual plot of the signals in the vertical slices, for each channel of Enubino. The position of the fibers is plotted in dashed lines.

The situation is different if we average this effect by considering the vertical slices and the grid. Fig. 3.36 shows the uniformity in these cases. The prototype behaves according to expectations with good uniformity.

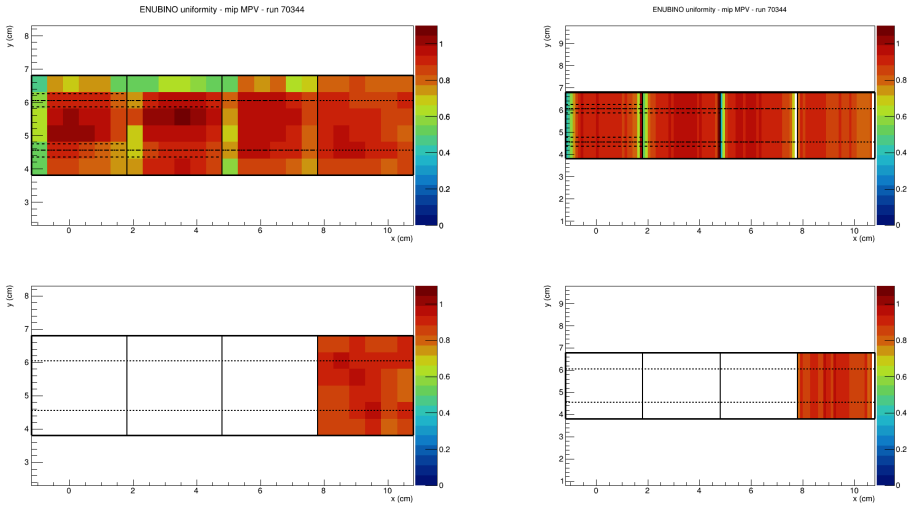

(a) 5×5 mm^2 grid

(b) 30×1 mm^2 vertical slices

Figure 3.36: Uniformity of Enubino on grid/vertical slices.

3.3.6 Optical crosstalk

It is essential that the new light readout scheme employed in Enubino, and that will be employed later by the Demonstrator, is safe in terms of channel crosstalk. Optical crosstalk occurs when light produced in the scintillator belonging module travels to a neighbouring on, and might then be picked up by one of its readout fibers. This would generate a signal in the wrong module, affecting the reconstructing performances of the modular calorimeter. There are three contributions to the optical crosstalk that can be identified in Enubino, due to its geometry: a "direct" contribution and two "indirect" ones.

The direct crosstalk ("DC", or crosstalk of "type I") is due to the lateral surface of the scintillator tiles being in contact between modules. Scintillation light can travel from one module to another if the surfaces are not completely opaque, due to imperfections in the TiO_2 layer of paint. Two additional kinds of indirect crosstalk are possible:

- leak of light from fibers to modules which are passed through ("type II"). This results in a signal in the neighbouring module on the side of the fiber extraction;
- collection of light from transit grooves to fibers ("type III") In this case, the light enters the fiber belonging to the module on the side opposite to the fiber extraction.

Crosstalk of type I should be suppressed with respect to the other two sources, due to the Enubino structure. One of the difficulties in the Enubino construction was indeed the painting of the

grooves (for a close-up see Fig. 3.14 in Sec. 3.2). As an example, a scheme of how the three crosstalk types act on the R0 module is shown in Fig. 3.37.

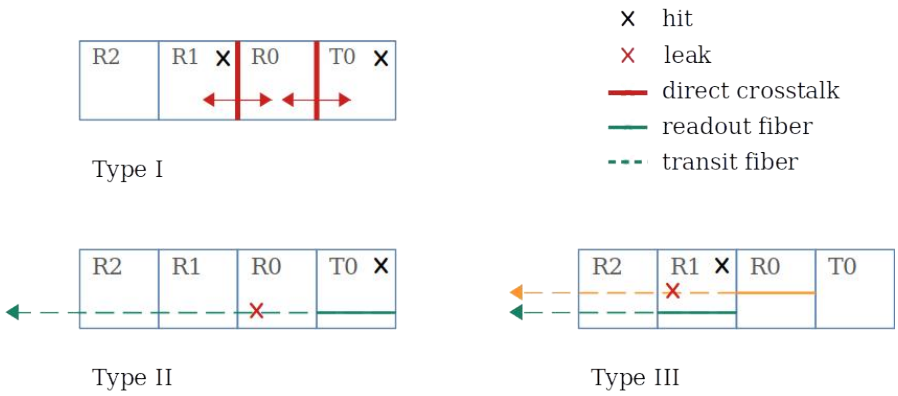

Figure 3.37: The three types of crosstalk on R0: the direct crosstalk (top left) and the indirect type I (bottom, left) and II (bottom, right).

In practice, one looks at what the modules of Enubino see when one of them is hit by a particle (Fig. 3.38). A qualitative study comes from the comparison of the channel signals, with their respective baselines, and the crosstalk caused by the other channels. The baselines were estimated by looking at the signals recorded by the Enubino channels when the reconstructed tracks do not hit Enubino (in particular, only tracks missing Enubino by 2 cm on each side were selected). Signals (both real and crosstalk ones) and baselines were scaled arbitrarily since what really matters are the peak amplitudes.

Crosstalk of type III is the dominant source: the highest crosstalk signals appear to be caused by R2 and R1 on the channels right to their right (with fibers collected on the left, see as reference Fig. 3.21). This means that the scintillation light went from the transit grooves to the wrong fibers, and was then recorded as a signal on the tiles on the right side. On most of the channels, the crosstalk signals are almost completely overlapped with the baseline. These signals then cannot be considered crosstalk. At this level, the crosstalk is not challenging for the calorimeter, since its purpose is not precise shower profiling. It would not affect the reconstruction capabilities, but would only contribute to the amount of energy reconstructed in a module. The t_0 case can not be evaluated, since the t_0s were not amplified during the test beam, and their reconstructed signals partially overlap with their baselines.

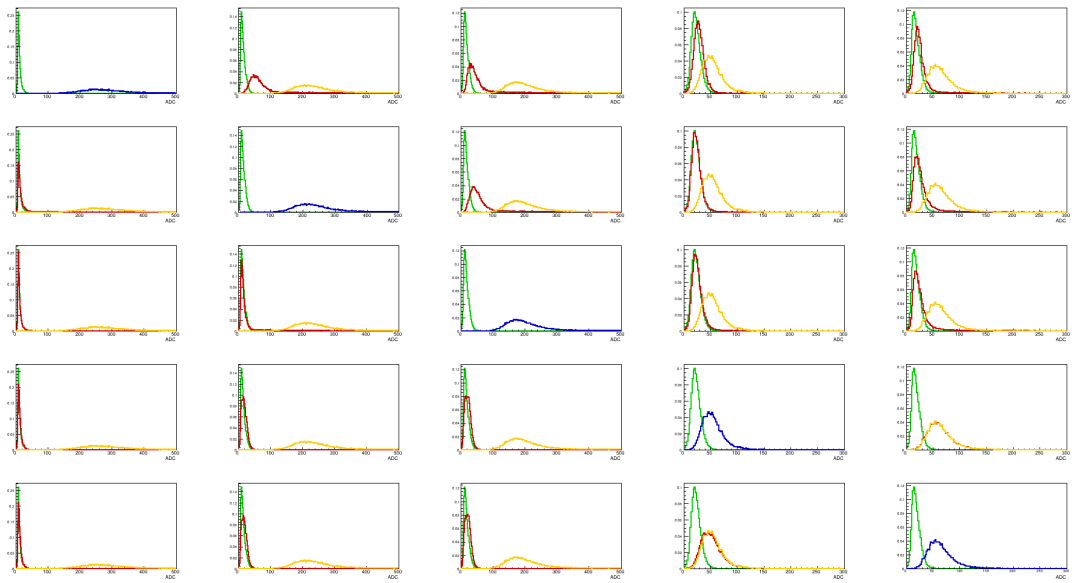

Figure 3.38: Optical crosstalk between the channels of Enubino. Blue histograms (in diagonal plots): signal on each channel. Following the sequence: R2, R1, R0, T0-2, T0-1: rows represent the crosstalk *caused* by each module, while columns represent the crosstalk *on* each module. Crosstalk signals are shown in red. Yellow histograms on the off-diagonal plots show the signal of that particular module, with their baselines (in green). For instance, column 1 contains, from up to down: the signal on R2 in blue (with its baseline in green), the crosstalk on R2 from R1 (red) with the signal (yellow) of R2 and its baseline (green), the crosstalk on R2 from R0 (red) with the signal (yellow) of R2 and its baseline (green), the crosstalk on R2 from T0-2, and the crosstalk on R2 from T0-1. Row 1 contains instead, from left to right, the signal on R2 and the crosstalk (red) caused by R2 on R1 (yellow), R0, T0-2, T0-1. Each t_0 tile gives a 100% crosstalk on the other since they are placed one downstream the other: any reconstructed particle crossing T0-2 necessarily crosses also T0-1, producing two correlated signals.

3.4 Future perspectives: the Demonstrator

Enubino can be considered as a pre-demonstrator. The new light reading scheme that uses frontal grooves instead of lateral grooves, which was motivated by the need for large-scale production of the scintillators, has been successfully tested thanks to Enubino. It ensures good uniformity and high efficiency of light collection. The Hamamatsu S14160-3050HS (with a smaller 3×3 mm^2 area, for the t_0 layer) and S14160-4050HS (4×4 mm^2. for the LCMs) SiPMs were chosen to instrument the demonstrator (Fig. 3.44). This choice was driven by the commercial availability of these models. Some of the properties of the calorimeter (e.g. the optical crosstalk) were not tested on Enubino since only one of these SiPMs was available during the test beam, however, the data acquired during the test beam demonstrate good performances (see Sec. 3.3.3) and good baseline-signal separation.

The demonstrator will be a section of the ENUBET instrumented decay tunnel. This prototype will be 1.65 m long in the z direction, which corresponds to 15 LCMs, and it will be composed of arches of iron or plastic scintillators spanning 90°. This modular design could be extended then to a full 2π object. The demonstrator is composed of three LCMs in the radial direction, plus a 30 cm thick BPE layer (the neutron shield). Only the central 45°part can be instrumented, for mechanical considerations, but the current availability of materials (in particular, the scintillator tiles) requires a restriction to 8 LCMs along the arches. The total weight of the prototype (mechanical support, calorimeter and t_0 layer, BPE) is $\sim$3.2 t.

A schematic view of the demonstrator is shown in Fig. 3.39a, while Fig. 3.39b shows one complete arch: three radial layers of LCMs with integrated photon veto, and fiber routing through the BPE.

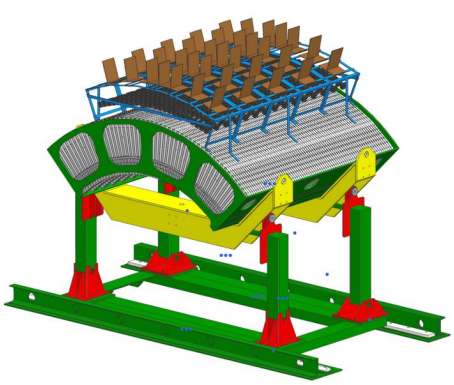

(a) 3D rendering of the demonstrator.

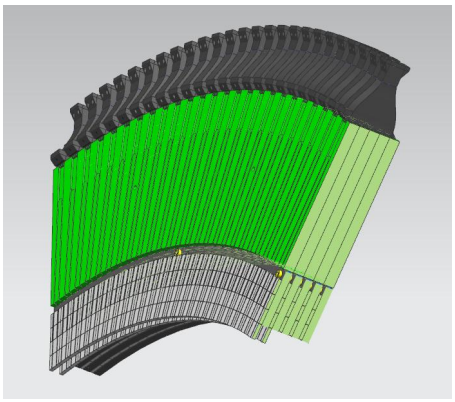

(b) A section of the demonstrator corresponding to the instrumentation of one arch (for a depth of one LCM).

Figure 3.39: Demonstrator design.

The demonstrator will be housed in a custom structure (Fig. 3.40a) with four extendable legs for calorimeter tilting (in order to simulate the impact angle of the positrons inside the ENUBET decay tunnel), and it will be composed of 75 Iron planes 1.5 cm thick, 11 cm long, alternated

with 75 scintillator planes. Above them, the BPE arches (2.25 cm thick, 30 cm long) will be placed (Fig. 3.40b). The Iron components will be made of single slabs, that have been milled in their central part in order to better accommodate the painted scintillator tiles (Fig. 3.40c).

(a) Demonstrator cradle

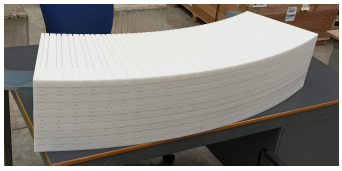

(b) Borated Polyethylene arches

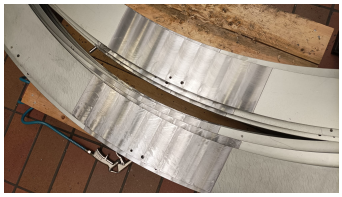

(c) Iron inner arches

Figure 3.40: Assembly of the demonstrator at INFN-LNL.

Scintillator tiles (Fig. 3.41) 0.7 cm thick from STYLPLEX have a trapezoidal shape in order to avoid dead regions. The grooves on each tile have a square shape. 5000 meters of Kuraray Y11 WLS fiber are available. It has been cut in segments 50-60 cm long for proper routing. Tiles are smoothed with sandpaper, for better adhesion of the paint coating, and then fibers are glued to them. The risk of obstructing the grooves with the TiO_2 coating has been reduced by painting the tiles with two layers of the TiO_2-based paint watered down. An additional layer of Aluminum-based paint will be added to the grooves for safer optical isolation.

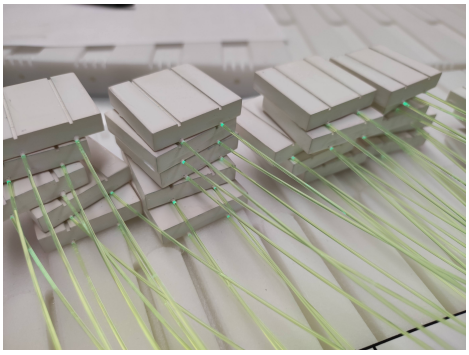

(a) Painted tiles for the demonstrator

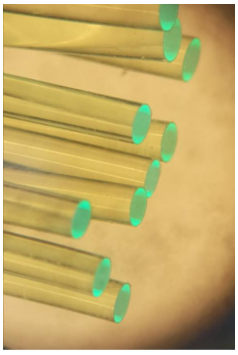

(b) Polished fibers

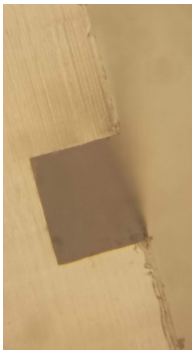

(c) Groove close-up

Figure 3.41: Demonstrator tiles.

Tiles are assembled according to the triplet/quadruplet scheme, over each Iron layer, as in Fig. 3.42.

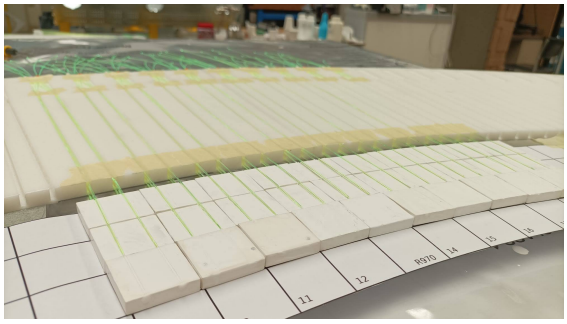

(a) A plane of triplets

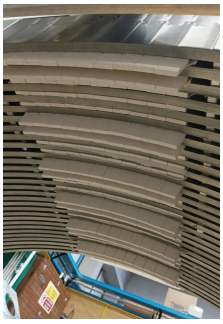

(b) t_0 tiles as the inner layer

Figure 3.42: Construction of the demonstrator.

Correct bundling is ensured by a fiber routing cap, the "concentrator", at the end of the neutron shield, which was appositely designed and 3D printed for the ENUBET demonstrator (Fig. 3.43). The fibers are glued into place and then levelled for a good fiber to SiPM coupling. The demonstrator will be readout by 600 channels: 360 LCMs and 240 t_0 tiles. Hamamatsu SiPMs will be hosted on custom PCBs (Fig. 3.44) that will be fixed to the top of each fiber concentrator.

(a) First planes built

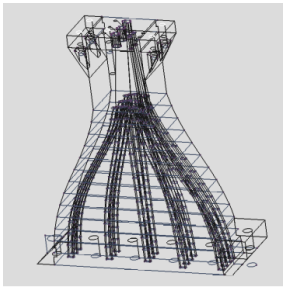

(b) Concentrator design

Figure 3.43: Fiber routing.

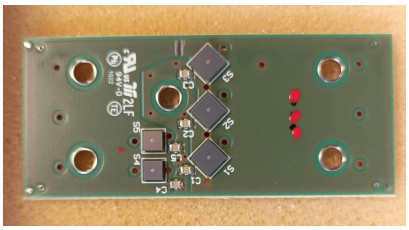

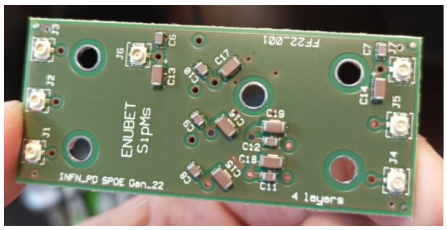

Figure 3.44: SiPMs soldered on a PCB hosting three calorimetric LCMs and a t_0 doublet.

At the time of writing, the assembly of the demonstrator has been completed at the INFN-LNL, and it has been successfully sent to CERN for the final test with a charged particle beam at the PS East Area.

Figure 3.45: The assembled demonstrator.

Conclusions

During my PhD work, I focused on the simulation of the beamline for ENUBET in order to have the desired secondary hadronic beam that leads to a muon/electron neutrino beam. A quantitative analysis and design of such a beamline cannot just rely on a pure optical simulation and must instead be put through a number of thorough, generally complex simulations of particle tracking and interaction. The most crucial beamline components have undergone extensive adjustments and tuning procedures. I participated in the optimization of the beamline parameters, such as the dimensions and apertures of the collimators. The background transported by the beamline was carefully taken into account in this procedure, having as a figure of merit the kaons decaying into the detector over all the other hadronic activity, leading to an improvement in the signal-to-noise ratio in the decay tunnel.

I exploited cluster resources in order to run efficiently the simulations of the beamline, and I worked on optimizing the simulation time performance by applying suitable cuts on the simulation parameters and verifying their impact on the results. Thanks to these studies, I produced the first results with the GEANT4 software on the ENUBET beamline performances, which lead to the finalization of the beamline that will be used for the future realization of ENUBET. The beamline framework is extremely flexible: the code has been automatized and scripted to a level in which, when something has to be modified, the entire beamline can be quickly re-adjusted to an optimal configuration. Moreover, it allows accessing the particles decay information and their history through the beamline volumes. The development of the simulation of the ENUBET facility is of the utmost importance since such a tool can be exploited in various contexts, from the assessment of the particle discrimination capabilities of the ENUBET tagger to the studies on the reduction of the systematic budget, which is the ENUBET primary goal. The fit of the lepton observables performed thanks to the beamline inputs allows reducing to the $\sim 1\%$ level the hadro-production systematics on the neutrino flux [97].

In addition, I have worked on the hardware R&D for ENUBET. I assembled Enubino, the prototype that contains the finalized calorimeter technology for the ENUBET instrumented tagger. Enubino consists of a modular sampling calorimeter made of iron and plastic scintillator. Each module is read out by a Silicon PhotoMultiplier (SiPM), which is coupled to a specific light readout technique, based on a novel method of connecting WLS fibres to the scintillator tiles. I prepared, coated, and assembled the final detector at the Legnaro INFN National Laboratories, where I also took part in the characterisation of Enubino with cosmic rays and the testing of several SiPM models. Then I participated in the test of Enubino on a charged particle beam and analyzed data from this test beam, assessing the performance of the readout system of the

calorimeter. I have been in charge of the test beam data analysis, which includes the intercalibration of the different modules of the calorimeter, the measurement of the efficiency, and the characterization of the response to charged particles. Enubino has an efficiency of $\sim 96\%$, it presents a good uniformity of response to MIPs, and the optical crosstalk is under control. I participated in the realization of the Demonstrator, assembling, this final prototype thanks to the knowledge of Enubino, and I will participate in the test beam in October 2022. The ultimate test beam of the demonstrator will corroborate the performance of ENUBET and be a milestone in the future development of monitored decay tunnels for current and future experiments.

Thanks to the finalization of the simulation work and the detector technology it will now be possible to propose the construction of ENUBET and perform more accurate studies on the usage of such a facility for neutrino flux systematics reduction.

The project has been validated by simulations and experimental tests, demonstrating the potential of the ENUBET technology. The outcome of the studies is convincing and no showstoppers have been identified in the monitored neutrino beam concept. An optimal opportunity for this kind of experiment would be the possibility to begin data collection in 2029, during LHC Run IV and concurrently with the DUNE/Hyper-Kamiokande data taking. The Collaboration has started working on an actual implementation at CERN with the aim is to submit a technical proposal by 2024/25.

Bibliography

[1] Raymond Davis, Don S. Harmer, and Kenneth C. Hoffman. Search for neutrinos from the sun. *Phys. Rev. Lett.*, 20:1205–1209, May 1968.

[2] John N. Bahcall. Solar neutrinos. i. theoretical. *Phys. Rev. Lett.*, 12:300–302, Mar 1964.

[3] John N. Bahcall and Raymond Davis. Solar neutrinos: A scientific puzzle. *Science*, 191(4224):264–267, 1976.

[4] Y. Fukuda et al. Evidence for oscillation of atmospheric neutrinos. *Phys. Rev. Lett.*, 81:1562–1567, 1998.

[5] A. B. McDonald et al. Measurement of CC interactions produced by ^{8}B solar neutrinos at SNO. *PoS*, hep2001:186, 2001.

[6] Carlo Giunti and Chung W. Kim. *Fundamentals of Neutrino Physics and Astrophysics*. Oxford Univ., Oxford, 2007.

[7] R. L. Workman and Others. Review of Particle Physics. *PTEP*, 2022:083C01, 2022.

[8] Ivan Esteban, M.C. Gonzalez-Garcia, Michele Maltoni, Thomas Schwetz-Mangold, and Albert Zhou. The fate of hints: updated global analysis of three-flavor neutrino oscillations. *Journal of High Energy Physics*, 2020, 09 2020.

[9] NuFIT 5.1 (2021). www.nu-fit.org. Accessed: 2022-06-15.

[10] J. A. Formaggio and G. P. Zeller. From eV to EeV: Neutrino Cross Sections Across Energy Scales. *Rev. Mod. Phys.*, 84:1307–1341, 2012.

[11] N. Aghanim et al. Planck 2018 results. VI. Cosmological parameters. *Astron. Astrophys.*, 641:A6, 2020. [Erratum: Astron.Astrophys. 652, C4 (2021)].

[12] E. Komatsu, K. M. Smith, J. Dunkley, C. L. Bennett, B. Gold, G. Hinshaw, N. Jarosik, D. Larson, M. R. Nolta, L. Page, D. N. Spergel, M. Halpern, R. S. Hill, A. Kogut, M. Limon, S. S. Meyer, N. Odegard, G. S. Tucker, J. L. Weiland, E. Wollack, and E. L. Wright. Seven-year Wilkinson Microwave Anisotropy Probe (WMAP) Observations: Cosmological Interpretation. *Astrophys. J. Suppl.*, 192(2):18, February 2011.

[13] M. Aker et al. Direct neutrino-mass measurement with sub-electronvolt sensitivity. *Nature Phys.*, 18(2):160–166, 2022.

[14] L. Gastaldo et al. The Electron Capture ^{163}Ho Experiment ECHo: an overview. *J. Low Temp. Phys.*, 176(5-6):876–884, 2014.

[15] B. Alpert et al. HOLMES - The Electron Capture Decay of ^{163}Ho to Measure the Electron Neutrino Mass with sub-eV sensitivity. *Eur. Phys. J. C*, 75(3):112, 2015.

[16] M. P. Croce et al. Development of holmium-163 electron-capture spectroscopy with transition-edge sensors. *J. Low Temp. Phys.*, 184(3-4):958–968, 2016.

[17] S. H. Ahn et al. Detection of accelerator produced neutrinos at a distance of 250 km. *Phys. Lett. B*, 511:178–184, 2001.

[18] E. Ables et al. P-875: A Long baseline neutrino oscillation experiment at Fermilab. Technical report, FERMILAB, 2 1995.

[19] K. Abe et al. The T2K Experiment. *Nucl. Instrum. Meth. A*, 659:106–135, 2011.

[20] D. S. Ayres et al. NOvA: Proposal to Build a 30 Kiloton Off-Axis Detector to Study $\nu_\mu \to \nu_e$ Oscillations in the NuMI Beamline. Technical report, FERMILAB, 3 2004.

[21] Hyper-Kamiokande Collaboration. Hyper-Kamiokande Design Report. Technical report, KEK, 2 2016.

[22] James Strait et al. Long-Baseline Neutrino Facility (LBNF) and Deep Underground Neutrino Experiment (DUNE): Conceptual Design Report, Volume 3: Long-Baseline Neutrino Facility for DUNE June 24, 2015. Technical report, FERMILAB, 1 2016.

[23] M. H. Ahn et al. Measurement of Neutrino Oscillation by the K2K Experiment. *Phys. Rev. D*, 74:072003, 2006.

[24] S. Yamamoto et al. An Improved search for $\nu_\mu \to \nu_e$ oscillation in a long-baseline accelerator experiment. *Phys. Rev. Lett.*, 96:181801, 2006.

[25] P. Adamson et al. Measurement of Neutrino and Antineutrino Oscillations Using Beam and Atmospheric Data in MINOS. *Phys. Rev. Lett.*, 110(25):251801, 2013.

[26] M. A. Acero et al. New constraints on oscillation parameters from ν_e appearance and ν_μ disappearance in the NOvA experiment. *Phys. Rev. D*, 98:032012, 2018.

[27] P. Adamson et al. First measurement of muon-neutrino disappearance in NOvA. *Phys. Rev. D*, 93(5):051104, 2016.

[28] K. Abe et al. Indication of Electron Neutrino Appearance from an Accelerator-produced Off-axis Muon Neutrino Beam. *Phys. Rev. Lett.*, 107:041801, 2011.

[29] K. Abe et al. Observation of Electron Neutrino Appearance in a Muon Neutrino Beam. *Phys. Rev. Lett.*, 112:061802, 2014.

[30] K. Abe et al. Precise Measurement of the Neutrino Mixing Parameter θ_{23} from Muon Neutrino Disappearance in an Off-Axis Beam. *Phys. Rev. Lett.*, 112(18):181801, 2014.

[31] K. Abe et al. Constraint on the matter–antimatter symmetry-violating phase in neutrino oscillations. *Nature*, 580(7803):339–344, 2020. [Erratum: Nature 583, E16 (2020)].

[32] N. Abgrall et al. Measurements of $\pi^{\pm}$ differential yields from the surface of the T2K replica target for incoming 31 GeV/c protons with the NA61/SHINE spectrometer at the CERN SPS. *Eur. Phys. J. C*, 76(11):617, 2016.

[33] K. Abe et al. Improved constraints on neutrino mixing from the T2K experiment with $\mathbf{3.13 \times 10^{21}}$ protons on target. *Phys. Rev. D*, 103(11):112008, 2021.

[34] Sacha E. Kopp. Accelerator-based neutrino beams. *Phys. Rept.*, 439:101–159, 2007.

[35] Alessandro Strumia and Francesco Vissani. Neutrino masses and mixings and..., 2006.

[36] B. Aharmim et al. Determination of the ν_e and total ^{8}B solar neutrino fluxes with the Sudbury neutrino observatory phase I data set. *Phys. Rev. C*, 75:045502, 2007.

[37] K. Eguchi et al. First results from KamLAND: Evidence for reactor anti-neutrino disappearance. *Phys. Rev. Lett.*, 90:021802, 2003.

[38] M. Apollonio et al. Limits on neutrino oscillations from the CHOOZ experiment. *Phys. Lett. B*, 466:415–430, 1999.

[39] G. Bellini et al. Measurement of the solar ^{8}B neutrino rate with a liquid scintillator target and 3 MeV energy threshold in the Borexino detector. *Phys. Rev. D*, 82:033006, 2010.

[40] B. Armbruster et al. Upper limits for neutrino oscillations $\overline{\nu}_\mu \to \overline{\nu}_e$ from muon decay at rest. *Phys. Rev. D*, 65:112001, 2002.

[41] A. Aguilar-Arevalo et al. Evidence for neutrino oscillations from the observation of $\bar{\nu}_e$ appearance in a $\bar{\nu}_\mu$ beam. *Phys. Rev. D*, 64:112007, 2001.

[42] A. A. Aguilar-Arevalo et al. A Search for Electron Neutrino Appearance at the $\Delta m^2 \sim 1\ \mathrm{eV}^2$ Scale. *Phys. Rev. Lett.*, 98:231801, 2007.

[43] G. P. Zeller et al. A Precise Determination of Electroweak Parameters in Neutrino Nucleon Scattering. *Phys. Rev. Lett.*, 88:091802, 2002. [Erratum: Phys.Rev.Lett. 90, 239902 (2003)].

[44] P. Adamson et al. A Study of Muon Neutrino Disappearance Using the Fermilab Main Injector Neutrino Beam. *Phys. Rev. D*, 77:072002, 2008.

[45] M. Holder et al. A Detector for High-Energy Neutrino Interactions. *Nucl. Instrum. Meth.*, 148:235, 1978.

[46] A. N. Diddens et al. A Detector for Neutral Current Interactions of High-energy Neutrinos. *Nucl. Instrum. Meth.*, 178:27, 1980.

[47] C. Rubbia. The Liquid Argon Time Projection Chamber: A New Concept for Neutrino Detectors. Technical report, CERN, 5 1977.

[48] B. Abi et al. The Single-Phase ProtoDUNE Technical Design Report. Technical report, FERMILAB, 6 2017.

[49] A. Longhin, L. Ludovici, and F. Terranova. A novel technique for the measurement of the electron neutrino cross section. *Eur. Phys. J. C*, 75(4):155, 2015.

[50] A Berra et al. Enabling precise measurements of flux in accelerator neutrino beams: the ENUBET project. Technical report, CERN, Geneva, Oct 2016.

[51] F Acerbi et al. The ENUBET project. Technical report, CERN, Geneva, Oct 2018.

[52] A Longhin and F Terranova. NP06/ENUBET annual report for the CERN-SPSC. Technical report, CERN, Geneva, Mar 2020.

[53] F Acerbi et al. NP06/ENUBET Annual Report for the SPSC (2021). Technical report, CERN, Geneva, Apr 2021.

[54] F Acerbi et al. NP06/ENUBET annual report 2022 for the SPSC. Technical report, CERN, Geneva, Apr 2022.

[55] Fabio Pupilli et al. Positron identification in the ENUBET instrumented decay tunnel. *PoS*, NEUTEL2017(307):078, 2018.

[56] Fabio Pupilli et al. Lepton reconstruction in the ENUBET tagger. *PoS*, NuFact2021:025, 2022.

[57] Evegnii Lutsenko. *Advanced signal processing within the ENUBET project*. PhD thesis, Insubria U., Como, 2021. To be published.

[58] Andreas Hocker et al. TMVA - Toolkit for Multivariate Data Analysis. Technical report, CERN, 3 2007.

[59] Antonio Branca et al. Fluxes and systematics reduction with decay monitoring. *PoS*, NuFact2021:030, 2022.

[60] Elisabetta G. Parozzi, Giulia Brunetti, Nikolaos Charitonidis, Andrea Longhin, Michelangelo Pari, Fabio Pupilli, and Francesco Terranova. The ENUBET Multi Momentum Secondary Beamline Design. *JACoW*, IPAC 2021:3053–3056, 2021.

[61] Antonio Branca, Giulia Brunetti, Andrea Longhin, Marco Martini, Fabio Pupilli, and Francesco Terranova. A New Generation of Neutrino Cross Section Experiments: Challenges and Opportunities. *Symmetry*, 13(9):1625, 2021.

[62] Michelangelo Pari, Matthew Fraser, Brennan Goddard, Verena Kain, Linda Stoel, and Francesco Velotti. Model and measurements of CERN-SPS slow extraction spill re-shaping - the burst mode slow extraction. In *10th International Particle Accelerator Conference*, page WEPMP035, 2019.

[63] Michelangelo Pari. *Study and development of SPS slow extraction schemes and focusing of secondary particles for the ENUBET monitored neutrino beam*. PhD thesis, U. Padua, Dept. Phys. Astron., 11 2020.

[64] Karl L Brown, David C Carey, F Christoph Iselin, and F Rothacker. *TRANSPORT: a computer program for designing charged-particle beam-transport systems*. CERN Yellow Reports: Monographs. CERN, Geneva, 1980. Also publ. as SLAC and FERMILAB.

[65] T. J. Roberts, K. B. Beard, Dazhang Huang, S. Ahmed, D. M. Kaplan, and L. K. Spentzouris. G4Beamline Particle Tracking in Matter-dominated Beam Lines. *Conf. Proc. C*, 0806233:WEPP120, 2008.

[66] S. Agostinelli et al. GEANT4–a simulation toolkit. *Nucl. Instrum. Meth. A*, 506:250–303, 2003.

[67] John Allison et al. Geant4 developments and applications. *IEEE Trans. Nucl. Sci.*, 53:270, 2006.

[68] J. Allison et al. Recent developments in Geant4. *Nucl. Instrum. Meth. A*, 835:186–225, 2016.

[69] T. T. Böhlen, F. Cerutti, M. P. W. Chin, A. Fassò, A. Ferrari, P. G. Ortega, A. Mairani, P. R. Sala, G. Smirnov, and V. Vlachoudis. The FLUKA Code: Developments and Challenges for High Energy and Medical Applications. *Nucl. Data Sheets*, 120:211–214, 2014.

[70] Alfredo Ferrari, Paola R. Sala, Alberto Fasso, and Johannes Ranft. FLUKA: A multi-particle transport code, 10 2005.

[71] Nikolai Mokhov. Mars15, version 00, 7 2016.

[72] Hugo W. Bertini. Low-Energy Intranuclear Cascade Calculation. *Phys. Rev.*, 131:1801–1821, 1963.

[73] Bo Andersson, G. Gustafson, and Hong Pi. The FRITIOF model for very high-energy hadronic collisions. *Z. Phys. C*, 57:485–494, 1993.

[74] D.H. Wright and M.H. Kelsey. The geant4 bertini cascade. *Nuclear Instruments and Methods in Physics Research Section A: Accelerators, Spectrometers, Detectors and Associated Equipment*, 804:175–188, 2015.

[75] V. Uzhinsky. Tuning of the GEANT4 FRITIOF (FTF) Model Using NA61/SHINE Experimental Data. 9 2011.

[76] Centre de Calcule de l'IN2P3. Lyon, France. `https://cc.in2p3.fr`.

[77] B. D. Muratori, J. K. Jones, and A. Wolski. Analytical expressions for fringe fields in multipole magnets. *Phys. Rev. ST Accel. Beams*, 18(6):064001, 2015.

[78] User's guide: For application developers. https://geant4.web.cern.ch/support/user_documentation.

[79] G. Ballerini et al. Testbeam performance of a shashlik calorimeter with fine-grained longitudinal segmentation. *JINST*, 13(01):P01028, 2018.

[80] F. Acerbi et al. Irradiation and performance of RGB-HD Silicon Photomultipliers for calorimetric applications. *JINST*, 14(02):P02029, 2019.

[81] F. Acerbi et al. Polysiloxane-based scintillators for shashlik calorimeters. *Nucl. Instrum. Meth. A*, 956:163379, 2020.

[82] F. Acerbi et al. The ENUBET positron tagger prototype: construction and testbeam performance. *JINST*, 15(08):P08001, 2020.

[83] Claudio Piemonte. A new silicon photomultiplier structure for blue light detection. *Nuclear Instruments and Methods in Physics Research Section A: Accelerators, Spectrometers, Detectors and Associated Equipment*, 568:224–232, 11 2006.

[84] A. Berra et al. Shashlik calorimeters with embedded SiPMs for longitudinal segmentation. *IEEE Trans. Nucl. Sci.*, 64(4):1056–1061, 2017.

[85] H. Fessler, P. Freund, J. Gebauer, J.M. Glas, K.P. Pretzl, P. Seyboth, J. Seyerlein, and J.C. Thevenin. A tower structured scintillator-lead photon calorimeter using a novel fiber optics readout system. *Nuclear Instruments and Methods in Physics Research Section A: Accelerators, Spectrometers, Detectors and Associated Equipment*, 228(2):303–308, 1985.

[86] ELJEN Technology, 1300 W. Broadway, Sweetwater, TX 79556, USA.

[87] Saint-Gobain Group, Courbevoie, France.

[88] Fondazione Bruno Kessler, Trento, Italy.

[89] Advansid s.r.t., Via Sommarive 18, I-38123, Povo, Trento, Italy.

[90] Hamamatsu Photonics K.K., 325-6, Sunayama-cho, Naka-ku, Hamamatsu City, Shizuoka, 430-8587, Japan.

[91] KURARAY CO., LTD., Ote Center Building, 1-1-3, Otemachi, Chiyodaku, Tokyo 100-8115, Japan.

[92] Optical cement EJ-500. https://eljentechnology.com/products/accessories/ej-500.

[93] Reflective paint EJ-520. http://www.ggg-tech.co.jp/maker/eljen/ej-520.html.

[94] PS East Area documentation, http://sba.web.cern.ch/sba/BeamsAndAreas/East/East.htm.

[95] CAEN S.p.A. Via Vetraia, 11, 55049, Viareggio, Lucca, Italy.

[96] Gian Luigi D'Alessandro, Johannes Bernhard, Stewart Boogert, Alexander Gerbershagen, Stephen Gibson, Laurence Nevay, Marcel Rosenthal, and William Shields. Implementation of CERN secondary beam lines T9 and T10 in BDSIM. *J.Phys.Conf.Ser.*, 1350 1:THPGW069, 2019.

[97] Antonio Branca. Enubet: the first monitored neutrino beam. ICHEP 2022 XLI International Conference on High Energy Physics, 2022.